



UNIVERSITÀ
DEGLI STUDI
DI PADOVA

Sede Amministrativa: Università degli Studi di Padova

Dipartimento di
INGEGNERIA DELL'INFORMAZIONE

CORSO DI DOTTORATO DI RICERCA IN: INGEGNERIA DELL'INFORMAZIONE
CURRICOLO: Scienza e Tecnologia dell'Informazione (I.C.T.)
CICLO XXX

TITOLO TESI

Heterodyne laser interferometers for the dimensional control of large ring-lasers

Coordinatore: Ch.mo Prof. Andrea Neviani

Supervisore: Dott.ssa Maria Guglielmina Pelizzo

Co-Supervisore: Prof. Giampiero Naletto

Dottorando: Alberto Donazzan

Alberto Donazzan

1107937 - IL

Heterodyne laser interferometers for the dimensional control of large ring-lasers

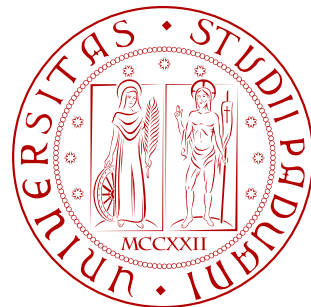
Ph.D. degree in
Information Engineering

CURRICULUM
Information Science and Technology

SUPERVISORS
Dr Maria G. Pelizzo
Prof. Giampiero Naletto

University of Padova
Department of Information Engineering

Academic year 2016/2017
Oct 2017



Alberto Donazzan: *Heterodyne laser interferometers for the dimensional control of large ring-lasers*, Ph.D. thesis in Information Engineering, © Oct 2017.

This work was realized with \LaTeX [1] on  Windows 7 using the ArsClassica package, a rework of the ClassicThesis style from André Miede, inspired to Robert Bringhurst's *The elements of typographic style*.

All trademarks, service marks and trade names belong to their respective owners.

E-MAIL

alberto.donazzan@gmail.com

CONTENTS

INTRODUCTION	xi
1 RING-LASERS IN GENERAL RELATIVITY	1
1.1 The Lense-Thirring effect	1
1.1.1 Detection of gravitomagnetism	2
1.2 The ring-laser gyroscope	3
1.2.1 Ring-laser error sources	4
1.2.2 Relativistic corrections to the Sagnac effect	6
1.3 Large ring-lasers: state of the art	8
1.3.1 G-ring	8
1.3.2 Italian ring-lasers: G-Pisa	8
1.3.3 GP2	10
1.3.4 GINGERino	11
1.4 Multi-axial ring-lasers: GINGER	13
1.4.1 Requirements	15
1.4.2 Structure	16
1.4.3 Geometrical stability	18
1.5 GINGER External Metrology	18
1.5.1 The NASA: SIM case study	18
1.5.2 Locking of GINGER	19
2 DISPLACEMENT INTERFEROMETRY	23
2.1 Basic interferometry	23
2.2 Heterodyne interferometry	24
2.2.1 The cancelable circuit	27
2.3 Phase retrieval methods	28
2.3.1 Zero-crossing detection	29
2.3.2 Lock-in detection	29
2.4 Error sources	30
2.4.1 Random	30
2.4.2 Systematic	31
2.4.3 Environmental	36
2.5 Error model	38
3 EXPERIMENTAL SETUP	39
3.1 Source unit	39
3.1.1 Laser source	44
3.1.2 Fibers	45
3.1.3 Acousto-optic modulators	45
3.2 Measurement interferometer	46
3.2.1 Holey mirror	47
3.2.2 Diffraction masks	50
3.2.3 Fiducials	53
3.2.4 Beam combiner and detection splitter	54
3.3 Detection and acquisition	55
3.3.1 Amplified photodiodes	55
3.3.2 Digital phasemeter	56

4	RESULTS AND DISCUSSION	59
4.1	Random errors estimation	59
4.2	Positioning tests	60
4.3	Performance tests	61
4.3.1	Best working conditions	61
4.3.2	Actuator noise	63
4.4	Environmental tests	64
4.4.1	Cancelable circuit operation	64
4.4.2	Vibration isolators operation	65
4.4.3	Ambient parameters changes	66
5	CONCLUSIONS AND FUTURE WORK	71
	BIBLIOGRAPHY	75

LIST OF FIGURES

Figure 1.1	Simplified representation of the LT precession.	2
Figure 1.2	Sagnac effect representation.	3
Figure 1.3	Rotational sensitivity and related applications	6
Figure 1.4	RL sensitivity compared to relativistic signals	7
Figure 1.5	Picture of the G-ring	9
Figure 1.6	G-Pisa ring-laser	10
Figure 1.7	Picture of GP2 ring-laser	11
Figure 1.8	GP2 ring-laser optical scheme	12
Figure 1.9	Picture of GINGERino	13
Figure 1.10	GP2 ring-laser optical scheme	14
Figure 1.11	Representations of the GINGER apparatus	17
Figure 1.12	External metrology truss concept	20
Figure 2.1	Homodyne and heterodyne interferometry	25
Figure 2.2	Layout of a heterodyne displacement interferometer	26
Figure 2.3	Acquisition system and lock-in detection scheme	28
Figure 2.4	Example of cyclic non-linearity	32
Figure 2.5	Simulated cyclic error over a displacement period	33
Figure 2.6	Schematic representation of the Abbe error	35
Figure 2.7	Schematic representation of the cosine error	36
Figure 3.1	Portable heterodyne source unit	40
Figure 3.2	Reference configuration for the beats simulation	40
Figure 3.3	Simulated optical beating with source phase noise	42
Figure 3.4	Simulated optical beating with source amplitude noise	43
Figure 3.5	Source light spectrum near DC	45
Figure 3.6	Interferometer alignment steps	47
Figure 3.7	Displacement gauge under test	48
Figure 3.8	Custom holey mirror	48
Figure 3.9	Illustration of the surface parallelism issue	49
Figure 3.10	Wedge interference pattern at recombination	50
Figure 3.11	Fabricated diffraction masks	51
Figure 3.12	Displacement gauge POP model	51
Figure 3.13	Simulated and acquired beam cross-sections	52
Figure 3.14	Simulated beam cross-sections (false colors)	52
Figure 3.15	Wide aperture CC retro-reflector	54
Figure 3.16	Non-beating light issue	54
Figure 3.17	Raw voltage signals spectral analysis	56
Figure 3.18	Phasemeter response to reference phase modulations	57
Figure 3.19	Simplified layout of the experimental setup	58
Figure 4.1	Random error contributions	60
Figure 4.2	Gauge response to 10nm squarewave displacement	61
Figure 4.3	Gauge response to various displacement patterns	62
Figure 4.4	Racetrack enclosure	63
Figure 4.5	Detected displacement over 3h in best conditions	64
Figure 4.6	Effects of the piezo actuator	65
Figure 4.7	Effects of the cancelable circuit	66
Figure 4.8	Effects of the pneumatic isolators	67
Figure 4.9	Monitored ambient parameters over 5h	68

Figure 4.10 Detected displacement over $5h$ 69

LIST OF TABLES

Table 2.1 Mathematical expressions for various random errors . . 31
Table 3.1 Optical power leakages from simulations 53

ABSTRACT

We present here the design, implementation and characterization of a heterodyne laser interferometer for sub-nanometer displacement metrology. The analyses and experimental activity reported in this thesis are part of a wider study, aimed to the realization of an external metrology truss for the stabilization of large opto-mechanical structures. The purpose is to monitor the 3-dimensional shape of an array of large ring-lasers, planned for future General Relativity experiments. Reaching the required $10^{-11} m$ displacement uncertainty over $7 m$ distances and several days integration periods is an challenging task. The proposed solution consists of a non-polarizing Mach-Zehnder configuration, featuring an optical cancelable circuit and a holey folding mirror, which makes possible to place the gauge in between the fiducial points which define the distance of interest. We present here the instrument working principle and the method for online phase reconstruction, as well as the complete hardware configuration used. The several sources of noise are investigated mathematically and, whenever possible, identified experimentally. The displacement gauge was tested up to $300 min$ of continuous data acquisition, showing nanometer level performances down to $100 mHz$. Air index variations and mechanical instabilities are currently the main limiting factors at lower frequencies. The present experiment has brought into light many technical issues which will constitute precious lessons learned for the future improvements of the system.

SOMMARIO

Il presente lavoro riporta il progetto, l'implementazione e la caratterizzazione di un interferometro laser a eterodina per applicazioni metrologiche sub-nanometriche. Le analisi e l'attività sperimentale legate a questa tesi fanno parte di uno studio più ampio, indirizzato alla realizzazione di un sistema di metrologia esterna per l'impiego su estese strutture opto-meccaniche. L'obiettivo è il controllo della geometria tridimensionale di un insieme di grandi giroscopi laser, destinato a futuri esperimenti nell'ambito della Relatività Generale. Il massimo livello di incertezza dimensionale tollerabile corrisponde a $10^{-11} m$, che va raggiunto su distanze operative di $7 m$ e mantenuto per periodi di diversi giorni. La soluzione proposta consiste in una configurazione Mach-Zehnder non polarizzante, che include un circuito ottico di annullamento e un peculiare specchio forato. Lo schema permette l'interrogazione della distanza di interesse tramite il posizionamento dello strumento fra i due punti fiduciali che la definiscono. Si descrivono qui il principio di funzionamento alla base del sistema, il metodo di estrapolazione della fase e tutta la strumentazione utilizzata per l'esperimento. Le diverse sorgenti di errore sono trattate analiticamente e, ove possibile, identificate sperimentalmente. Lo strumento di misura realizzato è stato testato con sessioni di acquisizione lunghe fino a $300 min$, mostrando prestazioni a livello del nanometro per frequenze decrescenti fino a $100 mHz$. Variazioni nell'indice di rifrazione dell'aria e instabilità meccaniche sono ad ora i principali fattori che limitano le prestazioni del sistema

alle basse frequenze. L'esperimento ha messo in luce diverse problematiche tecniche, che costituiranno un prezioso bagaglio di esperienze, utile per il futuro avanzamento dell'attività di ricerca.

C'est que, malheureusement, on ne se doute pas que le livre le plus précieux du plus savant serait celui où il dirait tout ce qu'il ne sait pas, c'est qu'on ne se doute pas qu'un auteur ne nuit jamais tant à ses lecteurs que quand il dissimule une difficulté.

Unfortunately what is little recognized is that the most worthwhile scientific books are those in which the author clearly indicates what he does not know; there is no doubt that an author most hurts his readers by concealing difficulties.

— Évariste Galois

ACKNOWLEDGMENTS

First, I would like to thank my supervisors, Dr Maria Pelizzo and Prof. Giampiero Naletto, together with the entire GINGER collaboration, for supporting this work and giving me the precious opportunity of pursuing my doctorate. Particularly, I wish to thank Davide Cuccato, Jacopo Belfi and Antonello Ortolan for the many valuable conversations, for their willingness, smart thinking and wise advice. A special thank goes to Alain Corso, for his never-ending support and for helping me not to forget Electronics engineering.

Thanks to the MePA for making myself understand that handling paperwork is not my way. A warm thank you to all the patient administration people who managed it for me. Thanks also to “The President” and all the LUXOR guys, for the technical support and the precious business ideas, as well as for entrusting me with the food court management.

I am also grateful to my family, who have always been there and who taught me to never forget to smile. Finally, I would like to dedicate this work to Noemi, who sincerely cares for me since the day we met (again).

Padova, oct 2017

A. D.

INTRODUCTION

A ring-laser gyroscope (RL) employs laser light, circulating inside a closed optical cavity, for measuring rotation rates with high accuracy. When the instrument is rotated, two beams counter-propagating inside the cavity gather a frequency offset that can be exploited, thanks to their mutual interference, to output an optical beating. The physical mechanism that translates rotations into fringe shifts is named after the physicist Georges Sagnac, who conceived and implemented the first passive ring interferometer in 1913 [2]. Although Sagnac had the purpose to detect the effect of the relative motion of the Earth and the ether, successive works explained the Sagnac effect in the framework of the Special and General Relativity [3]. Following this interpretation, in the past few years ring-lasers have become an instrument of interest for the verification of General Relativity (GR) with ground-based experiments. Indeed, large size ring-laser gyroscopes are reaching increasingly higher sensitivities, already allowing for outstanding geodetic measurements [4, 5].

GINGER (Gyroscopes IN GEneral Relativity) is an experiment proposal for the measurement, by means of an array of large ring-lasers, of a very weak relativistic effect produced by the Earth's rotating mass [6, 7]. This effect, known as inertial frame dragging, or *Lense-Thirring effect* (LT), is predicted by General Relativity and was studied by Lense and Thirring in 1918 for the case of the weak gravitational field of a slowly rotating body [8]. The Earth induced LT, although very weak, can in principle be measured by monitoring slight alterations of the Earth's rotation vector. To this end, many possible configurations of ring-lasers array have been conceived and analyzed. In Italy, since 2008 the landscape of public scientific research has seen the birth and growth of some notable experimental activities, which have started to deal with the many challenges offered by the future realization of GINGER.

One of the main issues in the feasibility of GINGER is its dimensional stability. In fact, the good combined operation of many large ring-lasers will be possible, within the required specifications, only with the aid of advanced metrological techniques, able to provide accurate dimensional knowledge of the instrument geometry. The present work constitute the first major achievement towards the construction of a complex external metrology truss, called GEMS. The truss is intended to the monitoring and control of the relative positions of the many mirrors constituting the GINGER array.

We report here on the implementation of a heterodyne Mach-Zehnder interferometer devoted to the measurement of displacements between couples of corner-cube retro-reflectors. The optical design takes advantage of a cancelable circuit for optimal noise rejection, which is implemented by wavefront splitting of the second arm with the insertion of a holey mirror and blocking masks. With respect to other non-polarizing solutions [9, 10] and similarly to [11], the developed layout is suitable for insertion along measurement axes which can extend up to many meters. In addition, the whole instrument can run unattended for many days and is designed to implement a closed control loop for the stabilization of the monitored distance. Currently, the apparatus is able to measure in real-time the relative displacement between two fiducial points placed 1 m apart with an uncertainty lower than $3\text{ nm}/\sqrt{\text{Hz}}$ down to 100 mHz.

Thesis outline

CHAPTER ONE gives an introduction to the Lense-Thirring effect, as well as on the ring-laser gyroscope technology. The effects of systematic and random errors on RLs are addressed and their response to the relativistic precessions is described. Finally, the experimental activities related to the GINGER project are presented.

CHAPTER TWO introduces to the basic principles of homodyne and heterodyne interferometry. It focuses on the analytic description of suitable optical schemes for high resolution displacement metrology and presents the many possible sources of errors that can affect this type of measurements. A comprehensive error model is also provided and later used for the interpretation of the collected data.

CHAPTER THREE describes in detail the experimental setup which has been implemented for the feasibility study of GEMS. All the hardware used is presented, with focus on the optical layout and on the associated design and alignment issues. The detection and acquisition units are illustrated as well.

CHAPTER FOUR presents some notable experimental results obtained with the developed gauge. The interferometer performances are determined together with its limiting error sources and interactions with the surrounding environment.

CHAPTER FIVE states the conclusions regarding the work conducted up to now and suggests future perspectives for the GEMS experiment.

Worth mentioning is that the work here presented was carried out within the facilities offered by the Institute for Photonics and Nanotechnology (CNR-IFN), located in Padova. Currently, the developed experiment is housed in a dedicated optical laboratory, which was fully equipped to the purpose. A brief description of the Institute follows below.

Information about CNR-IFN

The *Istituto di Fotonica e Nanotecnologie* (CNR-IFN), Italian for “Institute for Photonics and Nanotechnology”, carries out innovative research in the fields of photonics and of nanotechnologies considering both the fundamental aspects and their applications, involving the development of novel photonic devices and systems, optoelectronic equipment, and electronics devices. CNR-IFN is tightly integrated with the national scientific community and collaborates with the major international Universities and research centres through targeted projects funded by main national and international agencies and foundations.



The main research topics of the IFN operative unit in Padova are:

- Optical instrumentation for space
- Photon instrumentation for the extreme ultraviolet
- Coatings and optical materials
- Adaptive optics
- Quantum communications
- Applied optics for industrial applications

CNR-IFN belongs to the National Research Council (CNR), a public organization who is in charge to carry out, promote, spread, transfer and improve research activities in the main sectors of knowledge growth and of its applications for the scientific, technological, economic and social development of the Country. The IFN consists of a headquarter in Milan, and four branch sections (operative units) in Bari, Padova, Roma, and Trento. The personnel is composed by 45 staff researchers, 18 employees in administration and technical services, 95 associated researchers, and a variable number of undergraduate, PhD students and post-doctoral fellows.

CNR-IFN laboratories located in Padova.



PUBLICATIONS

Journal papers

Alberto Donazzan et al. “Characterization of nanometer displacement gauge for dimensional control of large opto-mechanical structures”. In: *Opt. Express* (2017, submitted)

Conference papers

Alberto Donazzan, Giampiero Naletto, and Maria G. Pelizzo. “Study of the optical crosstalk in a heterodyne displacement gauge with cancelable circuit”. In: *Modeling Aspects in Optical Metrology VI*. vol. 10330. International Society for Optics and Photonics. 2017, 103300F. DOI: [10.1117/12.2270193](https://doi.org/10.1117/12.2270193)

Antonello Ortolan et al. “GINGER: an array of ring lasers for testing fundamental physics”. In: *Proceedings of the MG14 Meeting on General Relativity*. Ed. by Massimo Bianchi, Robert T. Jantzen, and Ruffini Remo. 2017

Alberto Donazzan et al. “A network of heterodyne laser interferometers for monitoring and control of large ring-lasers”. In: *SPIE Optical Engineering + Applications*. 2016, pp. 1–8. DOI: [10.1117/12.2237638](https://doi.org/10.1117/12.2237638)

Alberto Donazzan et al. “External metrology system for the stabilization of large ring-lasers”. In: *Metrology for Aerospace (MetroAeroSpace), 2016 IEEE*. IEEE. 2016, pp. 266–270

J. Belfi et al. “Very high sensitivity laser gyroscopes for general relativity tests in a ground laboratory”. In: *2016 European Frequency and Time Forum (EFTF)*. Apr. 2016, pp. 1–4. DOI: [10.1109/EFTF.2016.7477839](https://doi.org/10.1109/EFTF.2016.7477839)

A. Ortolan et al. “The GINGER project and status of the GINGERino prototype at LNGS”. in: *Proceedings, 14th International Conference on Topics in Astroparticle and Underground Physics (TAUP 2015)*. Vol. 718. 7. 2016, p. 072003. DOI: [10.1088/1742-6596/718/7/072003](https://doi.org/10.1088/1742-6596/718/7/072003)

A. Di Virgilio et al. “The GINGER Project”. In: *Nuclear Physics B-Proceedings Supplements* (2016), pp. 1–8

A. Di Virgilio et al. “The GINGER Project and status of the ring-laser of LNGS”. in: *Proceedings of the XVI International Workshop on Neutrino Telescopes (NEUTEL2015)*. Palazzo Franchetti, Venice, Italy, Mar. 2015, pp. 2–6

1

RING-LASERS IN GENERAL RELATIVITY

This chapter introduces to the Lense-Thirring relativistic precession and presents the various techniques for measuring it with increasing levels of accuracy. Among them, the optical gyroscope technology is described, with particular focus on ring-lasers. The Sagnac effect is presented analytically, as well as the systematic and random errors which limit the sensitivity of a ring-laser for rotation measurements. The state of the art of large frame RLs is presented, together with the many past and present experiments developed within the Italian scene, namely G-Pisa, GP2 and GINGERino. The design of the multi-axial sensor GINGER is then described, pointing out its binding requirements in terms of structural stability. GEMS, the external metrology truss conceived to solve the issue, is finally introduced.

1.1 THE LENSE-THIRRING EFFECT

The term gravitomagnetism designates the effects and phenomena predicted by GR which occur when the source of a gravitational field is rotating. Actually, rotational effects are due also to rotating reference frames (i.e. non inertial observers), as we will see in [subsection 1.2.2](#).

In the case of celestial bodies, including the planet Earth, gravito-magnetic effects are due to the absolute rotation of the massive source with respect to distant stars. In the case of weak field approximation, gravitomagnetism can be described as the analogue of a magnetic field of a rotating spherical charge. In practice at the lowest approximation level, a dipolar gravitomagnetic field is obtained, with the dimensions of an angular velocity. The explicit form in a non-rotating reference frame centered on the source (that is the Earth center) is (see e.g. [21])

$$\mathbf{B} = \frac{2G}{c^2 R^3} [\mathbf{J}_\oplus - 3(\mathbf{J}_\oplus \cdot \mathbf{u}_r)\mathbf{u}_r] , \quad (1.1)$$

where $\mathbf{R} \equiv R\mathbf{u}_r$ is the position of the laboratory with respect to the Earth center, c is the speed of light, $\mathbf{J}_\oplus \simeq I_\oplus \boldsymbol{\Omega}_\oplus$ is the angular momentum of the Earth approximated as a rotating rigid sphere of radius R , mass M , moment of inertia $I_\oplus = (2/5)MR^2$ and rotation rate $\boldsymbol{\Omega}_\oplus$; the unit vector \mathbf{u}_r is along the radial direction.

The effect produced by a field like \mathbf{B} on a massive test body moving with velocity \mathbf{v} looks like the one produced by a magnetic field on a moving charge:

$$\frac{d\mathbf{v}}{dt} = \mathbf{G} + \mathbf{v} \wedge \mathbf{B} , \quad (1.2)$$

where

$$\mathbf{G} = -\frac{GM}{R^2} \mathbf{u}_r \quad (1.3)$$

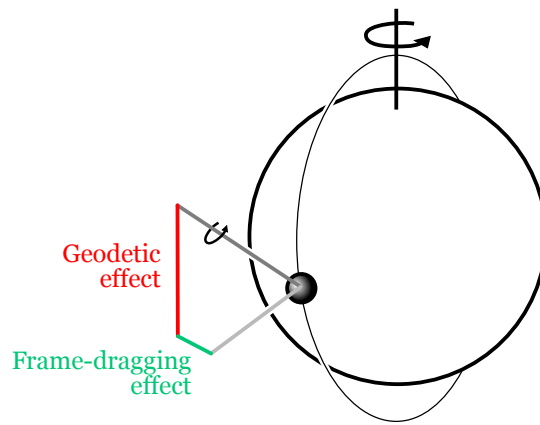


Figure 1.1: Simplified representation of a gyroscope orbiting around the planet Earth. General relativistic effects on the gyroscope are showed in color: the precessions make its spinning axis change orientation.

is the newtonian gravitational field, so that the effect can be described in terms of a gravito-electromagnetic Lorentz force, where the newtonian gravitational field plays the role of the gravito-electric field.

Therefore, the rotation of the massive Earth affects a gyroscope orbiting around it, in such a way that it undergoes a precession called *Lense-Thirring effect*, also known as *frame-dragging*. Even a freely falling body with null local angular momentum is subject to this phenomenon, because it will be seen as rotating by a distant observer at rest with the fixed stars.

1.1.1 Detection of gravitomagnetism

Gravitomagnetic effects can in principle be measured with different methods. The one that has most often been considered is based on the behavior of a gyroscope, that can be either in free fall (on board an orbiting satellite) or attached to the rotating Earth. The axis of the gyroscope is affected in various ways by the presence of the Earth's gravitational field, as showed in Figure 1.1. As previously stated, for gravitomagnetism, a little mechanical gyroscope is the analogous of a small dipolar magnet (a current loop), so that it behaves as magnetic dipoles do when immersed in an external magnetic field.

Direct experimental evidence of the Earth induced frame dragging relies for the moment on three only experiments in space: Gravity Probe B (GP-B) that took data from 2004 to 2005 and was concluded and the results published in 2011 [22]; the two LAGEOS (LAsER GEODynamics Satellite) orbital nodes analysis, published in 2004 [23] and, with an improved modeling of the gravitational field of the Earth, in 2011 [24]; the LARES (Laser Relativity Satellite) mission, launched in February 2012 and ended in 2016. The dedicated mission GP-B was launched by NASA in 2004 after more than 30 years of research and development. It took data for a year and required five years of data analysis to measure the LT effect with an uncertainty of 19%. With precise satellite laser ranging the same value was confirmed with approximately 10% uncertainty, using LAGEOS and LAGEOS 2. The Earth's gravity field mapping, provided by the space geodesy mission GRACE was essential for this kind of measurement. A later publication reports an improved accuracy of 5%, based on LAGEOS, LAGEOS2 and LARES orbit data over a 3.5 years period [25]. Recently a new LARES2 mission has been approved by the Italian Space Agency [26], which aims to a reduction of the LT uncertainty down to 0.2%. The measurement will also be possible thanks to the new GRACE Follow-On space mission, scheduled for launch at the end of 2017[27], which will continue to improve the accuracy

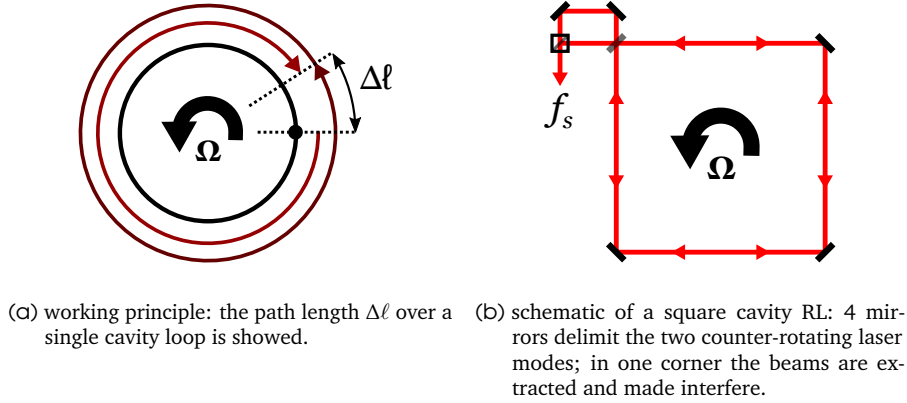


Figure 1.2: Sagnac effect representation for two laser beams counter-propagating in a rotating cavity.

of measurement of the Earth gravity field and its variations. Other evidence of gravito-magnetic effects may be found in the laser ranging of the orbit of the moon and in the study of the dynamics of binary systems composed of at least one compact massive object (neutron star). We point out that all the already available results required years of data analysis, thus orbits averaging, in order to extract a reliable value from all the systematics and random errors.

A different experimental approach consists in using light as a probe. In this case the main remark is that the propagation of light in the gravitational field of a rotating body is not symmetric. Therefore, the coordinated time duration for a given space trajectory in the same sense as the rotation of the gravitational source is different from the one obtained when moving in the opposite direction. This property of the propagation of light is the one exploited by ring-laser gyroscopes.

1.2 THE RING-LASER GYROSCOPE

Ring-laser gyroscopes are inertial sensors based on the *Sagnac effect* [28] which are able to detect their rotation rate with respect to a non-accelerated reference frame. Laser light circulates inside a polygonal cavity in opposite directions and is forced, using mirrors, to move along a closed path in space. In an inertial frame the two counter-propagating beams follow a path of the same length, but, if the system is rotated, a round-trip time difference occurs between the clockwise rotating beam and the counter-clockwise rotating one, as they experience a longer and a shorter path respectively. This difference translates directly into an optical frequency shift f_s between the two beams, which is proportional to the rotation rate accordingly to

$$f_s = \frac{4\mathbf{A} \cdot \boldsymbol{\Omega}}{\lambda p} = \underbrace{\frac{4A}{\lambda p}}_{k_{\text{SF}}} \mathbf{u}_A \cdot \boldsymbol{\Omega}, \quad (1.4)$$

where $\boldsymbol{\Omega}$ is the angular velocity vector, p is the optical path length of a single cavity loop (also known as the *cavity perimeter*), $\mathbf{A} = A\mathbf{u}_A$ is the area vector, normal to the instrument enclosed area A , and λ is the wavelength of the

laser radiation in steady conditions. Thus Ω and f_s are linearly dependent through the parameter $k_{SF} = 4A/(\lambda p)$, which is known as “scale factor”. As showed in [Figure 1.2b](#), the Sagnac frequency can be easily extracted from the instrument by properly recombining the two counter-propagating beams, which will beat at f_s [29]. For a thorough analytical treatment of the optical beating phenomenon we refer to [section 2.2](#).

The non-reciprocal nature of the Sagnac effect can be exploited to measure several effects which break time-reversal symmetry, such as magneto-optical and nonlinear effects. On the other side, any source of noise acting in a non-reciprocal way, such as mechanical and thermal fluctuations, is parasitic and needs to be removed or minimized to guarantee optimal measurements. Moreover, the Sagnac effect is independent of specific material properties and it has been observed with photons as well as coherent massive particle beam [30].

Compared to conventional spinning gyroscopes, optical gyroscopes shows several advantages: they have large dynamic range, small size, high precision, they do not have any moving mechanical part and they are insensitive to translational accelerations. Thanks to these features laser gyros acquired a prominent role in many applications, ranging from inertial navigation system on commercial airliners, ships and spacecraft to geodesy and geophysics [31], to test of fundamental physics [32, 33].

Optical gyroscopes are traditionally divided in two main classes. Passive devices take advantage of an external light source, which must be injected into the optical system to make it work. An example are fiber optic gyroscopes (FOG), where the closed optical path is defined by a long fiber [34]. These sensors are mostly used in applications requiring low performance such as robotics, space applications, inertial navigation of submarines and spacecrafts. Differently, in active devices, namely ring-lasers, the light source does not come from outside the instrument. The two counter-propagating beams are emitted by an active medium that fills the closed cavity. The presence of the medium adds gain dispersion, dissipative losses and non-reciprocal phenomena, which can limit the overall instrument performances. On the other hand, the intracavity generation of the beams assures better reciprocity and equal optical paths. Up to now, all cutting edge sensibility optical gyroscopes are or large RL type. The most commonly used active medium in RL is a helium-neon gas mixture, because it represents a well established laser technology and offers good emission efficiency and beam quality. The first He-Ne ring-laser operated at a wavelength of $1.153 \mu m$ [35]. Today the $632.8 nm$ transition is mostly used, since the optical components at this wavelength are largely available.

1.2.1 Ring-laser error sources

Several error sources which can corrupt the linear relation between f_s and Ω have been analyzed in detail in previous works [36, 37]. These perturbations can be treated as corrective terms which alter the beat frequency of a RL. [Equation 1.4](#) can be rewritten as

$$f_s = (k_{SF} + k_n) \mathbf{u}_A \cdot \Omega + f_0 + f_{BS} + f_{shot} , \quad (1.5)$$

where the deviations from the ideal behavior expressed by [Equation 1.4](#) are:

- corrections to the scale factor k_n , which are due to fluctuations of the cavity geometry, cavity losses or variations of the laser active medium

- parameters (laser gain, plasma temperature and pressure, frequency detuning);
- null-shift errors f_0 , due to any cavity non-reciprocity, e.g. cavity non planarity or asymmetries in the cavity geometry, gas flows inside the tubes, parasite magnetic fields and mirror birefringence;
 - non-linear coupling of the counter-propagating laser beams f_{BS} , due to light retro-reflections, also known as *backscattering*;
 - photon shot-noise, represented by the random variable f_{shot} , which is due to light incoherence.

Regarding the error related to the scale factor, the fluctuations of k_{SF} are caused by both reciprocal and non-reciprocal effects affecting the stability of the A/p ratio. Slow deformations of the optical cavity can be driven by temperature, pressure and ageing of materials. These effects are the present limit to the performance of large devices. The term k_n accounts as well for changes in the optical cavity length due to the dispersion properties of the plasma discharge. These are mainly induced by fluctuation of active medium parameters, such as gain, temperature, pressure and detuning between the gain center frequency and the beams optical frequencies. Spectroscopic diagnostics can be implemented to monitor this type of variations and the resulting systematic effects can be subtracted from the measurement data using online and offline methods [38].

Null-shift, also known as *bias error*, is a non-zero beat frequency f_0 which can be detected in the case of a null rotation. It usually exhibits as a difference between the intensities of the circulating beams. The null shift is mainly caused by lack of surface planarity in the cavity mirrors, causing that the counter propagating beams to experience two different quality factors. Other sources of bias are the Faraday effect and the Langmuir effect. The Faraday effect occurs in of external magnetic field are present in the plasma, due to the elliptical polarizations of the two beams. The Langmuir effect is a flow of the laser active medium which is seen as moving on opposite directions by the counter-propagating modes. A significant reduction of this latter effect can be obtained with RF laser pumping, instead of DC excitation.

Mode coupling, is the tendency, typical of coupled oscillators with similar frequency, of the counter-propagating laser beams to lock to the same frequency, practically blinding the ring-laser as rotation sensor. Unlike the small ring-lasers used for navigation systems, large RL easily detect Earth's rotation Ω_{\oplus} , which provides a nearly constant background rotation rate and avoids lock-in. Even without actual locking, mode coupling is associated to pulling (f_{BS}) of the Sagnac frequency and can cause serious systematic errors. As already mentioned, mode coupling is induced by backscatter processes, which arise from mirror imperfections that cause a fraction of one laser beam to propagate in the wrong direction. The problem of backscatter has been already treated extensively [39] and many approaches are used in order to minimize it [40–42].

Finally, shot-noise is the irreducible accounting for quantum fluctuations of photon number in the interferogram. This noise source imposes a fundamental limit to the angular velocity resolution of a RL. For a given integration time T , the equivalent rotational noise $\epsilon_{\Omega, shot}$, expressed in units of *rad/s*, reads

$$\epsilon_{\Omega, shot} = \frac{cp}{4AQ} \sqrt{\frac{h\nu}{P_{out}T}}, \quad (1.6)$$

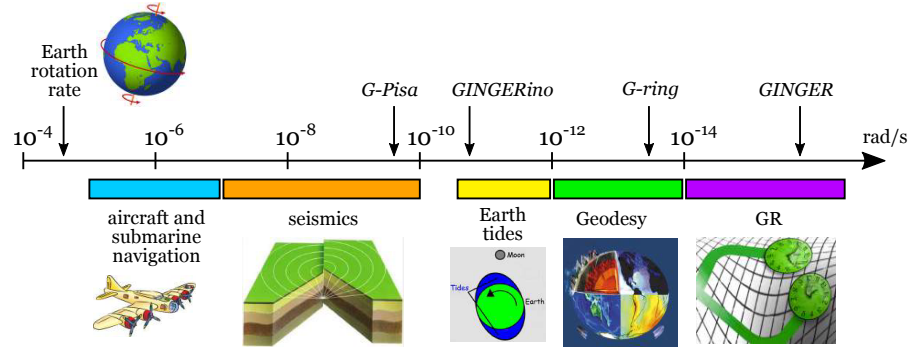


Figure 1.3: Orders of magnitude of rotations and ring laser gyroscopes. The sensitivities in measuring rotations achieved by the G-Pisa and the G-ring experiments are indicated, as well as the target sensitivity needed to measure the Lense-Thirring effect.

where Q is the quality factor of the optical cavity, h is the Planck constant, $\nu = c/\lambda$ is the light frequency in the ring medium and P_{out} is the optical power of the beating light extracted from the ring. Hence, for a given sampling time, the minimum uncertainty in the rotation rate depends upon the size of the cavity, the losses of the mirrors and the optical power level.

Therefore, as suggested by the Equation 1.4 and Equation 1.6, the larger the ring, the easier the detection of the Sagnac frequency. However, it is clear that increasing the dimension of a RL eventually results in more demanding requirements on the mirrors alignment and on the mechanical stability of the device. Variations of the environmental conditions during measurement processes on long timescales (hours) induce larger deformations on larger optical cavities, enhancing the fluctuations of the correction terms in Equation 1.5. Indeed, the magnitude of those effects, which are mainly driven by temperature and pressure drifts, has been reported to be proportional to p . A trade off must then be made between the minimization of intrinsic and systematic noise sources.

Figure 1.3 shows the many RLs application, depending on their sensitivity level. The sensitivities achieved by the GINGERino experiment (L'Aquila, Italy) and the G-ring (Wetzell, Germany) are indicated, as well as the sensitivity required to detect relativistic effects on rotation (see following section).

1.2.2 Relativistic corrections to the Sagnac effect

More specifically on the detection of Lense-Thirring effect, we must note that a ring-laser, which is closed from the view point of the host laboratory, is not so for an observer bound to the fixed stars frame. Essentially, as already mentioned, the opposite directions of propagation are not equivalent and the two times required for light to come back to the starting point are (slightly) different. The difference in the two times of flight is made up of various contributions, depending on the rotation of the axes of the local reference frame with respect to distant stars, on the fact that the local gravitational (newtonian) potential is not null, and of course on the gravito-magnetic drag, which is our main interest. What matters, however, is that the final proper time difference is an *invariant*: it does not depend on the choice of the reference frame or of the coordinates.

The relativistic response of an Earth-bound RL has been calculated many times in the literature, usually starting from the metric near the Earth surface,

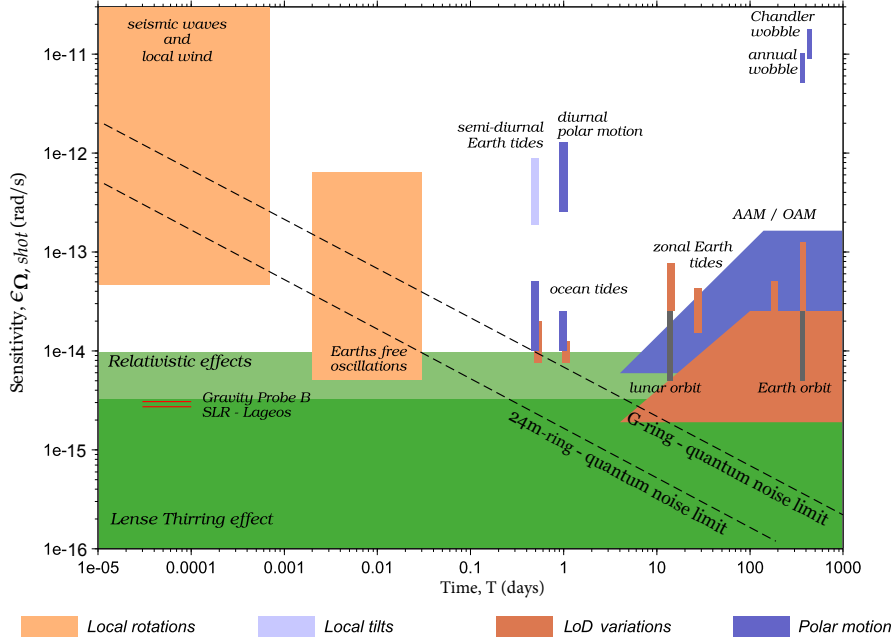


Figure 1.4: Geodetic and relativistic signals accessible to an Earth bound RL with given sensitivity $\epsilon_{\Omega, shot}$ [7]. The horizontal axis accounts for the typical time duration of the showed events. The green parts show the region of interest for the geodetic precession and the Lense–Thirring precession; on the left the present level of test obtained by GP-B and Lageos is showed. The two dotted lines show the shot noise level of the G-ring (16 m perimeter), and of a ring with perimeter 24 m.

which is the solution of the linearized Einstein equations in vacuum for a rotating body (see e.g. [6]). The Sagnac frequency of Equation 1.4 can be rewritten as

$$f_s = k_{SF} \mathbf{n}_A \cdot \left(\underbrace{\Omega_{\oplus}}_{\substack{\text{Sagnac term} \\ \sim 10^{-5} \text{ rad/s}}} + \underbrace{\Omega_G + \Omega_B}_{\substack{\text{Geodetic and} \\ \text{LT terms} \\ \sim 10^{-14} \text{ rad/s}}} + \underbrace{\Omega_W + \Omega_T}_{\substack{\text{minor terms} \\ \sim 10^{-17} \text{ rad/s}}} \right). \quad (1.7)$$

Thus the effective angular velocity vector $\mathbf{\Omega}$ is the sum of 3 major contributions:

1. the kinematic Earth rotation vector, or Sagnac term, $\mathbf{\Omega}_{\oplus} = \Omega_{\oplus} \mathbf{u}_{\oplus}$ as measured from an inertial reference frame, where

$$\Omega_{\oplus} = \frac{2\pi}{LoD} \simeq 7.2921 \cdot 10^{-5} \text{ rad/s} \quad (1.8)$$

and $LoD \simeq 86164.09053 \text{ s}$ is the length of the day;

2. the pure mass contribution, or Geodetic term

$$\mathbf{\Omega}_G = -\frac{2GM}{c^2 R} \Omega_{\oplus} \sin \theta \mathbf{u}_{\theta}, \quad (1.9)$$

where \mathbf{u}_{θ} is along the local meridian in the sense of increasing colatitudes;

3. the Earth angular momentum contribution or Lense-Thirring term, which derives from Equation 1.1:

$$\boldsymbol{\Omega}_B = -\frac{1}{2}\mathbf{B} = -\frac{G}{c^2 R^3} [\mathbf{J}_\oplus - 3(\mathbf{J}_\oplus \cdot \mathbf{u}_r)\mathbf{u}_r] . \quad (1.10)$$

All terms in $\boldsymbol{\Omega}$, except for $\boldsymbol{\Omega}_\oplus$, are called *relativistic precessions*, but properly speaking only the third, $\boldsymbol{\Omega}_B$, is due to the intrinsic gravito-magnetic field of the Earth, as defined by Equation 1.1. Using Earth mass, rotation rate and radius, we have that Geodetic and Lense-Thirring terms are both of order $\sim 10^{-9}$ with respect to the Sagnac term, while the other terms are two or three orders of magnitude smaller. Consequently, to leading order, the relativistic contribution to the rotation measured by the ring-laser can be approximated to $\boldsymbol{\Omega} \simeq \boldsymbol{\Omega}_\oplus + \boldsymbol{\Omega}_G + \boldsymbol{\Omega}_B$. Figure 1.4 plots the required sensitivity for a ring-laser devoted to the detection of the relativistic precessions and of many other signals of interest for Geodesy and Geophysics.

1.3 LARGE RING-LASERS: STATE OF THE ART

Several large frame RLs have been developed around the world over the last two decades with the aim of reaching ever higher sensitivities. In particular, we mention the international collaboration among Germany (U. K. Schreiber and collaborators, Technische Universität München and Fundamentalstation Wettzell), Italy (A. Di Virgilio and collaborators, INFN Pisa) and New Zealand (G. E. Stedman and collaborators, University of Christchurch). We refer to [31, 43] for a comprehensive review of the current state of the art in large frame RLs technology.

1.3.1 G-ring

To this day, the best RL is the Grossring “G”, located at the Geodätisches Observatorium in Wettzell, Bavaria (GER). The *G-ring* has an optical cavity length $p = 16\text{ m}$ and routinely achieves a sensitivity of few *prad/s* at the frequency of 1 Hz [31, 44]. The optical cavity of the G-ring has a semi-monolithic design to minimize the effects of environmental drifts: it exploits an ultra-low expansion coefficient glass ($\approx 5 \cdot 10^{-8} / K$), named *Zerodur*, and its high mechanical stability is guaranteed by four bars rigidly connected to a large monolithic base plate. Spherical supermirrors are attached to the bar side faces by molecular adhesion, ensuring stable vacuum sealing. Active control of the cavity perimeter stabilizes the circulating laser beams frequency against an optical frequency reference. The remarkable results obtained by the G-ring have been possible thanks to continuous improvements of the experiment over the years. Worth mentioning are a pressure stabilizing vessel that encloses the entire ring laser structure [45] and, more recently, the frequency locking of the ring-laser to a single tooth of an optical frequency comb, referenced to a hydrogen maser [46].

1.3.2 Italian ring-lasers: G-Pisa

Since 2008, Italy has seen the start and growth of research activities in the field of large RLs. The leading challenge was to demonstrate the effectiveness of

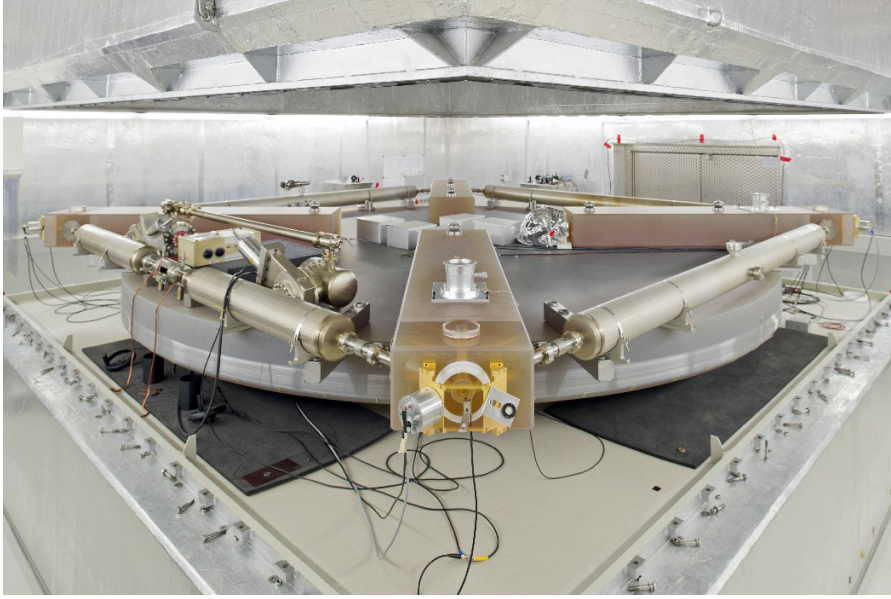


Figure 1.5: Picture of the G-ring, showing its semi-monolithic Zerodur structure. The pressure stabilizing vessel can be seen lifted up in the upper part of the picture. Courtesy of U. K. Schreiber.

heterolithic designs can for high-sensitivity applications. In this effort, several tools and working devices have been developed, namely the *G-Pisa*, *GP2* and *GINGERino* experiments. All the present italian RLs feature a square optical cavity and, except for *GP2*, are based on a design, called *GEOsensor*, conceived after the G-ring experience [47]. Actually, the good performance achieved by the G-ring after few years of operation showed both the potentialities and the limit of its design. A notable sensitivity improvement would be possible by a size upscale, as predicted by Equation 1.4 and Equation 1.6, but larger monolithic Zerodur slabs become too expensive and bulky, moreover are not suitable for multi-axial designs.

The experimental activities started with the middle-size RL “G-Pisa” [48], showed in Figure 1.6. It had an heterolithic and flexible design: it was able to work in the horizontal as well as in the vertical orientation and its sides could be adjusted in length from 1.40m to 0.90m. A rotational sensitivity of $10^8 \text{ rad}/\sqrt{\text{Hz}}$ below 1 Hz was demonstrated for the horizontal configuration [49]. After successful operation as a rotational sensor for the Virgo gravitational wave interferometer [50, 51], the upgraded version of the G-Pisa setup was installed on a granite slab oriented with the normal to the ring plane almost parallel to the Earth rotation axis, to maximize the Sagnac effect and minimize the contribution of the orientation error. The stabilization of the cavity perimeter against a primary frequency standard was then optimized [49]. A set of spectroscopic diagnostic of the active medium parameters was developed as well, together with an online denoising method based on the Kalman filter approach [38, 52].

The results from G-Pisa paved the way to the use of heterolithic designs, equipped with proper precise diagnostics, for the high accuracy measurement of the Earth rotation rate. This motivated the design of the large frame multi-axial ring-laser “GINGER” [6], which is described in more detail in section 1.4. The GINGER project specifications require a strict control of the systematic errors related to the fluctuation of the cavity geometry and the laser active

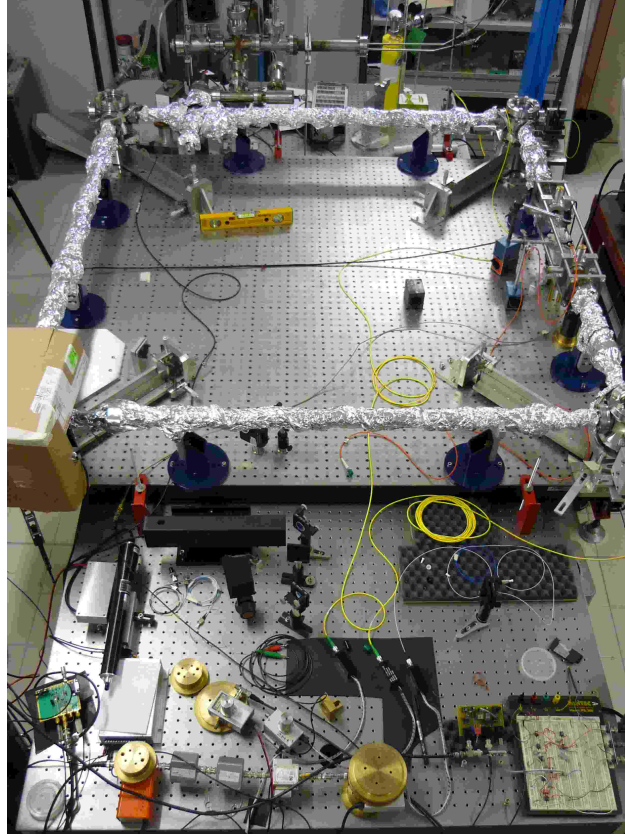


Figure 1.6: G-Pisa ring-laser in the horizontal configuration.

medium parameters, as well as very low environmental noise. The two RLs presently operating in Italy, GINGERino and GP2, have both been developed as intermediate prototypes of GINGER, in order to tackle its most critical issues. Pictures of the two experiments are showed in [Figure 1.7](#) and [Figure 1.9](#).

1.3.3 GP2

GP2 is devoted to test active control strategies for the monitoring and control of the ring-laser geometry, going beyond the level attainable by means of passive methods. It exhibits an innovative design, in which the mirrors that constitute the square optical cavity are equipped with a piezo nano-positioning system, in order to actively control their relative positions. The relevant observables to constraint the geometry are the perimeter of the ring cavity and the lengths of the two diagonal cavities, defined by the mirrors on opposite corners. The use of the diagonal lengths is pioneering in the RL technology. It has been demonstrated that, when the lengths of the two diagonals are locked to the same value, the perturbations to the mirror positions affect only quadratically the ring-laser perimeter and scale factor [53]. In this case, the regular square geometry corresponds to a saddle-point of the perimeter, and so the scale factor fluctuations k_n are minimized. To allow the implementation of this new control strategy, the vacuum chamber of GP2 features the possibility of injecting an external laser beam in the linear cavities formed by each pair of opposite mirrors.

To stabilize the absolute lengths of the two diagonal cavities with respect to a reference laser, an original interferometric technique has been conceived. It consists of locking the resonance frequencies (f_{diag}) of the two cavities to the

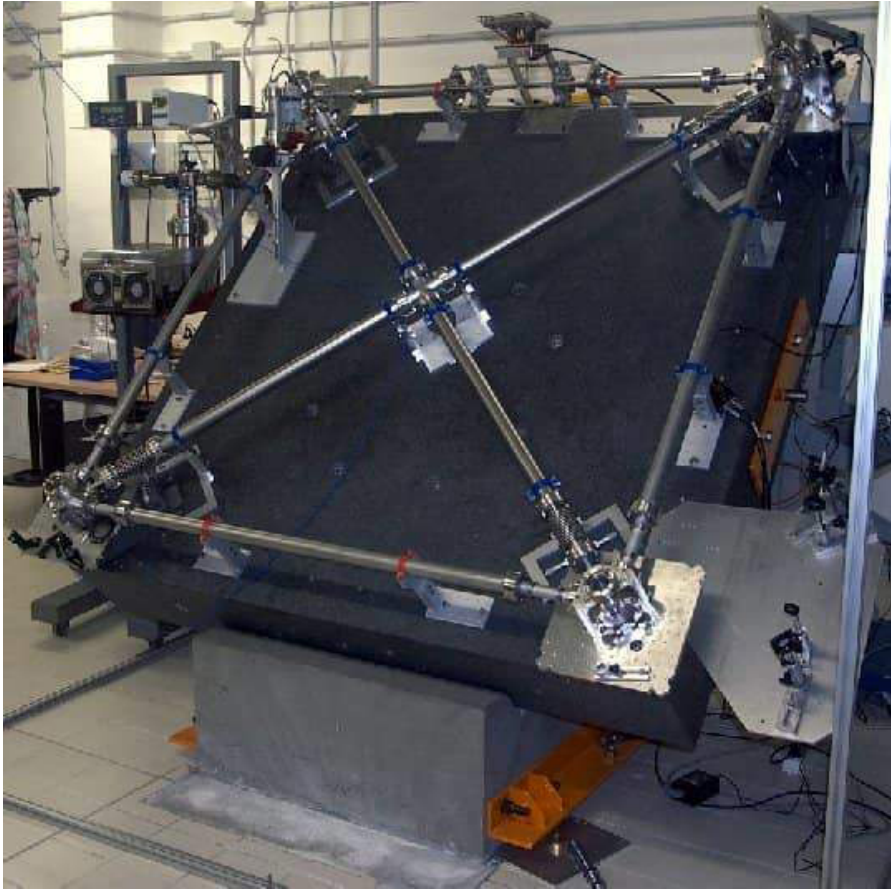


Figure 1.7: GP2 ring-laser installed at INFN-Pisa laboratory.

same laser carrier frequency and, at the same time, in determining an integer multiple of the two free spectral ranges (FSR). The error signals needed to implement, for each diagonal, a two frequency measurement (f_{diag} and FSR) in closed loop, are recovered by phase-modulating the interrogating laser source with a combination of three independent frequencies, through a single electro-optic modulator (see Figure 1.8). The stabilization scheme has been tested in a table top experiment on two Fabry-Perot resonators composed by two couples of spherical mirrors. These resonators were mounted on an optical bench to simulate the cavities along the diagonals of a RL gyroscope. With this setup, the capability of stabilizing the two lengths at the level of 1 part in 10^{11} was demonstrated [54, 55], and setting their difference equal to zero within the precision of 500 nm , with residual fluctuations only limited by the laser frequency noise.

The above described metrology technique has also been partially implemented in GP2. Preliminary results demonstrate the compatibility of the scheme with the RL operation, resulting in a sub-nanometer diagonal lengths stabilization with a signal integration time of few hundred seconds [56].

1.3.4 GINGERino

The second ongoing experiment within the GINGER framework is located in the LNGS underground laboratory at L'Aquila [17, 57]. GINGERino is a test

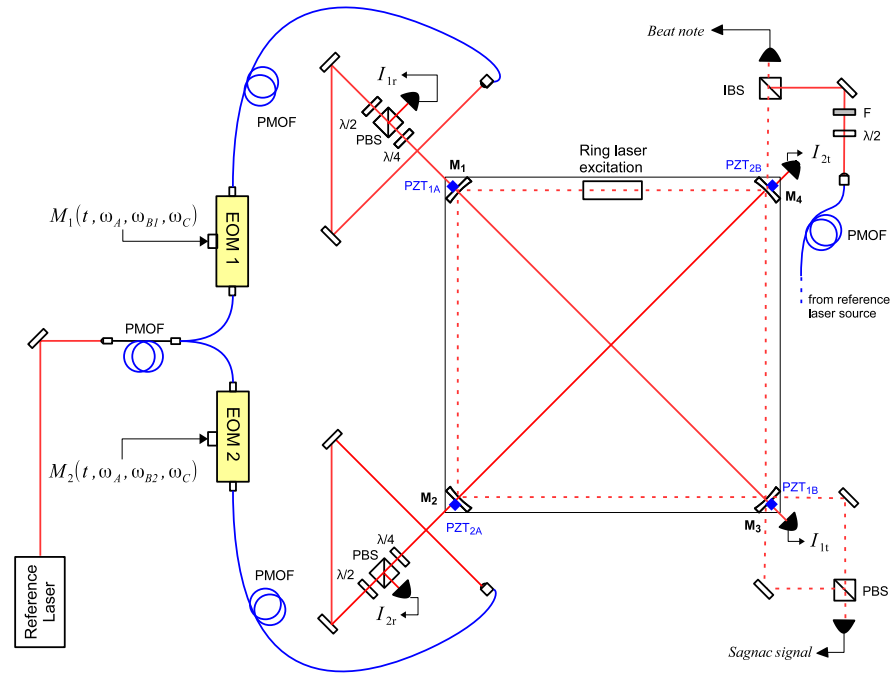


Figure 1.8: Optical scheme of the GP2 experimental apparatus. The triple frequency modulation signals can be seen as the inputs to the EOMs. EOM: electro-optic modulator, PBS: polarizing beam-splitter, IBS: intensity beam-splitter, PMOF: polarization-maintaining optical fiber, $\lambda/2$, half-wave plate, $\lambda/4$: quarter-wave plate, PZT: piezo-electric transducer, F: neutral filter.

apparatus with the main purpose of studying the low frequency rotational motion of the LNGS, in order to validate this site for the future installation of GINGER. GINGERino is located south of the node B, far from human activities occurring in the laboratory. In principle, this apparatus would be able to measure the polar motions and other relevant geodetic signals associated to Earth rotations, as well teleseismic events and micro-seismic activity of the Earth that are relevant for geophysics. The instrument is made of a square optical cavity of $3.6m$ side formed by four high reflectivity mirrors. The cavity is mounted on a cross granite structure rigidly linked to the underlying bedrock. The experimental instrumentation is completed by two seismometers (provided by INGV), two nano-tiltmeters and several environmental monitors (temperature, humidity, pressure, etc.). GINGERino is enclosed in an isolating box with a temperature that can be set in the $13 - 16^\circ C$ range. Even without active control, temperature remains stable at the level of fractions of degrees, with a relative humidity of the order of 60%.

The basic hardware of GINGERino has been completed at the beginning of 2015. Since then, several mechanical improvements have been adopted in order to make stiffer the supports of the cavity mirrors and discharge, and to isolate the instrument from the vibration of the box, which, in turns, isolates acoustically the whole apparatus. Figure 1.10 shows a schematic of the experimental setup. The data acquisition is based on a modular and programmable system (PXI-8106, National Instruments Corp., USA). The relevant signals from the RL, namely mono-beam intensities, interferogram, gain monitor and UTC (Coordinated Universal Time) synchronization signal, are acquired at $5kHz$, while the auxiliary channels (temperature, humidity,



Figure 1.9: Detail of a corner mirror of the GINGERino experiment at LNGS

local tilts, etc.) are acquired at 1 Hz . Data files are created hourly and sent to a PC, which takes care of copying the files directly to a dedicated storage area in Pisa for subsequent analyses. So far a consecutive data set of more than a week has been acquired.

The preliminary analysis has shown a sensitivity about 0.1 nrad/s for 1 s of integration time, compatible with the shot noise level [58]. At present, the main limitation comes from the backscatter noise due to mirror losses, which are a factor of 10 higher than losses of top quality mirrors. After offline correction of f_{BS} , a maximum resolution of about 30 prad/s for 500 s of integration time has been obtained. The correlation between the observed instabilities of the gyroscope and the environmental parameters fluctuation (temperature, pressure, humidity, anthropic activities) is now under investigation.

1.4 MULTI-AXIAL RING-LASERS: GINGER

The purpose of the “Gyroscopes IN General Relativity” (GINGER) experiment is to measure the relativistic components of the gravitational field of the Earth at 1% or better accuracy level, by means of an array of large ring-lasers. A first proposal in 2011 was presented based on an octahedral or cubic configuration [6]. The three-dimensional array would permit to reconstruct the modulus of the total angular rotation vector Ω in the laboratory. The Ω_B and Ω_G terms would be evaluated by subtracting from Ω the Earth rotation rate value Ω_{\oplus} , measured independently by the International Earth Rotation and Reference Systems Service (IERS). The proposed approach requires long term stability and very high accuracy, since it would be necessary to subtract the contribution of Ω_{\oplus} , which, as said, is about nine orders of magnitude bigger than the relativistic terms.

As already mentioned, so far the gravitomagnetic field of the Earth has been measured only by spaceborne experiments and the present uncertainty limit is $\sim 5\%$. The experimental goal of GINGER is to measure Ω_B down to 1%, which remains a challenging target. Moreover, GINGER would provide the first measurement of the GR features of the gravitational field on the surface

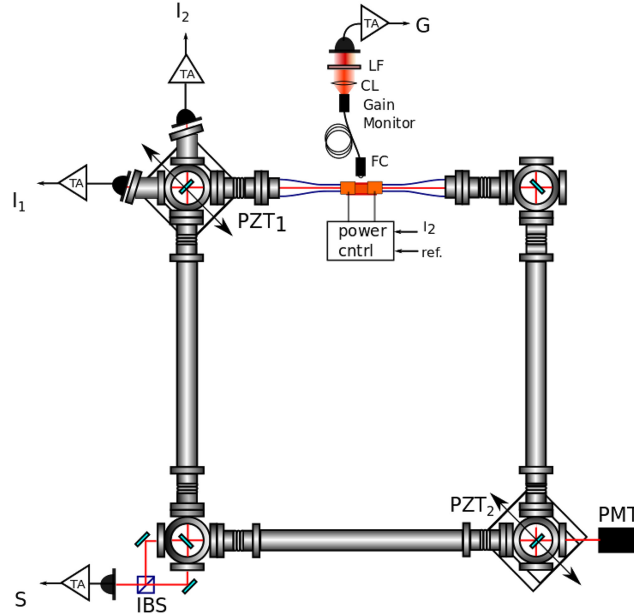


Figure 1.10: Optical scheme of the GINGERino experimental apparatus. Three optical signals are continuously acquired: the combined beams intensity (Sagnac interferogram) S , the two mono-beam intensities I_1 and I_2 and the intensity of the plasma fluorescence G , filtered around the laser line. This last signal is acquired as a monitor of the laser excitation level. IBS: intensity beam splitter, PMT: photo-multiplier tube, LF: line filter (633 nm), TA: transimpedance amplifier, FC = fiber coupler, CL: collimating lens.

of the Earth. Indeed, not being in free fall condition, it would be a direct local measurement independent of the global distribution of the gravitational field. This is one main difference with respect to the space experiments presented in subsection 1.1.1, where the result is the consequence of a long averaging of the effects along the whole orbits.

Before proceeding to the description of some notable features required for the GINGER project, it is worth to mention the presence of another multi-axial array of large RL, which is under development since 2014. The experiment is called ROMY (ROTational Motions in seismology) and is led by the two german institutes, namely LMU Munich and TU Munich, with the financement of the European Research Council (ERC) [59, 60]. The main objective is to make, for the first time, high resolution measurements of broadband rotational ground motions. The target sensitivity of ROMY is 10^{-12} rad/s , which is four order of magnitudes above that required for GINGER. This is because the project scope is not GR; Geophysics and Geodesy are the main field of interests for this research activity. Nevertheless, the cross-validation of the seismic observations made by the two RL arrays would be of great interest in the future. ROMY consists of a tetrahedral set of four independent triangular ring-lasers, each one with a side length of 12 m . The instrument was officially inaugurated in July 2017 and has started data taking. First performance estimations are underway [61, 62].

1.4.1 Requirements

The final desired sensitivity required for GINGER can be inferred by observing the magnitude of the relativistic terms in Equation 1.7. To reach its target of 1% uncertainty on the LT precession value, the array sensitivity must be less than $0.01 \cdot \Omega_B \sim 10^{-16} \text{ rad/s}$. Actually, measuring Ω_B with a ring-laser gyroscope set up horizontally at mid-latitudes requires a sensor sensitivity of around 0.04 prad/s . For comparison, the world's best performing G-ring routinely shows a measurement sensitivity of well below 1 prad/s at 3 h of integration time. However, slowly changing effects in the sensor technique currently limit the sensor stability. This situation is made more difficult by the fact that the LT signal is a very small DC contribution to the overall measurement quantity. Being a small constant signal, it can easily be overshadowed by several potential systematic biases of the instrument, as expressed in Equation 1.5.

A closer look at Equation 1.7 reveals that there are three basic effects one has to carefully account for:

- instantaneous Earth's rotation rate Ω_{\oplus} ;
- orientation \mathbf{n}_A of the gyroscope with respect to the instantaneous Earth's rotation axis;
- stability of the scale factor k_{SF} .

For what concerns the first point, we stated that the estimation of the local frame angular velocity is to be directly compared with the Earth's rotation estimate in the fixed stars reference frame. Nowadays, the best Earth rotation monitoring is provided by the IERS-05C04 time series which are routinely obtained using the geodetic space techniques VLBI (Very Long Baseline Interferometry), SLR (Satellite LASER Ranging), GPS (Global Positioning System), and DORIS (Doppler Orbitography and Radiopositioning Integrated by Satellite). Because of tidal forces and to the exchange of angular momentum between the solid Earth and geophysical fluids, the angular velocity of the Earth varies in time, both in direction and modulus. Changes in modulus correspond to a variation of the length of the day of few milliseconds with respect to atomic clocks, while the direction of the rotation axis of the Earth varies with respect to both the fixed stars and the Earth-fixed reference frames. Currently, IERS measures the Earth rotation rate with an accuracy of $3 \cdot 10^{15} \text{ rad/s}$, which is compatible with a 10% uncertainty on the LT measurement. Therefore the overall errors in LoD and pole position should decrease of a factor 10, that is crucial for a 1% measurement of the relativistic rotation terms. Upgrades in the IERS data uncertainty are expected in the future, even if improvements are not foreseen in the next five years plan [63]. Obviously, prolonging the measurement time T would reduce the uncertainty anyway. A 1 order of magnitude improvement requires $T = 10 \text{ days}$ and of course one must insure the stability of the apparatus over the whole run extension [64].

On the second point, this is the main motivation for the multi-axial design of GINGER. Observing Equation 1.4 it is clear that the angles between vectors \mathbf{A} and Ω must be known at the same level of accuracy requested for the vectors moduli. Since $|\Omega|/|\Omega_{\oplus}| \sim 10^{-9}$ and the requested LT test accuracy is 1%, all parameters in Equation 1.4 should be well known to less than 1 part in 10^{11} . With a single ring-laser experiment, this means asking for the absolute measurement of the area vector \mathbf{A} in the fixed stars reference system with an uncertainty below the nano-radian. This requirement, nearly impossible

to achieve experimentally, can be relaxed using a multi-axial array of RLs, in order to reconstruct the modulus of the Earth rotational vector from multiple scalar measurements. In fact, Ω can be completely measured by means of its projections on at least three independent directions \mathbf{u}_{Ai} . The possible redundant measurement can be used as a monitor and control of the stability of the directions themselves. A further assumption is that ring-lasers have identical sensitivity and noise parameters, which, from an experimental point of view, can be easily satisfied by building the devices with scale factors that differ less than 1%.

Another issue is the differential rotation of the laboratory with respect to the rotation estimated by IERS. In addition to the relativistic terms, Ω contains also an additional component Ω_{loc} which was not mentioned so far. Ω_{loc} accounts for possible microrotations of the crust of the Earth. This is one of the causes limiting the performances of the G-ring in Wettzell: the Earth crust motion caused by atmospheric changes. In order to minimize this, as well as all other types of environmental noise, GINGER is likely to be installed in a very stable geological environment. A suitable location should be the underground facility of LNGS (Laboratori Nazionali del Gran Sasso, L’acquila, Italy), where the GINGERino prototype is now operating in order to characterize the site.

The third point deals with all the noise sources related to the ring-laser operation itself, which have been already discussed in [subsection 1.2.1](#). More specifically, GINGER needs a reduction of all instrumental errors to less than $0.01 \cdot |\Omega_B|/|\Omega_\oplus| \sim 10^{-11}$. This of course must be guaranteed over the whole duration of the acquisition runs, which will last from days to years, depending on the final sensitivity reached by the instrument. This need for a long-term strict control on the fluctuation of cavity geometry, laser active medium and relative dihedral angles is highly demanding. We focus here the attention on the purely geometrical part of k_n in [Equation 1.5](#), which accounts for the systematics induced by instabilities in the mechanical structure of the ring cavity. In order to monitor the reciprocal positions of the many mirrors which will constitute the array, some solutions have been investigated and are currently under test. More detailed informations on this issue can be found in ??.

1.4.2 Structure

As already stated, N_{RL} co-located RLs arranged in a tri-axial system seems to be a viable way to improve the accuracy of the Ω measurement. Measuring the three components of Ω in all three spatial directions permits to reconstruct the norm of the vector combining together different measurements. If the orientation of the array with respect to the rotation axis of the Earth and the meridian plane are not given, all information that can be retrieved by the experiment is contained in the norm of Ω confronted with the theory. If also the external orientation is given, then the full Ω vector, including the angle with respect to the axis of the Earth, is obtained. In general, using multiple independent rings has several advantages: the statistics would be improved since the shot noise of each ring, in the set of many, is independent of the others. An array of $N_{RL} \geq 3$ co-located rings would have the very interesting feature that the angular rotation vector could be reconstructed with different combinations 3 by 3. The comparison of different results would give information on the systematics of the lasers. Worth mentioning is that

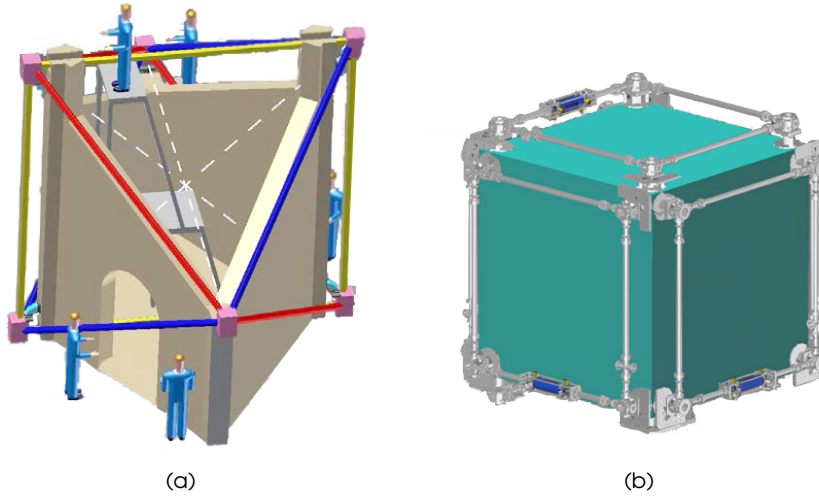


Figure 1.11: Representations of the GINGER apparatus: (a) concept drawing of GINGER's experimental site after implementation of the octahedral configuration and (b) GINGER in cubic configuration.

redundancy is crucial as well in eliminating local rotations, allowing the estimation of the Ω_{loc} contribution.

The first considered configurations for the GINGER array have been the cube and the octahedron, both pictured in Figure 1.11. In particular, the octahedral configuration has been extensively discussed. Three different rings of $p = 6m$ are nested together, sharing 2 by 2 the same mirrors. This configuration has the advantage of imposing inherent constraints in the relative angles between rings, since each mirror is in common between two rings, and three linear Fabry-Pérot cavities are available using the three diagonals of the rings. In principle, those linear cavities have the capability of monitoring the relative angles between different rings, and as well the length of each diagonal, similarly to the GP2 approach. Being a symmetric configuration, the octahedron should be more efficient in the rejection of spurious effects and in the control and monitoring of the relative orientation of the ring-lasers. However, problems related to back-scattering may likely arise because of the mirrors being shared by two ring-lasers. This issue is still to be analyzed and might be critical for the octahedral configuration.

Recently, a simplified $N_{RL} = 2$ array has been proposed as the basic element of a multi-axial system [65]. The ring-lasers have $p = 28m$ and are arranged in a tilted configuration, with one ring-laser laying horizontal and the other one oriented with $\mathbf{n}_A // \Omega_{\oplus}$ ($\approx 45^\circ$ at the LNGS latitude). The experimental apparatus is rather simple and compact. Several arrays could be located at different latitudes, giving the possibility to investigate the response of the RL as function of the latitude. The generalization of the system to three dimensions is possible with the addition of another ring-laser and a system able to monitor the relative angles between the devices. A complete Monte Carlo analysis is also reported, were the target 1% uncertainty on the LT value is linked to the required specifications for the experimental setup.

1.4.3 Geometrical stability

One of the key issues of the GINGER apparatus is its dimensional stability: as for the error budget in [65], the required accuracy for the geometrical scale factor is $\sim 10^{-12}$. This value must be intended as the maximum error variance on the absolute k_{SF} value. In the most optimistic conditions, an absolute knowledge of k_{SF} may not be necessary and the monitoring of relative variations of k_{SF} will be sufficient for the stabilization of GINGER. In either case, the relative positions of the mirrors in the array will need to be stabilized down to the sub-nanometer level.

As seen in subsection 1.3.1, stabilizing the geometry is possible by passive means, such as environmental control, lab sealing, use of materials with low Coefficient of Thermal Expansion (CTE), but becomes increasingly challenging with larger ring sizes and number of rings. Until now, two approaches have been implemented for achieving long-term stabilization of heterolithic ring-lasers. The first technique locks p against a primary frequency standard and was first installed on the G-Pisa ring-laser. The second approach aims to the absolute measure and control of the ring-laser diagonals and is now under development on the GP2 ring-laser. These two experiences made clear that all the information gathered from the inside of a ring-laser cavity is not sufficient to properly constrain the instrument's geometry. Data collected by means of the two above approaches are limited and strictly dependent on the ring-laser dynamics.

Therefore a third approach, based on an external metrology system, was proposed to solve this open issue and is now under development and test. The instrument, called GEMS, represents an alternative metrological approach to measure and control the ring-lasers size and orientation with the required accuracy. The system will be integrated with GINGER RLs but will be independent of their dynamics.

1.5 GINGER EXTERNAL METROLOGY

The GINGER External Metrology System (GEMS), represents a suitable approach to the stabilization of a large heterolithic structure such as that of GINGER. Based on a multiple gauge truss, GEMS will be closely matched to the opto-mechanics of the main instrument to provide real-time measurements of its geometrical frame. It will act as the sensor node of a feedback control loop for the stabilization of the whole structure.

Before proceeding to the description of the instrument concept, we give here a brief description of the most notable example of external metrology truss, developed for the monitoring of a space-born large opto-mechanical structure.

1.5.1 The NASA: SIM case study

The “External Metrology Truss” concept [66, 67] was devised by NASA JPL in the framework of the, by now discontinued, Space Interferometric Mission [68]. This device was supposed to provide reliable distance measurements for the accurate monitoring of the baseline length of a stellar interferometer aimed to planet finding. The truss was made of a network of laser heterodyne interferometers, working together to keep the spacecraft geometry constantly determined with $<10\text{ pm}$ precision.

A common light source was provided by a fiber coupled 1319 nm DPSS laser. Source light was split in half and each part sent to an acousto-optic modulator, where a frequency offset was introduced between the halves. These frequency shifted beams were sent, after proper splitting, to every interferometer via optical fibers. Each interferometer (called *beam-launcher*) layed on a compact and portable Zerodur baseplate, where all the necessary optics were firmly fixed. Each beam-launcher was placed between two of the many fiducials laying on the spacecraft. The fiducials were made by multiple corner-cube retro-reflectors, rigidly connected to appropriate reference points of the truss to be monitored. The measurements along single distances were performed by heterodyne interferometry, a technique which will be described in detail in the next chapter (see [section 2.2](#)) Together with this main displacement monitoring system, there existed some other subsystems working to provide additional features and reliability:

- a frequency tuning system for the laser source, devoted to two-colors interferometry for the determination of the absolute distance between the fiducials [66];
- a pointing dithering system which protected against misalignments of the interferometer with respect to the axis ideally connecting the fiducials [69].

For a detailed description of the beam-launcher we refer to [11].

1.5.2 Locking of GINGER

Basically, the idea was to tailor the SIM concept to the case of GINGER, which is less critical in terms of required dimensional uncertainty, but instead necessitates structural stability in the long-term (days to years instead of minutes). Moreover, GEMS will not be limited to the simple monitoring of the array geometry. The instantaneous displacement measurements will be used to reconstruct the non-ideal array geometry and fed to a closed control loop, which will compensate for any unwanted deformation by adjusting the mirror positions. To this end, all mirrors will be mounted on tri-axial nano-positioners. More in detail, the monitoring of a single array edge is obtained by placing a single gauge in between the couple of array mirrors of interest, with a lateral offset sufficient to guarantee an unaltered ring cavity operation. To this end, a dedicated vacuum system will be necessary for GEMS, in order to guarantee dimensional measurements independent of any ring-laser dynamics. Vacuum operation is required for high precision dimensional measurement, because of the detrimental effects of air index changes in typical ambient conditions (see [subsection 2.4.3](#)). The interrogated fiducial points are represented by low CTE corner-cube retro-reflectors, mechanically bound to each ring-laser mirror and properly characterized prior to and after installation. An extremely precise fiducials characterization will be necessary to avoid misalignment errors (see “Abbe error” in [Sec. 2.4](#)).

If, for instance, the octahedral configuration is chosen for GINGER, every fiducial (one for each vertex) could be ideally composed by a single bulk substrate featuring both the ring-laser super-mirror, which is shared by 3 ring-lasers, and 4 corner-cube retro-reflectors, one for each edge leaving from the given vertex. Then the external metrology truss would be ideally set up by placing 12 compact distance gauges along the corresponding edges of the octahedron, as shown in [Figure 1.12](#).

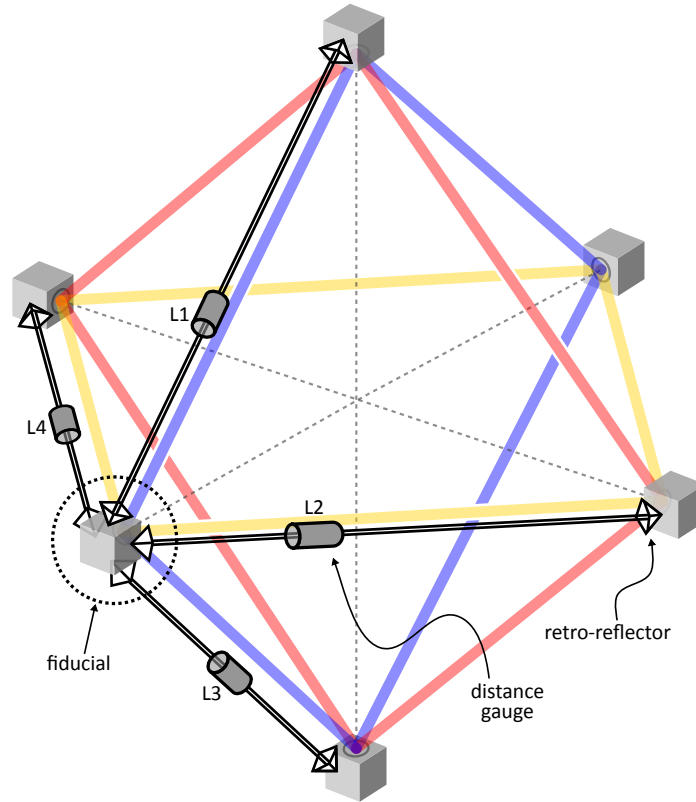


Figure 1.12: Simplified schematic of the external metrology truss matched to GINGER in the octahedral configuration (for a clearer appearance only one complete vertex is showed).

Depending on the number of available interferometers and the type of physically craftable fiducials (either simple one-direction backreflectors, or multidirectional ones), an array of cross measurements can be realized to over-constrain the “stiffness” of the ring-laser array. Moreover, this external truss could be applied both to the control of each single RL and to the monitoring of the angles between different rings. Then, thanks to a detailed mathematical model of the array and a multivariable control scheme, it will be possible to drive suitable nano-positioning actuators to properly move the mirrors and actively control all the relevant dimensions of the cavities. In such a way, it will be possible to keep GINGER’s geometry locked within the required accuracy, independently of any environmental disturbances.

Modularity of the GEMS concept is guaranteed by the presence of a single common laser source, which will provide sufficient light for all the employed gauges. A fiber distribution system will be necessary in order to feed each displacement gauge. This configuration should offer enough flexibility and robustness for an experiment like GINGER. Indeed, changing the number of dimensional observables is possible by moving or adding a displacement gauge without need for reconfiguring the optical layout of either the source or the gauge itself. Moreover, fibers ruggedness will help in incrementing the device durability. We point out that this type of metrological approach can be applied to almost any type of array configuration. For comparison, the solution developed with GP2 is clearly limited to ring cavities offering couples of opposite facing mirrors.

In order to find out the required minimum source power, a power efficiency estimate of the single gauge conducted at first. The *efficiency* parameter is defined as

$$\eta_j = \frac{P_{Oj}}{P_{LAS}}, \quad (1.11)$$

where P_{Oj} is the average optical power hitting the final detector j and P_{LAS} is the common source power. Even if an accurate evaluation of the total efficiency was not possible at the initial development stage, a rough estimate for the single gauge efficiency turned out to be $\eta = 1.3\%$. This value can be obtained by considering the typical transmission coefficients and coupling factors of all the components visible in [Figure 3.19](#) (see [chapter 3](#) for details), as reported from the manufacturers' datasheets. A conservative $\times 0.1$ factor was added to the computation. The original 13% result looks quite optimistic if compared to the actual efficiency of the built system, which turned out to be $\eta_R = 3.27\%$ and $\eta_M = 0.596\%$, for the measurement and the reference paths respectively. This is due to the large contribution of diffraction to the power losses, which was not considered at first and will be extensively discussed in [chapter 3](#). The desired minimum $P_{O,min}$ is determined as

$$\begin{aligned} P_{O,min} &= SNR_{min} \cdot NEP_{typ} \cdot \sqrt{B_{typ}} \\ &= 10^4 \cdot 1 \text{ pW}/\sqrt{\text{Hz}} \cdot \sqrt{1 \text{ MHz}} = 100 \mu\text{W}, \end{aligned} \quad (1.12)$$

where $SNR_{min} = 10^5$ is imposed to guarantee a limiting displacement resolution of $\lambda/SNR_{min} \approx 1 \mu\text{m}/10^5 = 0.01 \text{ nm}$. Indeed, by ignoring laser noise and considering only classical noise from the detector, the limiting resolution of a displacement interferometer may be shown to be inversely proportional to its SNR [70]. The GINGER experiment foresees an array of at least two square ring-laser, $N = 8$ mirror locations, which gives a total of $N_{tot} = N(N - 1)/2 = 28$ possible critical distances to be monitored. Assuming equal power distribution to all 28 gauges, we get

$$P_{LAS} \geq \frac{1}{\eta_{half}^{\text{ceil}(\log_2(N_{tot}))}} \frac{P_{O,min}}{\eta} \approx 750 \text{ mW} \quad (1.13)$$

where $\eta_{half} = 0.4$ accounts for a power halving stage represented by a fiber splitter (FS); typical insertion losses of fiber splitter (0.7 dB) and mating sleeves (0.5 dB) are considered. Clearly, the above estimation is only approximate and the real required power will heavily depend on the final array configuration chosen for GINGER. The total number of ring cavities is still to be determined. Moreover, although redundancy will be fundamental in the determination of GINGER geometry, it is unlikely that a number of gauges equal to N_{tot} will be implemented. A thorough approach to the optical power budgeting for a system of this type can be found in [71].

The first challenge towards the implementation of the GEMS design was the construction and characterization of its fundamental element, i.e. a compact heterodyne displacement interferometer. The scientific activities related to the development of this displacement gauge are presented in the following chapters.

2

DISPLACEMENT INTERFEROMETRY

Since its first commercial launch in 1970 [72], the heterodyne laser interferometer has been a widely applied metrological instrument for more than four decades. It affords to measure distance variations with subwavelength precision both in static and dynamic conditions of the target. Its wide dynamic range and high signal-to-noise ratio successfully responded to the increasing demand for highly accurate measurements in many different industrial fields, e.g. precision machining [73, 74], nanotechnology [75], photolithography and semiconductor manufacturing [76]. Moreover, being based on the interference of light, the heterodyne interferometer offers direct traceability to the length standard and for this reason it has become the instruments of choice for position measurements at the national metrology institutes [77]. Also many past and present advanced scientific activities have taken advantage of heterodyne interferometry as a reliable method to obtain sub-nanometer dimensional knowledge: ground-based and space-born stellar interferometers devoted to the detection of exoplanets which required accurate baseline monitoring [78, 79], dilatometry for aerospace materials testing [80], tracking of inter-spacecraft distances for space missions dedicated to the detection of gravitational waves [81] or to the mapping of the Earth's gravity field [82], etc. The increasing requirements dictated by cutting edge applications are pushing resolution and speed of displacement measuring interferometers to constant improvements [83, 84]. Nevertheless, even the state-of-the-art heterodyne interferometers are susceptible to various error sources. Noise may be optical, mechanical or electrical in nature and must be identified and eliminated, or corrected, in order to achieve the best performances. The environment is also a big actor in limiting the final system repeatability and accuracy. Temperature changes, vibrations and air turbulence are usually the main error contributors when measurements are taken in typical atmospheric conditions.

This chapter first deals with some of the basic concepts of interferometry and their application to displacement metrology. After a brief introduction on the homodyne and heterodyne configurations, the concept of *cancelable circuit* is presented and analyzed. Two widely applied techniques for phase retrieval are described, with focus on their implementation in a real experimental setup. Finally, a wide discussion opens on the many possible error sources which can affect a heterodyne displacement interferometer. An analytic expression is given for each introduced error, together with its related uncertainty and its role in the comprehensive error model of the displacement gauge.

2.1 BASIC INTERFEROMETRY

The essence of displacement interferometry is to measure the phase of an optical wave as a target reflector is moved, and to infer its displacement with respect to the known wavelength λ of the laser used: usually a phase advance

of 2π corresponds to a displacement of λ or $\lambda/2$, depending on the specific optical configuration.

We consider an unbalanced Mach-Zehnder interferometer as the one showed in Figure 2.1a. The laser source is assumed to be ideally monochromatic and linearly polarized. Its electric field E as function of time t can be described as

$$E(t) = E_0 \exp \{i2\pi\nu t\} , \quad (2.1)$$

with E_0 the amplitude and ν the optical frequency. In the interferometer a beam-splitter (BS) splits the light into two branches. In the long arm (arm 2) the light is delayed with respect to the short arm (arm 1) by an amount τ and then gathers a phase delay $\varphi = 2\pi f\tau$. Then we can write the electric field contributions of the two arms at the recombination point:

$$E_1(t) = E_{01} \exp \{i2\pi\nu t\} \quad (2.2)$$

$$E_2(t) = E_{02} \exp \{i2\pi\nu t + \varphi\} , \quad (2.3)$$

where E_{01} and E_{02} are constants, related to E_0 , which account for the power splitting and other losses inside the BS. A second beam-splitter recombines the two beams and the resulting optical power is measured with a detector. Summing and squaring of the two fields yields a quantity proportional to the optical power P which is hitting the detector. To be more specific, the underlying hypothesis is of uniform optical intensity I over the detector active area A , such that $P(t) = AI(t)$. Moreover, the optical intensity (or, more correctly, *irradiance*) and the electric field strength E are related by $I = |\langle S \rangle| = (1/2)n\epsilon_0 c|E|^2$, which corresponds to the absolute value of the time-averaged Poynting vector of a monochromatic plane wave. Then we can write

$$\begin{aligned} P(t) \propto |E_1(t) + E_2(t)|^2 &= |E_1(t)|^2 + |E_2(t)|^2 + \overline{E_1(t)} E_2(t) + E_1(t) \overline{E_2(t)} \\ &= |E_1(t)|^2 + |E_2(t)|^2 + E_{01} E_{02} (e^{i\varphi} + e^{-i\varphi}) \\ &= |E_1(t)|^2 + |E_2(t)|^2 + 2E_{01} E_{02} \cos(\varphi) , \end{aligned} \quad (2.4)$$

which explains the light and dark fringes appearing in any interferometer when one changes the path length of either one of its arms. Therefore, the phase φ is directly related to the optical path difference 2ℓ between the two branches and can be written as

$$\varphi = \frac{2\pi}{\lambda} 2\ell = \frac{2\pi\nu}{c} 2\ell , \quad (2.5)$$

where $\lambda = c/\nu$ is the radiation wavelength. Clearly, this linear relation between length and phase is valid within a full phase period. Indeed, the interferometer, as simple as presented, cannot give information about the N integer number of wavelengths corresponding to the absolute pathlength difference between arm 1 and arm 2.

2.2 HETERODYNE INTERFEROMETRY

The optical heterodyne method is based on the creation and recombination of two laser beams with different optical frequencies. Creating frequency shifted beams is possible by means of an optical modulator inserted along one of the interferometer branches. An acousto-optic modulator (AOM) or an electro-optic modulator (EOM) are usually used. AOM and EOM are based

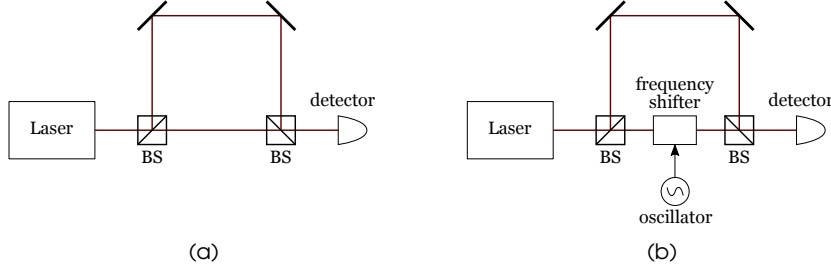


Figure 2.1: Comparison between homodyne and heterodyne interferometry: (a) homodyne scheme; (b) heterodyne scheme.

respectively on the acousto-optic effect and the electro-optic effect and both can shift the optical frequency using an input RF signal with a frequency f_{het} in the range of 30 MHz to 100 GHz [85]. The resulting interference pattern on the detector will be time-varying and periodic, with frequency f_{het} . With respect to its homodyne counterpart, heterodyne interferometry offers many inherent advantages [86], even though it requires more complex hardware and software assemblies to properly modulate and demodulate ac signals. Worth mentioning are its built-in directional sensitivity, the better noise immunity and its wide dynamic range.

Based on the specific application, many optical configurations are possible, even though the underlying principle stays the same. We refer now to the simple layout of Figure 2.1b, but we will switch soon to that of Figure 2.2a because it better represents the experimental setup described later in chapter 3. In this second representation two AOMs are present on both arms of the interferometer. This configuration is required to obtain a beat signal whose frequency can be easily processed with detection and acquisition electronics in the kHz range. To this end the AOM in arm 1 is driven at frequency f_1 , while the AOM in arm 2 works at $f_2 = f_1 + f_{het}$. Now f_{het} can easily be tuned from 0 Hz to several MHz within the modulators best working ranges.

The electric fields \mathbf{E}_j of two linearly polarized light beams can be described as:

$$\mathbf{E}_j(\mathbf{r}, t) = E_j \mathbf{p}_j \exp \{ i [2\pi \nu_j t + \varphi_j + \varphi_{rj}(\mathbf{r})] \} , \quad (2.6)$$

where $j = 1, 2$ identifies the interfering beam, \mathbf{p}_j determines the polarization direction, E_j is the electric field amplitude, and $\varphi_{rj}(\mathbf{r})$ is the spatial distribution (with zero mean) of wavefront phase at the detector location. The interference signal intensity $I(\mathbf{r}, t)$ oscillates at the heterodyne frequency $f_{het} = \nu_2 - \nu_1$ and is proportional to $|\mathbf{E}_{tot}(\mathbf{r}, t)|^2$, where $\mathbf{E}_{tot} = \mathbf{E}_1(\mathbf{r}, t) + \mathbf{E}_2(\mathbf{r}, t)$ is the interference pattern hitting the detector. In the ideal case of identically shaped wavefronts $\varphi_{r1}(\mathbf{r}) = \varphi_{r2}(\mathbf{r})$ and assuming matched polarization vectors $\mathbf{p}_1 = \mathbf{p}_2$, the detected heterodyne signal can be described as:

$$I(t) = I_0 [1 + C \cos (2\pi f_{het} t + \varphi)] , \quad (2.7)$$

where I_0 is the average intensity and C defines the beating contrast (also called *fringe visibility*). The contrast will be directly related to the wavefronts flatness, i.e. to how φ_{rj} will be close to a constant null value. The phase offset

$$\varphi = \varphi_2 - \varphi_1 \quad (2.8)$$

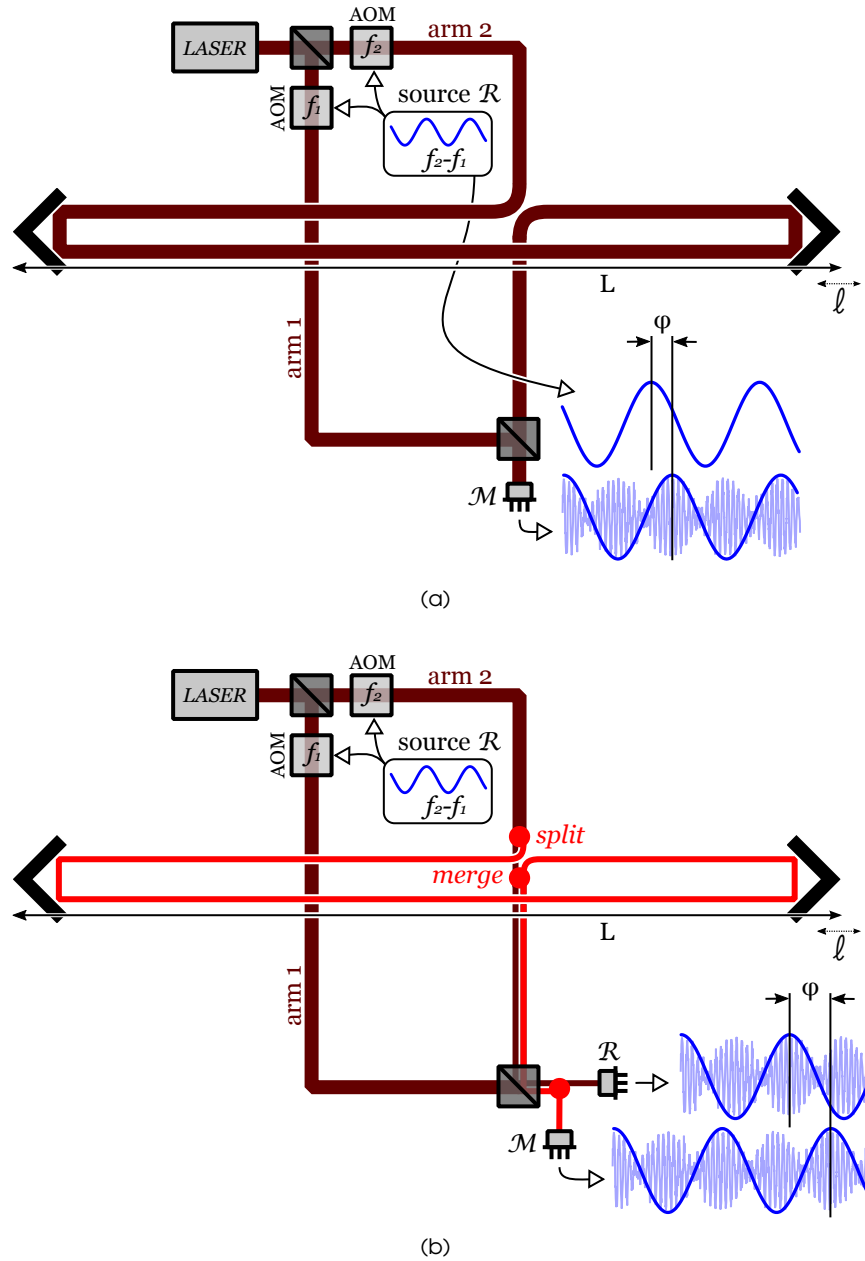


Figure 2.2: Simplified layout of a heterodyne displacement interferometer: (a) standard scheme; (b) added cancelable circuit (red path). Folding of arm 2 is required for proper interrogation of the distance L .

carries the information about the pathlength difference 2ℓ between the arms of the interferometer (net of an N integer number of wavelengths):

$$2\ell = \frac{\lambda}{2\pi} \varphi, \quad (2.9)$$

which is the same relation expressed in Equation 2.5.

2.2.1 The cancelable circuit

The interference of two beams produces one beat signal and consequently one displacement can be calculated with Eq. 2.9. However, two optical paths will be fluctuated independently by different causes, preventing the identification of the real displacement, which is the net optical path change in either one of the two arms. In order to suppress such fluctuations and obtain a high-precision displacement value, the system must introduce an additional interference signal. Two beats have to be generated by the recombination of four beams, in a configuration called *cancelable circuit* [85, 87].

Figure 2.2a shows a heterodyne interferometer in Mach-Zehnder configuration. One of its arms is folded twice more than usual to let the beam travel a distance L , defined by a couple of retro-reflective fiducials. The interferometer is thus designed to be placed in between the fiducial points. This layout was specifically selected as being the simplified model of the experiment described in the following sections. Nevertheless, all considerations apply rather loosely to any kind of two-beam interferometer whose ideal output is a sinusoidal signal. For instance, the same applies to Michelson configurations, where the beams are split and recombined by the same optical element and the beam enclosed area is zero. The system has just one optical output, which is compared to an external electrical reference for phase retrieval. By contrast, Figure 2.2b shows the same interferometer with added a cancelable circuit: by splitting the second arm in two separate parts we define a *reference beam* \mathcal{R} and a *measurement beam* \mathcal{M} , both at frequency f_2 . \mathcal{R} goes straightforward to the recombination point and interferes with its counterpart at frequency f_1 : this reference beat I_R is collected by a suitable photo-detector. \mathcal{M} travels along the distance to be monitored and then merges back into the \mathcal{R} path. In doing this, \mathcal{R} and \mathcal{M} must be kept separate to avoid optical crosstalk (see Sec. 2.4). \mathcal{M} finally reaches the recombination point and, as well as \mathcal{R} does, interferes with its f_1 counterpart: this second measurement beating I_M is properly separated and collected by a second dedicated detector. The phase offset φ between I_M and I_R results from applying Eq. 2.8 to both signals:

$$\varphi_R = \varphi_{2R} - \varphi_{1R} \quad (2.10)$$

$$\varphi_M = \varphi_{2M} - \varphi_{1M} \quad (2.11)$$

$$\begin{aligned} \varphi &= \varphi_M - \varphi_R \\ &= (\varphi_{2M} - \varphi_{1M}) - (\varphi_{2R} - \varphi_{1R}) \\ &= \varphi_{2R} + \frac{2\pi}{\lambda} 2\ell - \varphi_{1R} - \varphi_{2R} + \varphi_{1R}, \end{aligned} \quad (2.12)$$

where $\varphi_{1M} = \varphi_{1R}$ by construction, because both phase terms are identically related to pathlength changes in arm1; similarly φ_{2M} is equal to $\varphi_{2R} + (2\pi/\lambda)2\ell$, being \mathcal{R} and \mathcal{M} identical except for the distance $2L = N\lambda + 2\ell$. This two facts are responsible for the effectiveness of the, though more complex, cancelable circuit design. Any perturbation affecting arm 1 (φ_{1M}) or arm 2 (φ_{2M}) changes

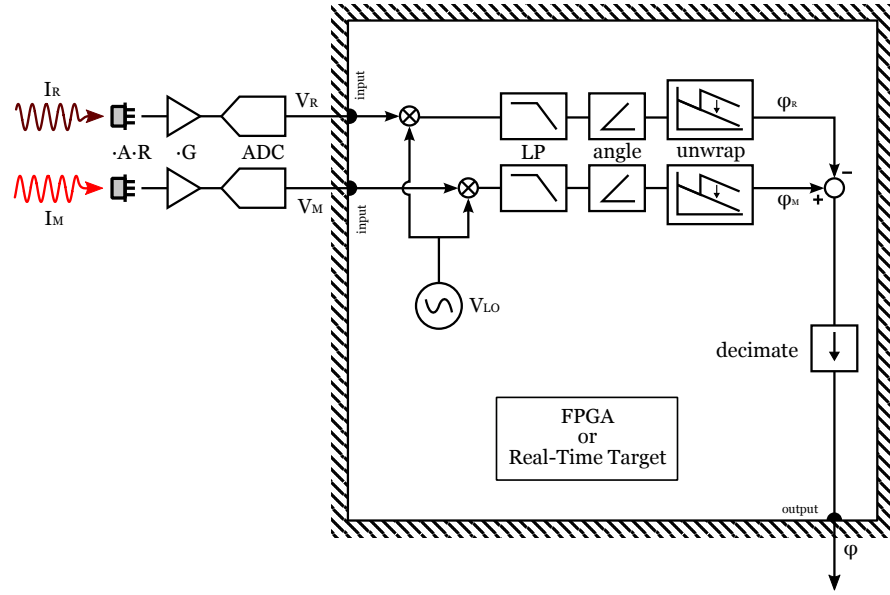


Figure 2.3: Schematic representation of the system for interferometric signals acquisition and phase retrieval (lock-in detection).

both ϕ_M and ϕ_R by the same amount, leaving ϕ unaltered. In other words, any fluctuation happening outside the interrogated distance is converted into common mode noise, which is inherently rejected by a differential measurement. Therefore, following from Eq. 2.12, the resulting displacement for the cancelable circuit design can be written as:

$$2\ell = \frac{\lambda}{2\pi} \phi, \quad (2.13)$$

which resembles Eq. 2.9, but with a clear different definition for ϕ .

2.3 PHASE RETRIEVAL METHODS

As stated before, the goal in interferometry is usually to obtain a phase, based on the measurement of an optical power. Clearly this is not possible with a single power measurement, since Equation 2.7 and Equation 2.4 have no unique solution. Therefore, to properly reconstruct the desired phase, at least two interferometric measurements are necessary.

In a heterodyne interferometer, once the beat signals are properly amplified, converted to voltage and digitized, the phase offset between them has to be retrieved in order to reconstruct the fiducials relative displacement. If the hypotheses of section 2.2 about the interfering beams still hold true, the voltage signals from the experiment can be described as

$$V_j(t) = G_j R_j A_j I_j(t), \quad (2.14)$$

where $j = R, M$ identifies the interference signal, $I_j(t)$ is the detected optical intensity as defined in Eq. 2.7, G_j is the transimpedance gain of the readout am-

plifier, A_j and R_j are, respectively, the detector's active area and responsivity at λ . By substituting Eq. 2.7 in Eq. 2.14, one obtains

$$V_j(t) = G_j R_j A_j I_{Oj} [1 + C_j \cos(2\pi f_{het} t + \varphi_j)] \quad (2.15)$$

and, by defining $V_{Oj}(t) = G_j R_j A_j I_{Oj}$, $V_{Cj} = V_{Oj} C_j$ and $\Phi_j(t) = 2\pi f_{het} t + \varphi_j$, we can rewrite

$$V_j(t) = V_{Oj} + V_{Cj} \cos(\Phi_j(t)) . \quad (2.16)$$

Two widely used phase retrieval methods are described in the followings: the zero-crossing detection scheme and the lock-in detection scheme. Nevertheless, many other techniques, both analogue and digital, do exist for retrieving a phase offset between two nominally sinusoidal signals [88, 89]: dedicated lock-in amplifiers, discrete Hilbert transform, time domain cross-correlation, etc.

2.3.1 Zero-crossing detection

The zero-crossing method acts in the time domain and consists of directly measuring the time lag between the instants in which the two signals of interest cross a predefined voltage level. This voltage level is usually zero and requires the two signals to be high-pass filtered before acquisition. The zero-crossing detection can ideally be implemented with simple comparator circuitry [90], even though, if high accuracy levels are requested, careful attention must be paid to all phasemeter components and to the characteristics of the input signals. Amplitude noise, changing in the signal slew-rates and instabilities of the reference voltage levels can severely spoil this type of phase measurement [91].

If we consider the input voltage signal of Equation 2.16, the (absolute) zero-crossing instant t_j reads

$$[V_j(t_j)]_{HP} = 0 \quad (2.17)$$

$$V_{Cj} \cos(\Phi_j(t_j)) = 0$$

$$\Phi_j(t_j) = \frac{\pi}{2}$$

$$t_j = \frac{(\frac{\pi}{2} - \varphi_j)}{2\pi f_{het}} , \quad (2.18)$$

where the $[\cdot]_{HP}$ notation is used to indicate the process of high-pass filtering of the argument. In this case we refer to simple ac coupling of the voltage signals, in order to remove the component V_{Oj} at $f = 0$. The detected phase is then

$$\hat{\varphi}_j = \frac{\pi}{2} - 2\pi f_{het} t_j , \quad (2.19)$$

where the “hat” notation specifies, here and from now on, an estimation (from experimental measurements) of the real value. The same procedure applies to $V_R(t)$ and $V_M(t)$ and can be used to reconstruct the phase offset between them.

2.3.2 Lock-in detection

The lock-in detection method is based on the effects of multiplying complex exponentials representing oscillating signals. Formerly, the multiplication task

was usually performed by a non-linear electronic device, such as the analog mixer of a superheterodyne receiver. Now it can be implemented digitally with ease, giving better results in terms of flexibility, performance and noise. As a matter of fact, many standalone phasemeters nowadays on the market offer fully digital realizations of the lock-in detection scheme.

Again taking the voltage input signals of Equation 2.16, we offer here an analytic description of the algorithm. An internal signal $V_{LO}(t) = \exp(2\pi f_{het}t) = \exp(\Phi_O(t))$ is generated and used as reference for proper signals manipulation (dependence from t is omitted for clarity):

$$\begin{aligned} V_j V_{LO} &= \left[V_{Oj} + \frac{V_{Cj}}{2} (e^{i\Phi_j} + e^{-i\Phi_j}) \right] e^{\Phi_{LO}} \\ &= V_{Oj} e^{i\Phi_O} + \frac{V_{Cj}}{2} e^{i(\Phi_{LO} + \Phi_j)} + \frac{V_{Cj}}{2} e^{i(\Phi_{LO} - \Phi_j)}, \end{aligned} \quad (2.20)$$

where the first two complex exponentials are oscillating respectively at frequencies f_{het} and $2f_{het}$. The last term is the result of a baseband frequency translation, that is $\Phi_{LO} - \Phi_j = 2\pi f_{het}t - 2\pi f_{het}t - \varphi_j$. Therefore, by proper low-pass (LP) filtering, the resulting signal is

$$[V_j V_{LO}]_{LP} = \frac{V_{Cj}}{2} e^{-i\varphi_j} \quad (2.21)$$

and its phase can be easily extracted:

$$\hat{\varphi}_j = -\arctan\left(\frac{\text{Im}\{[V_j V_{LO}]_{LP}\}}{\text{Re}\{[V_j V_{LO}]_{LP}\}}\right), \quad (2.22)$$

The above described method substantially performs a quadrature phase demodulation on a collected optical beating and must be applied twice, both to $V_R(t)$ and $V_M(t)$.

All the operations can be implemented digitally on a PC, for post-processing of acquired data, or on a FPGA or a real-time OS, for online data acquisition and processing (Figure 2.3).

2.4 ERROR SOURCES

The heterodyne method for displacement measurements is affected by various error sources. These error sources can be generally classified into three categories: random errors, systematic errors and environmental errors.

2.4.1 Random

Random errors are caused by many random noise sources and cannot be completely eliminated, even though they can be reduced by acting on some specific experimental parameters. These errors come from photon shot noise on the detectors, electronic noise from drivers and amplifiers, ADC quantization, etc. A formulation of the instantaneous random error $\epsilon_{\ell,x}$ affecting a single displacement measurement is reported in Table 2.1, where x is the physical quantity affected by the random error and ϵ_x is its associated uncertainty. The expressions presented require many input parameters, which are defined as follows: λ_0 is the source vacuum wavelength, q is the electronic charge, B is

Table 2.1: Mathematical expressions for the random errors affecting a heterodyne displacement gauge.

Error source	Analytic expression	Ref.
laser freq. noise	$\epsilon_{\ell,\lambda_0} = \frac{\epsilon_{\lambda_0}}{\lambda_0} \ell = \frac{\epsilon_v}{v} \ell$	Eq. 2.13
voltage noise	$\epsilon_{\ell,V} = \frac{\lambda}{4\pi} \sqrt{\frac{\epsilon_{V_R}^2}{2V_{OR}^2} + \frac{\epsilon_{V_M}^2}{2V_{OM}^2}}$	Eq. 2.22, Eq. 2.13
photon shot noise	$\epsilon_{V_j,shot} = \sqrt{2q V_{Oj} B_j G_j}$	[92]
detector noise	$\epsilon_{V_j,det} = R_j G_j NEP_j \sqrt{B_j}$	[93]
amplifier noise	$\epsilon_{V_j,amp} = \sqrt{4k_B T_{nj} G_j} \sqrt{B_j}$	[93]
quantization noise	$\epsilon_{V_j,qtz} = \frac{1}{\sqrt{12}} \left(\frac{\Delta V}{2^b - 1} \right)$	[94]
sampling jitter	$\epsilon_{V_j,jit} = 2\pi f_{het} \tau_{jit} \frac{V_{Oj} C_j}{\sqrt{2}}$	[95]

the detection bandwidth, NEP is the noise equivalent power of the detector, k_B is the Boltzmann constant, T_n is the amplifier noise temperature, ΔV is the ADC input voltage range, b is the bit depth of the ADC, τ_{jit} is the maximum jitter value for the acquisition system.

Because of the nature of random noise, the total gauge error reduces when data are integrated for longer periods of time. Clearly, this is true as long as the considered noise has a white spectral distribution. Actually, if N instantaneous displacement measurements are averaged over the period T , the resulting gauge error reads

$$\langle \epsilon_{\ell,x} \rangle = \frac{\epsilon_{\ell,x}}{\sqrt{N}} = \frac{\epsilon_{\ell,x}}{\sqrt{f_s T}}, \quad (2.23)$$

where f_s is the sampling frequency.

2.4.2 Systematic

This result does not apply to systematic errors, which instead can be greatly reduced or even eliminated by proper modeling and tuning of the experiment. Three are the main error sources of this type: optical crosstalk, free-space diffraction and misalignments.

Optical crosstalk occurs when the reference and the measurement beams partially mix each other before the recombination point. This fact causes the so called *cyclic error*, which is a displacement dependent non-linear error, periodic of period $\lambda/2$ (Fig. 2.4). The cyclic error is a well-known limitation factor for the sensitivity of heterodyne interferometers at the nanometer and sub-nanometer scale. A comprehensive list of references dealing with this issue can be found in [96]. As in the most standard designs, when \mathcal{M} and \mathcal{R} are coded into orthogonal polarization states, any defect in polarizing optics can cause power leakages of one state into the other, with difficult improvement below -30 dBc , due to limitations in materials performances, system alignment and stability [97–100]. For instance, an intrinsic limit can be found in the optical properties of polarizing materials, given that their extinction ratios highly depends on manufacturing and environmental conditions, two factors which cannot be kept under sufficiently fine control. Alternative non-polarizing solutions have been developed to overcome this problem [9, 10, 101–106].

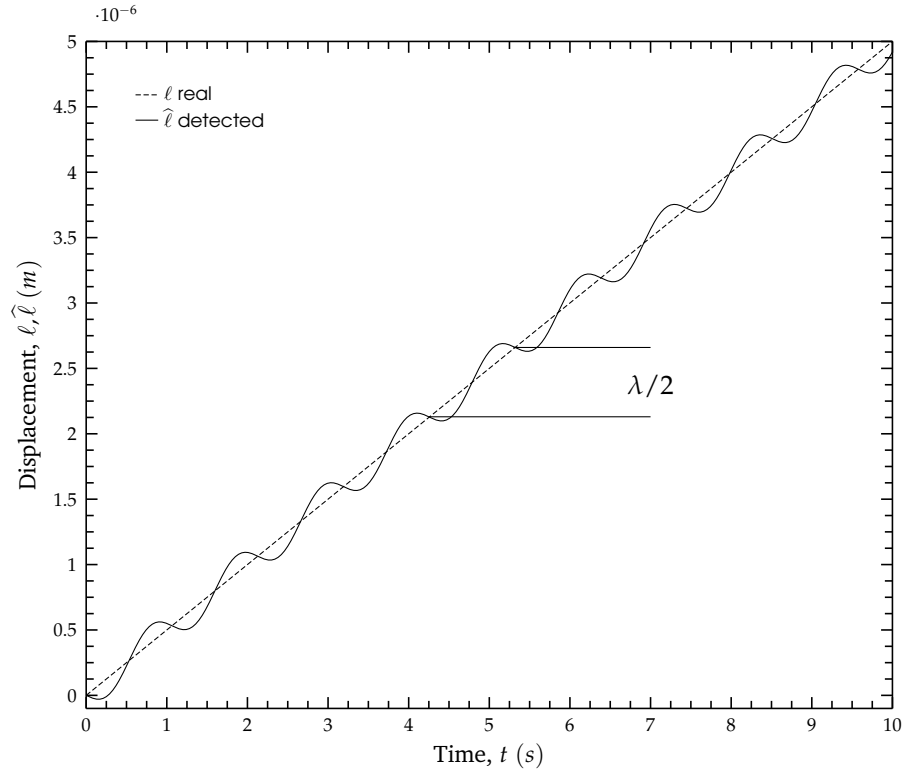


Figure 2.4: Output of a displacement gauge affected by cyclic non-linearity: the dashed line represent the ideal interferometer output; the solid curve is the measured displacement (exaggerated).

Among others, the separation of \mathcal{M} and \mathcal{R} by wavefront splitting has been demonstrated as an optimal workaround [11, 107]. Wavefront division by holey mirrors, supported by beam masking [108] and detailed modeling of diffraction at apertures [109, 110], can lead to reductions of the cyclic error down to the picometer level, which is associated to power leakages lower than -90 dBc . Worth noticing is that the same kind of cyclic error can be generated by other types of crosstalk between the reference and the measurement channels: optical crosstalk inside the heterodyne source or in the interferometer induced by scattering [111], ghost reflections [112] and back reflections [113], electrical crosstalk in RF electronics [114] and readout amplifiers [91, 115, 116], non-linear errors in the detection scheme due to hardware and software implementations [91, 117, 118].

In presence of crosstalk between the two gauge channels, the acquired voltage signals can be written as

$$V_R(t) = V_{OR} + V_{CR} \cos(\Phi_R(t)) + V_{LM} \cos(\Phi_M(t)), \quad (2.24)$$

$$V_M(t) = V_{OM} + V_{CM} \cos(\Phi_M(t)) + V_{LR} \cos(\Phi_R(t)), \quad (2.25)$$

where V_{LR} is the amplitude of the reference signal leaking into the measurement channel and V_{LM} is the amplitude of the measurement signal leaking into the reference channel.

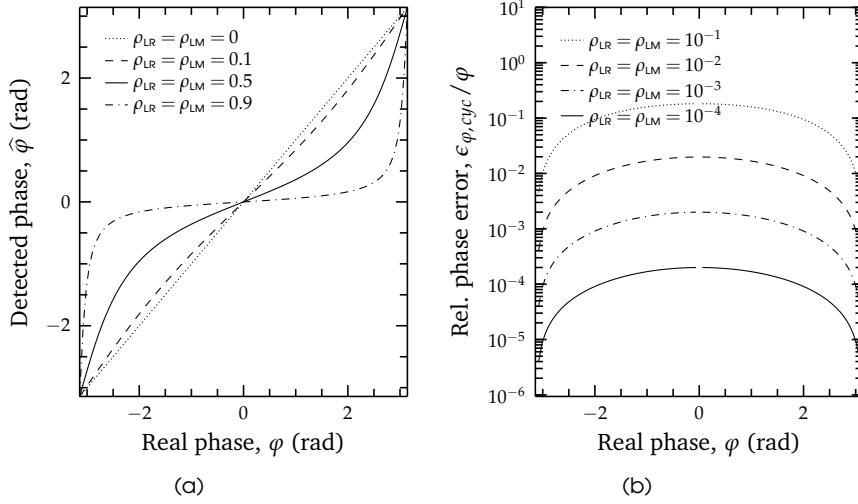


Figure 2.5: Simulated cyclic error over a displacement period, computed for different levels of leakage between \mathcal{R} and \mathcal{M} : (a) detected phase and (b) relative phase error.

In the case of zero-crossing phase detection we can substitute Equation 2.24 in Equation 2.17 and evaluate the zero-crossing instant:

$$\begin{aligned}
 0 &= V_R(t_j) = V_{OR} + V_{CR} \cos(\Phi_R(t_j)) + V_{LM} \cos(\Phi_M(t_j)) \\
 t_j &= \left[\frac{\pi}{2} - \arcsin \left(\frac{V_{CR} \sin \varphi_R + V_{LM} \sin \varphi_M}{\sqrt{V_{CR}^2 + 2V_{CR} V_{LM} \cos(\varphi_M - \varphi_R) + V_{LM}^2}} \right) \right] \frac{1}{2\pi f_{het}} \\
 &= \left[\frac{\pi}{2} - \arcsin \left(\frac{\sin \varphi_R + \rho_{LM} \sin \varphi_M}{\sqrt{1 + 2\rho_{LM} \cos(\varphi_M - \varphi_R) + \rho_{LM}^2}} \right) \right] \frac{1}{2\pi f_{het}}, \quad (2.26)
 \end{aligned}$$

with $\rho_{LM} = V_{LM}/V_{CR}$. As expected, this formulation simplifies to that of Equation 2.18 for the ideal case of $\rho_{LM} = 0$. The measured phase is obtained by substituting in Equation 2.19 the previous expression for t_j :

$$\widehat{\varphi}_R = \arcsin \left(\frac{\sin \varphi_R + \rho_{LM} \sin \varphi_M}{\sqrt{1 + 2\rho_{LM} \cos(\varphi_M - \varphi_R) + \rho_{LM}^2}} \right), \quad (2.27)$$

which can be approximated to the first order by Taylor expansion at $\rho_{LM} = 0$ turning into

$$\begin{aligned}
 \widehat{\varphi}_R &\approx \varphi_R + \frac{(\rho_{LM} - 0)}{1!} \cdot \left. \frac{\partial \widehat{\varphi}_R}{\partial \rho_{LM}} \right|_{\rho_{LM}=0} \\
 &\approx \varphi_R + \rho_{LM} \frac{1}{\sqrt{1 - \sin^2 \varphi_R}} \left[\sin \varphi_M - \frac{1}{2} \sin \varphi_R \cdot 2 \cos(\varphi_M - \varphi_R) \right] \\
 &\approx \varphi_R + \rho_{LM} \left[\frac{\sin \varphi_M (1 - \sin^2 \varphi_R)}{\cos \varphi_R} - \sin \varphi_R \cos \varphi_M \right] \\
 &\approx \varphi_R + \rho_{LM} \sin(\varphi_M - \varphi_R). \quad (2.28)
 \end{aligned}$$

All the above hold as well for the measurement signal in Eq. 2.25, with $\rho_{LR} = V_{LR}/V_{CM}$. Some error simulations are plotted in Figure 2.5.

A different derivation follows for the case of lock-in detection. By substituting Eq. 2.24 in Eq. 2.22 one obtains

$$\begin{aligned}\widehat{\varphi}_R &= \arctan \left(\frac{V_{CR} \sin(\Phi_O - \Phi_R) + V_{LM} \sin(\Phi_O - \Phi_M)}{V_{CR} \cos(\Phi_O - \Phi_R) + V_{LM} \cos(\Phi_O - \Phi_M)} \right) \\ &= \arctan \left(\frac{\sin \varphi_R + \rho_{LM} \sin \varphi_M}{\cos \varphi_R + \rho_{LM} \cos \varphi_M} \right),\end{aligned}\quad (2.29)$$

The above expression can be approximated to the first order by Taylor expansion at $\rho_{LM} = 0$ (Eq. 12 in [9]), turning into

$$\begin{aligned}\widehat{\varphi}_R &\approx \varphi_R + \frac{(\rho_{LM} - 0)}{1!} \cdot \left. \frac{\partial \widehat{\varphi}_R}{\partial \rho_{LM}} \right|_{\rho_{LM}=0} \\ &\approx \varphi_R + \rho_{LM} \frac{1}{1 + \left(\frac{\sin \varphi_R}{\cos \varphi_R} \right)^2} \cdot \frac{\sin \varphi_M \cos \varphi_R - \sin \varphi_R \cos \varphi_M}{\cos^2 \varphi_R} \\ &\approx \varphi_R + \rho_{LM} \sin(\varphi_M - \varphi_R),\end{aligned}\quad (2.30)$$

which resembles Equation 2.28, found for the zero-crossing case. The same calculation can be done for the measurement signal in Eq. 2.25 with analogous results.

The total cyclic error is defined as $\epsilon_{\varphi, cyc} = \widehat{\varphi} - \varphi$ and reads

$$\epsilon_{\varphi, cyc} = \widehat{\varphi} - \varphi \quad (2.31)$$

$$\begin{aligned}&= (\widehat{\varphi}_M - \widehat{\varphi}_R) - (\varphi_M - \varphi_R) \\ &= (\rho_{LM} + \rho_{LR}) \sin(\varphi_R - \varphi_M),\end{aligned}\quad (2.32)$$

which gives a displacement error of

$$\epsilon_{\ell, cyc} = \frac{\lambda}{4\pi} \epsilon_{\varphi, cyc} = \frac{\lambda}{4\pi} (\rho_{LM} + \rho_{LR}) \sin(\varphi_R - \varphi_M). \quad (2.33)$$

This expression shows analytically what was previously stated about the periodicity and non-linearity of the cyclic error. Moreover, it provides a useful means for the estimation of this type of error from the measured power leakages ρ_{LM} and ρ_{LR} .

Another type of non-linear systematic error is caused by diffraction due to free-space propagation of beams over long distances, which indeed takes the name of *diffraction error*. Real beams are never perfectly flat and their wavefront phase distribution $\varphi_{rj}(\mathbf{r})$ gets modified with the travelled longitudinal distance $2L$. The detected phase results from $\varphi_{rj}(\mathbf{r})$ being averaged over the detector area. This average phase value will then differ from the ideal phase by an ℓ dependent offset, which can, in principle, be modeled and subtracted. This error is a slowly varying function of displacement and its value is in the order of tens of *nm* over many meters displacement range [109, 119, 120]. The diffraction error can thus be neglected if ℓ is limited to ranges of few microns.

A third type of systematic error is that produced by misalignments between the metrology system and the distance to be monitored [121]. The *Abbe error* occurs when the measurement system and the distance L are not coaxial (Figure 2.6). In this case, if the fiducial point translates with a rotation error of θ_{abb} (of uncertainty ϵ_{abb}), then the measured displacement will be affected by an error $\delta_{abb} = d_{abb} \sin(\theta_{abb}) \approx d_{abb} \theta_{abb}$, where d_{abb} (of uncertainty ϵ_d) is the

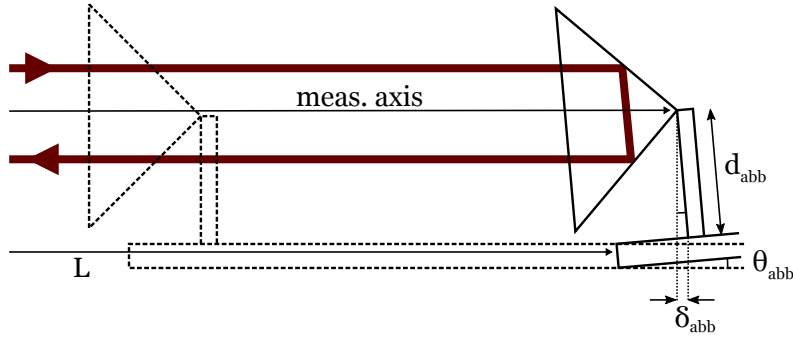


Figure 2.6: Schematic representation of the Abbe error.

offset distance between the L axis and the measurement axis. The associated uncertainty is then

$$\epsilon_{\ell,abb} = \sqrt{\theta_{abb}^2 \epsilon_d^2 + d_{abb}^2 \epsilon_{\theta_{abb}}^2}. \quad (2.34)$$

Figure 2.7 illustrates the *cosine error*: when the measurement axis is not parallel to the displacement axis by an angle θ_{cos} , the measured displacement $\hat{\ell}$ and the actual one ℓ differ by an amount $\delta_{cos} = \ell - \hat{\ell} = \ell(1 - \cos(\theta_{cos})) \approx (1/2)\ell\theta_{cos}^2$, and the resulting uncertainty is

$$\epsilon_{\ell,cos} = \frac{1}{2}\ell\epsilon_{\theta_{cos}}, \quad (2.35)$$

with $\epsilon_{\theta_{cos}}$ being the uncertainty on the angle θ_{cos} .

Another error originated from the measurement system geometry is the *deadpath error*. The deadpath is the full optical path difference between the \mathcal{R} and the \mathcal{M} paths when the interferometer output is zeroed ($2L$ in the layout of Figure 2.2b). If we consider two instantaneous measurements at different times, $\hat{\ell}_0 = \ell_0$ and $\hat{\ell}_1$, the measured displacement $\hat{\ell}$ will be the difference between the two. By expressing these quantities as a function of the deadpath $2L_0$ and using Eq. 2.13 we can write

$$L_0 = \frac{N_0}{2}\lambda + \ell_0 = \lambda \left(\frac{N_0}{2} + \frac{\varphi_0}{4\pi} \right) \quad (2.36)$$

$$L_1 = \frac{N_1}{2}\lambda + \ell_1 = \lambda \left(\frac{N_1}{2} + \frac{\varphi_1}{4\pi} \right) \quad (2.37)$$

$$\hat{L}_1 = \frac{N_1}{2}\lambda + \hat{\ell}_1 = (\lambda + \Delta\lambda) \left(\frac{N_1}{2} + \frac{\varphi_1}{4\pi} \right) \quad (2.38)$$

where N_0, N_1 are equal integers as long as $\ell < \lambda/2$ and $\Delta\lambda$ is a generic drift in wavelength between the two measurements, caused by a variation of either

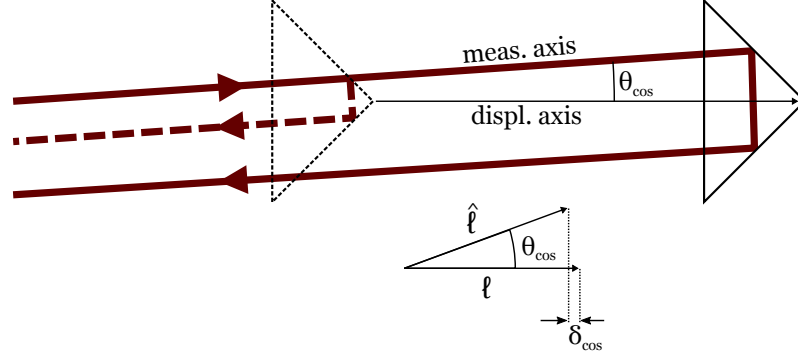


Figure 2.7: Schematic representation of the cosine error.

the source vacuum wavelength or the medium refractive index n (see below) or both. The deadpath error δ_{dp} results from the following:

$$\begin{aligned}
 \widehat{\ell}_1 - \ell_1 &= \widehat{L}_1 - L_1 = \Delta\lambda \left(\frac{N_1}{2} + \frac{\varphi_1}{4\pi} \right) \\
 &= \Delta\lambda \left(\frac{N_0}{2} + \frac{\varphi_0}{4\pi} \right) + \frac{\Delta\lambda}{4\pi} \varphi \\
 &= \frac{\Delta\lambda}{\lambda} L_0 + \frac{\Delta\lambda}{\lambda} \ell
 \end{aligned} \tag{2.39}$$

The first term on the right of the above equation is the additional deadpath error, while the second term represents the standard length error associated to wavelength variations. The uncertainty resulting from the deadpath error is

$$\epsilon_{\ell,dp} = \sqrt{\left(L_0 \epsilon_{\frac{\Delta\lambda}{\lambda}} \right)^2 + \left(\frac{\Delta\lambda}{\lambda} \epsilon_{L_0} \right)^2}. \tag{2.40}$$

where ϵ_{L_0} and $\epsilon_{\Delta\lambda/\lambda}$ are the uncertainties respectively on the deadpath length and on the fractional wavelength change. Therefore any path length imbalance increases the system sensitivity to changes both in λ_0 and n , because they apply also to the deadpath rather than just to the displacement pathlength.

2.4.3 Environmental

Finally, the third category of error sources is that of environmental errors, which refer to all those optical path length variations not caused by real changes in the measured geometrical distance, that is when the fiducial points are stationary. Temperature fluctuations and gradients may be critical for optics with high CTE [122]. Similarly, heat flow from active parts such as AOMs and lasers can cause mechanical parts to stress and relax and, thus, to fluctuate the optical beam direction and alter the pathlength. Moreover, under atmospheric conditions any change in temperature T , pressure p , relative humidity H or carbon dioxide content x_{CO_2} will cause a variation in the refractive index of air n and then in the detected displacement. In fact, the source wavelength in air $\lambda = \lambda_0/n$ determines the basic length reference for the displacement measurement, as described by Eq. 2.13. From that equation we obtain

$$\epsilon_{\ell,n} = \frac{\epsilon_n}{n} \ell \tag{2.41}$$

where the uncertainty ϵ_n on the air refractive index can be determined by direct tracking of the index changes (e.g. with refractometry) or inferred indirectly by separate measurements of the ambient quantities. For the latter method to be applied, one must measure the most critical environmental parameters and propagate the associated uncertainties ($\epsilon_T, \epsilon_p, \epsilon_H, \epsilon_{\text{CO}_2}$) using Ciddor's empirical equation [123] or Edlén's equation, in its original [124] or revised version [125, 126]. More in detail, in Bonsch et al. [126] they start from the Edlén's formula with the aim of providing the highest possible accuracy for laboratory conditions. Thus they consider only a small temperature range about 20°C and a CO₂ mixing ratio near 400 ppm, where linear formulae are adequate. The calculation starts with the dispersion formula of dry air for the standard conditions $T_{std} = 20^\circ\text{C}$, $p_{std} = 10^5 \text{ Pa}$, $x_{\text{CO}_2, std} = 0.04\%$, describing the refractivity of standard air dependent on the wavelength λ :

$$(n - 1)_{std} \cdot 10^{-8} = 8091.37 + \frac{2333983}{130 - \frac{1}{\lambda(\mu\text{m})^2}} + \frac{15518}{38.9 - \frac{1}{\lambda(\mu\text{m})^2}}. \quad (2.42)$$

Then the CO₂, T and p contributions are added:

$$(n - 1)_{x_{\text{CO}_2}} = (n - 1)_{std} \cdot [1 + 0.5327 (x_{\text{CO}_2} - 0.0004)] \quad (2.43)$$

$$(n - 1)_{T,p} = \frac{(n - 1)_{x_{\text{CO}_2}} \cdot p(\text{Pa})}{93214.60} \cdot \frac{1 + 10^{-8} (0.5953 - 0.009876 \cdot T(^{\circ}\text{C})) \cdot p(\text{Pa})}{1 + 0.0036610 \cdot T(^{\circ}\text{C})}. \quad (2.44)$$

Finally, the influence of water vapour with partial pressure p_w is calculated:

$$n = 1 + (n - 1)_{T,p} - p_w(\text{Pa}) \left[3.8020 - 0.0384 \frac{1}{\lambda(\mu\text{m})^2} \right] \cdot 10^{-10}, \quad (2.45)$$

where the partial pressure p_w can be inferred from the relative humidity parameter H by calculating the water vapour saturation pressure p_{ws} ; this can be done using the density equation 2.5 reported in [127], which reads:

$$\ln \left(\frac{p_{ws}}{p_c} \right) = \frac{T_c}{T} (a_1 \theta + a_2 \theta^{1.5} + a_3 \theta^3 + a_4 \theta^{3.5} + a_5 \theta^4 + a_6 \theta^{7.5}), \quad (2.46)$$

where $\theta = 1 - T/T_c$ and the various other parameters are empirical constants defined as follows:

$$\begin{aligned} T_c &= 647.096 \text{ K}, \\ p_c &= 22064000 \text{ Pa}, \\ a_1 &= -7.85951783, \\ a_2 &= 1.84408259, \\ a_3 &= -11.7866497, \\ a_4 &= 22.6807411, \\ a_5 &= -15.9618719, \\ a_6 &= 1.80122502. \end{aligned}$$

The usage of equations 2.42 through 2.46 lets us evaluate the air refractive index with an inherent uncertainty of about 10^{-8} . Nevertheless, this lower

bound can hardly be reached because of the low degree of accuracy with which the ambient parameters are usually measured.

Together with ambient parameters variation, air turbulence is usually another main cause of refractive index fluctuation. This effect can be fairly reduced by putting the whole gauge into an enclosure or by placing the critical beam paths inside protective tubes [128].

2.5 ERROR MODEL

Starting from all the above described error sources, the law of propagation of uncertainty is used in order to obtain a complete error model for the displacement gauge. The real displacement $\ell = f(x_1, \dots, x_k, \dots, x_n)$ is a function of many different parameters, each affected by an individual uncertainty ϵ_{x_j} . All individual error terms combine in quadrature to give the combined uncertainty ϵ_ℓ associated with the measured value $\widehat{\ell}$, as follows:

$$\epsilon_\ell^2 = \sum_{k=1}^n \epsilon_{\ell, x_k}^2 = \sum_{k=1}^n \left(\frac{\partial f}{\partial x_k} \cdot \epsilon_{x_k} \right)^2, \quad (2.47)$$

which is the uncertainty propagation formula in the special case of uncorrelated error sources.

The phase-displacement relation expressed in Eq. 2.13 can be slightly changed by following the observations of section 2.4. Therefore, the resulting measurement model turns out to be

$$\widehat{\ell} = \frac{\lambda_0}{4\pi n} \varphi + \delta_{abb} + \delta_{cos} + \delta_{dp} \quad (2.48)$$

and, by applying Eq. 2.47, this can be used to infer the total uncertainty ϵ_ℓ associated to each instantaneous measurement.

3

EXPERIMENTAL SETUP

Our goal is to investigate the possibility of measuring relative distances between retro-reflective fiducials using a technique called heterodyne displacement interferometry. In this chapter we will discuss the experimental setup and the various optical and electrical components that are used in our implementation of that technique. The interferometer configuration is based on a modified Mach-Zehnder layout and a schematic overview of the complete setup is shown in [Figure 3.19](#).

As mentioned in [subsection 1.5.2](#), this interferometer is developed within the scope of the GINGER experiment, which will benefit from an external metrology truss for the stabilization of its large opto-mechanical structure.

3.1 SOURCE UNIT

For our method to work we need two relatively stable optical frequencies which must differ by an amount small enough to be detected and manipulated by standard photodiodes and electronics. As stated in [section 2.2](#), one way to obtain this is to split in half a single laser beam and insert into both of the created branches two AOMs, driven with RF signals at slightly different frequencies ([Figure 2.2a](#)). Since phase is the final quantity of interest, low phase noise from the source unit components must be guaranteed to ensure good functioning of the whole experiment. The required properties of the source laser were first investigated qualitatively, as well as their effects on the output heterodyne beat. To this end, a numerical simulation of the optical beating was performed, in order to get some feeling on how the physical phenomenon works and then to find out any critical need to be met by the source and, possibly, by the frequency shifters. To take into account the actual physical behaviour of the source, two types of random noise are added to the formulation of [Equation 2.6](#), nominally amplitude and frequency noise, as follows:

$$E_j \sim \mathcal{N}(E_{0j}, \sigma_E^2) \quad (3.1)$$

$$v_j \sim \mathcal{N}(v_{0j}, \sigma_v^2) , \quad (3.2)$$

where $\mathcal{N}(\mu, \sigma^2)$ indicates a white gaussian noise of μ mean and σ standard deviation. In the same hypotheses of [section 2.2](#), we can take the real part and simplify [Equation 2.6](#) to:

$$E_j(t) = [E_{0j} + E_{nj}(t)] \cos \{2\pi [v_{0j} + v_{nj}(t)] t + \varphi_j\} , \quad (3.3)$$

where E_{0j} and v_{0j} are the average values of amplitude and frequency respectively, while $E_{nj} \sim \mathcal{N}(0, \sigma_E^2)$ and $v_{nj} \sim \mathcal{N}(0, \sigma_v^2)$ are the time-varying parts

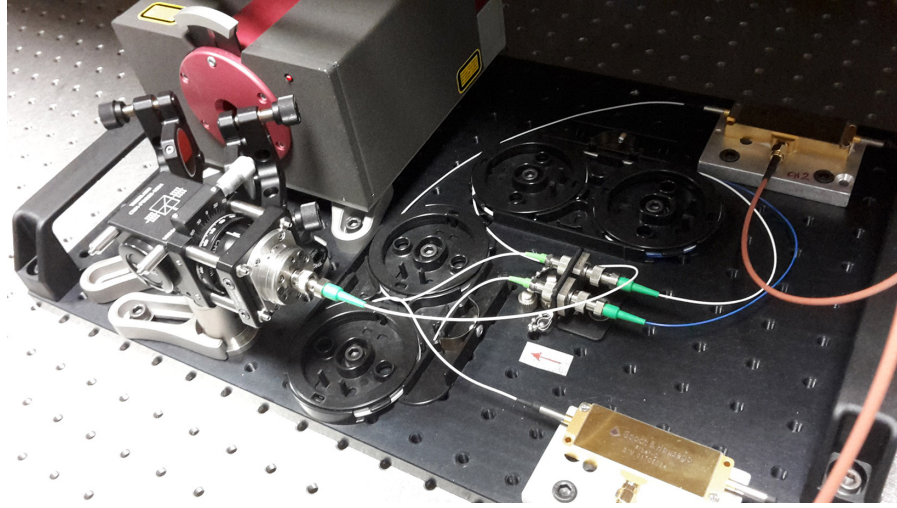


Figure 3.1: Heterodyne source unit mounted on its portable breadboard.

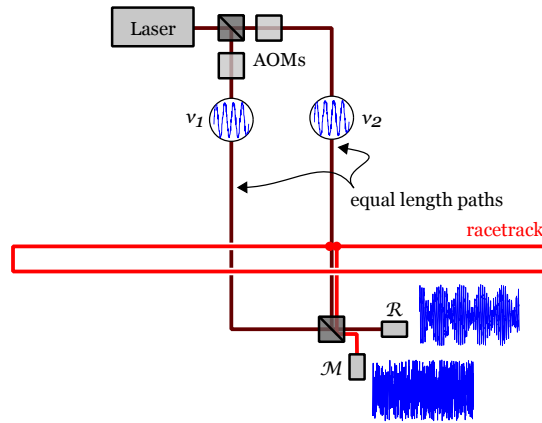


Figure 3.2: Reference interferometric configuration for the simulated optical beats. The displayed output refer to a source coherence length of 14 m which falls between the actual 4 m arms length and the sum of an arm length with the imposed racetrack length $2L = 20\text{ m}$; clearly the loss of coherence due to racetrack travelling nulls beats visibility on the \mathcal{M} detector.

that contain the amplitude and frequency noises. It should be noted that a real source emits a continuous stream of photons, indeed multiple time events, overlapping each other with a phase noise directly, but not trivially, related to the linewidth. This is due to the nature of the laser photon emission, which can be formalized as a random process. The problem here is simplified by considering a single and continuous time signal combined with additive white noise. For a further insight into the issue and a complete analytical description of lasers phase noise refer to [129]. We report here an operational definition for the linewidth $\Delta\nu$ of a laser affected by white gaussian frequency noise of variance σ_ν^2 :

$$\Delta\nu = \pi \sigma_\nu^2, \quad (3.4)$$

where the linewidth is intended as the FWHM of a Lorentzian line shape [130]. The corresponding coherence length reads

$$L_{\Delta\nu} = \frac{c}{\pi \Delta\nu} = \frac{c}{\pi^2 \sigma_\nu^2}. \quad (3.5)$$

In the numerical simulation two temporal cosine waves are built, summed and the resulting signal is analysed. Its spectrum is computed as well, for monitoring its changes due to the presence or absence of noise. Concurrently, beats visibility is evaluated in the time domain as the noise variance increases.

Within the developed script both amplitude and phase noises of E_1 and E_2 can, or cannot, be correlated to each other, which means that the same generated random vector is used for both time signals. The first condition reflects the case in which a single laser source is used, splitted into two beams by a beam-splitter and fed to identically driven AOMs. On the other hand, uncorrelated noise is given by use of two different laser sources and/or by independently driven AOMs. Another important point is the possibility of simulating the presence or absence of a long racetrack $2L$, for its effect on one of the beams and its influence on the \mathcal{M} signal. Light time-of-flight through the racetrack is computed and this value is taken in order to forward shift the time duration of just one beam. Then the two beams, now “existing” over different time intervals, are summed as usual. Moreover, an equal time delay for both signals can also be introduced to study the effects of the arms length L_{arm} on beats contrast. The above described configuration is showed in [Figure 3.2](#). Without loss of generality, the ratio f_{het}/ν used throughout the simulations was 10^{-2} instead of that of the real experiment, which settles around $3 \cdot 10^{-11}$. This was necessary in order to reduce the number of computed points and consequently the computing time.

[item 3.3a](#) shows how the $E_{tot} = E_1 + E_2$ looks like if no noise is added. Differently, in [item 3.3b](#) an exaggerated $\Delta\nu/\nu = 0.002$ was imposed to make clear the loss of coherence with increasing travelled pathlength, which results in a progressive reduction of beats contrast. The frequency noise and the phase noise can be seen as two alternative ways to describe the same phenomenon, since the instantaneous frequency is uniquely defined by the phase. More in detail, the instantaneous frequency ν can be defined as the derivative of the phase φ :

$$\nu = \frac{1}{2\pi} \frac{\partial \varphi}{\partial t}. \quad (3.6)$$

In other words, instantaneous phase results from integrating ν_j over time. Integration of white noise results in generation of red noise (random walk), which shows a frequency distribution with $1/f^2$ dependence [[131](#)]. Indeed, this intuitively explains why coherence is lost gradually with elapsing time (lowering frequencies).

Further simulations were conducted with different values of $\Delta\nu$. What is observed is that fully correlated phase noise never compromises beats visibility, meaning that a useful signal can always be detected by the \mathcal{R} photodiode, regardless of the finite and possibly large linewidth ([item 3.3c](#)). On the other hand, fully uncorrelated phase noises worsen beats visibility only for observation times longer than the source coherence time; thus an heterodyne signal can still be observed with uncorrelated phase noises, i.e. with independent lasers or independently driven AOMs, as long as the common path is shorter than the coherence length of the splitted beams ([item 3.3e](#)). The main issue of having uncorrelated noise on the beams is that beats visibility becomes dependent on the absolute length L_{arm} of the interferometer arms, therefore both \mathcal{R} and \mathcal{M} beats can worsen with short coherence lengths ([item 3.3d](#)). Similarly, in presence of the racetrack, as long as this racetrack is longer or comparable with the source coherence length, beats disappear on the \mathcal{M} detector ([item 3.3f](#)); introducing a racetrack, that is a time delay, is actually equivalent to uncorrelate E_{n1} from E_{n2} . Assuming the worst case of uncorre-

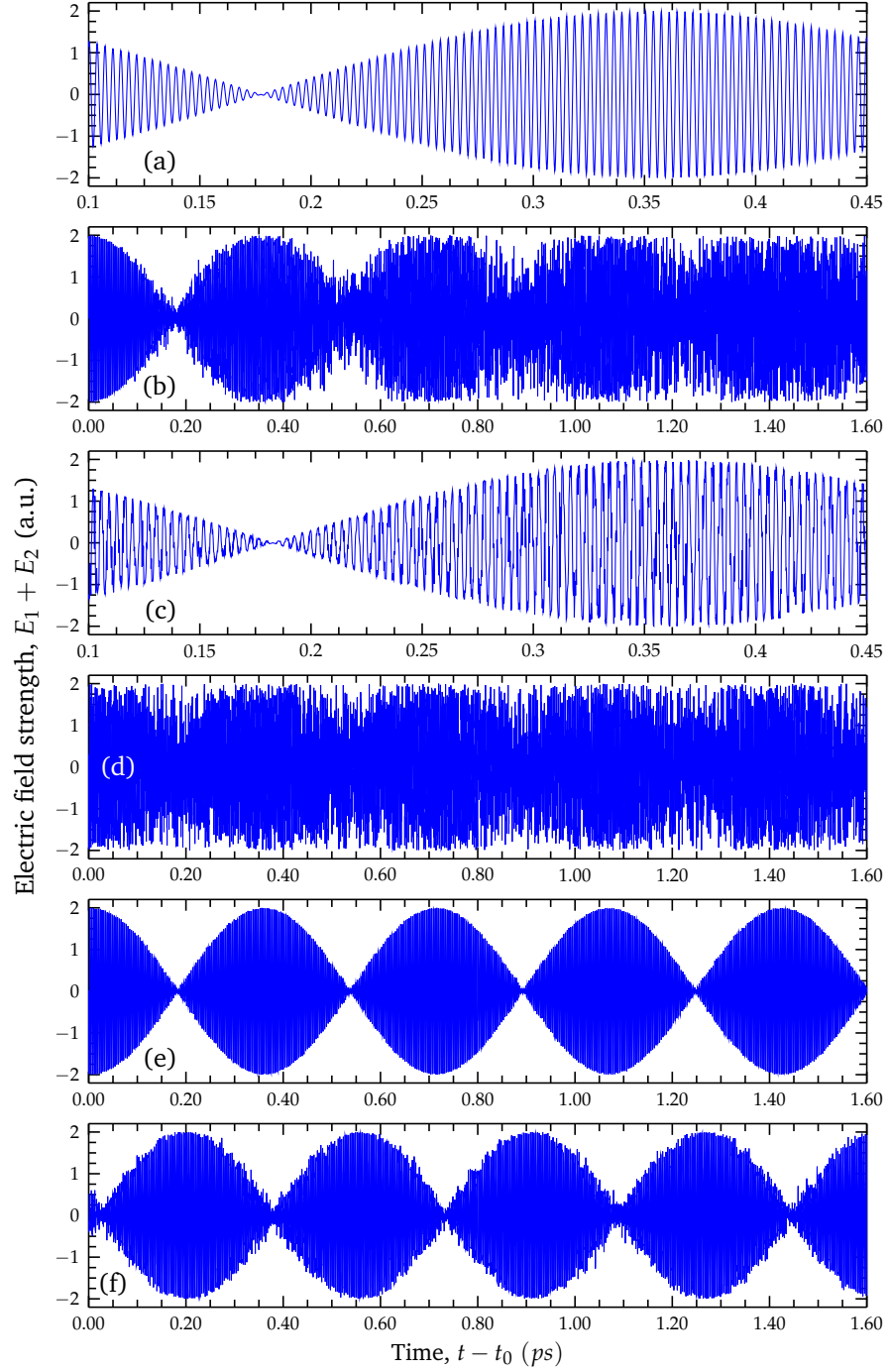


Figure 3.3: Simulated optical beating with $\lambda = 1064 \text{ nm}$ and $f_{\text{het}}/\nu = 0.01$. The output at \mathcal{R} or \mathcal{M} detector are showed for different optical path configurations and source linewidth values:

- (a) $\Delta\nu = 0$ (ideal signal), on \mathcal{R} detector;
- (b) uncorrelated $\Delta\nu/\nu = 0.002$, on \mathcal{R} detector;
- (c) correlated $\Delta\nu/\nu = 0.2 \rightarrow L_{\Delta\nu} = 0.17 \text{ mm}$, $L_{\text{arm}} = 4 \text{ m}$, on \mathcal{R} detector;
- (d) uncorrelated $\Delta\nu = 50 \text{ MHz} \rightarrow L_{\Delta\nu} = 1.9 \text{ m}$, $L_{\text{arm}} = 4 \text{ m}$, on \mathcal{R} detector;
- (e) uncorrelated $\Delta\nu = 1 \text{ MHz} \rightarrow L_{\Delta\nu} = 95 \text{ m}$, $L_{\text{arm}} = 4 \text{ m}$, on \mathcal{R} detector;
- (f) uncorrelated $\Delta\nu = 1 \text{ MHz} \rightarrow L_{\Delta\nu} = 95 \text{ m}$, $L_{\text{arm}} = 4 \text{ m}$, $2L = 20 \text{ m}$, on \mathcal{M} detector.

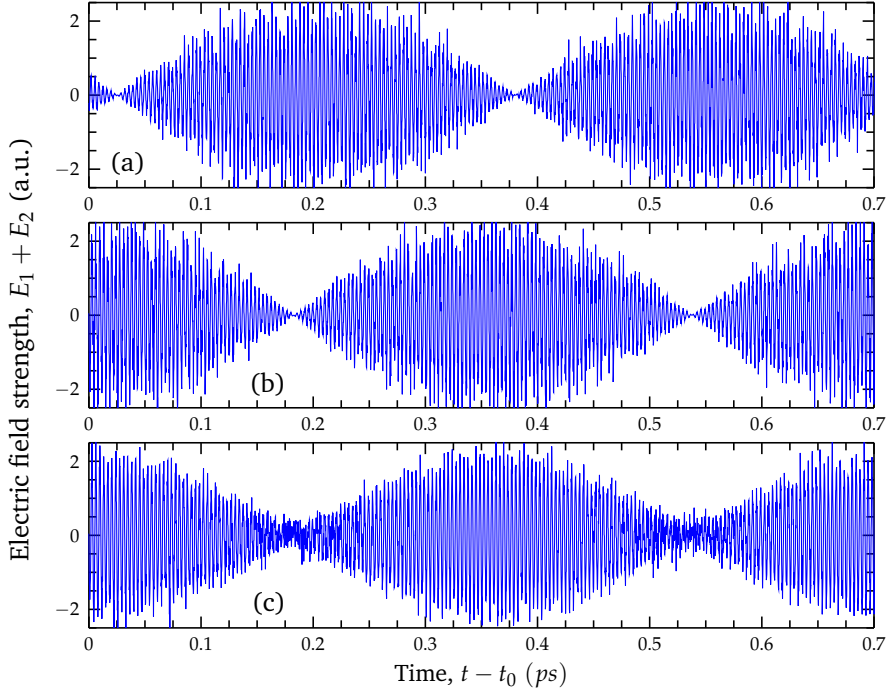


Figure 3.4: Simulated optical beating with $\lambda = 1064\text{ nm}$ and $f_{het}/\nu = 0.01$. The output at \mathcal{R} or \mathcal{M} detector are showed for different optical path configurations in presence of amplitude noise:

- (a) correlated $\sigma_E = 0.1$, $L_{arm} = 4\text{ m}$, $2L = 20\text{ m}$, on \mathcal{M} detector;
- (b) correlated $\sigma_E = 0.1$, $L_{arm} = 4\text{ m}$, on \mathcal{R} detector;
- (c) uncorrelated $\sigma_E = 0.1$, $L_{arm} = 4\text{ m}$, on \mathcal{R} detector.

lated frequency noise after power splitting, from Equation 3.5 we can retrieve the condition for good beats contrast as a function of the laser linewidth:

$$L_{\Delta\nu} = \frac{c}{\pi \Delta\nu} \gg L_{arm} + 2L$$

$$\Delta\nu \ll \frac{c}{\pi (L_{arm} + 2L)} . \quad (3.7)$$

The maximum racetrack length $2L$ is determined by the maximum size of a the ring-lasers within the GINGER array. The foreseen side length can measure up to $L = 10\text{ m}$. Whereas a reasonable value for L_{arm} may be of about 20 m if we consider a metrology system based on a single laser source. The light from this source requires proper splitting and handling through fibers in order to reach all the displacement gauges, which are themselves attached to all the critical distances requiring stabilization. Differently, the current experimental setup has $L_{arm} \approx 4\text{ m}$. The free-space racetrack length extends now for 2 m and will be incremented in the future to 7 m with folding mirrors, to simulate more closely the operative conditions of GINGER. With the given values for L_{arm} and $2L$, Equation 3.7 gives

$$\Delta\nu \ll 2.4\text{ MHz} . \quad (3.8)$$

Similar simulations to that of frequency noise were performed with additive amplitude noise. What becomes clear is that correlated amplitude noise never weakens beats visibility, regardless of the presence of the racetrack

(item 3.4a,item 3.4b). Instead, uncorrelated amplitude noises always have a detrimental effect on beating contrast, which decreases linearly with the amplitude noise variance (item 3.4c). These results, being based on a simplification of the real physical phenomenon, do not consider at all any effects of coupling between intensity and phase noise, which are instead treated separately.

3.1.1 Laser source

Thanks to the above reported observations and those in subsection 1.5.2, constraints in terms of spectral bandwidth and output power were determined for the ideal laser source.

The emission wavelength does not represent a metrological constraint as long as the choice is limited in the range of visible and NIR radiation. Infrared is somewhat preferred because it is also the spectral region of choice for telecommunications. This means better performances at lower costs due to the widespread use of that type of technology, with particular focus on optical fibers. IR fibers are inexpensive and offer very low transmission losses if compared to those designed for the visible range [132].

A wide range of available commercial sources was considered for use in this experiment. Quite different technologies can be found off-the-shelf, each capable of single frequency operation and narrow linewidth. Stabilized He-Ne lasers offer great short and long term stability, thanks to thermally driven cavity length control; unfortunately, low output power, usually below 5 mW , can be reached with this technology. Laser diodes with integrated semiconductor gratings or external cleaning cavities, namely DFB, DBR, VHG and ECDL lasers, have good spectral purity and high output power, but lack in terms of beam spatial quality and suffer from flicker noise and worse spectral stability [133, 134]. Continuous-wave (cw) Ti:sapphire sources, commonly used in coherent optical communications, offer the best performances at the highest price. This type of laser relies on a crystal of sapphire (Al_2O_3) that is doped with titanium ions. Ti:sapphire sources operate most efficiently at wavelengths near 800 nm and usually require to be pumped by another laser in the green spectral region. Diode pumped solid state (DPSS) lasers are the optimal union of the efficiency of laser diodes (the pump) with the excellent spatial and spectral emission quality of crystals [135]. Commercial devices integrate geometrical and thermal controls of the cavity to provide linewidths below the MHz and excellent beam characteristics.

The light source used for our experiment is a cw DPSS laser based on a Nd:YAG crystal in non-planar ring oscillator configuration, working at $\lambda_0 = 1064\text{ nm}$ (Mephisto, Innolight GmbH, Germany). This source can output up to 500 mW of power in single-frequency operation and can be thermally tuned over a 30 GHz range. Directly after the laser, a few optical components prepare the beam for use in the rest of the setup. A combination of a polarizing beam-splitter (PBS) and a half-wave plate (HWP) converts the elliptical polarization of the source into a linear one and permit fine alignment to the slow axis of a single-mode (SM) polarization-maintaining (PM) optical fiber. Figure 3.5 displays the source light spectra near DC, which show a flat noise floor around f_{het} and a broad spurious peak at about 100 kHz . We found that closing the embedded amplitude-stabilization loop (noise-eater) of our laser slightly shifted the amplitude noise peak. These unwanted peak is likely to cause aliasing artifacts at the acquisition stage in the case of low sampling rates and absence of proper filtering; the issue is discussed later on in Sec 3.3.1.

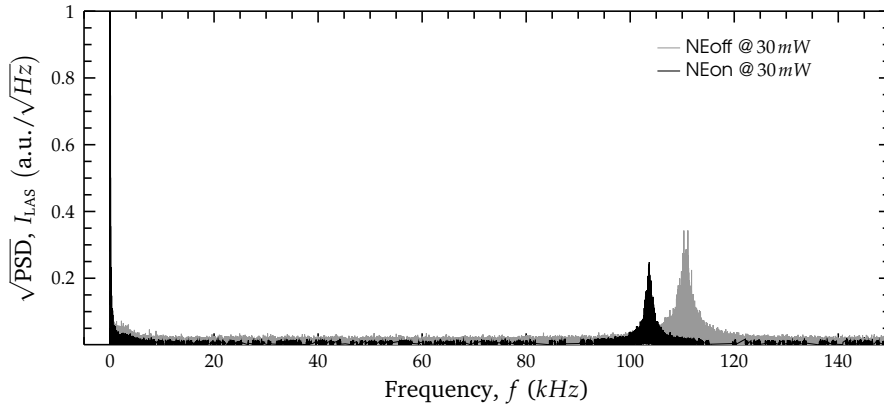


Figure 3.5: Source light spectrum near DC: the laser source presents a spurious amplitude modulation at a frequency of about 100kHz . The peak location and magnitude depend on the output power and on the operation of the noise eater embedded into the laser unit.

3.1.2 Fibers

Throughout the setup a number of optical fibers is used, mainly because of their convenience in transporting light between different parts of the optical setup. In this way an optical layout can be made modular, which, for example, allows exchanging or moving the laser source without having to realign sub-systems further down the optical path. Another useful property of (single-mode) fibers is that they act as spatial filters. This is especially important in interferometry, where well defined beam profiles are needed to achieve high fringe contrast when overlapping two beams. Fiber coupling of the source is achieved by a couple of folding mirrors and an aspheric lens mounted on a stable 5 degrees-of-freedom (dof) micropositioner (FiberPort PAF-X-5-C, Thorlabs Inc., USA). This means of lens alignment, combined with the excellent spatial quality of the laser ($M^2 < 1.1$), makes possible to achieve $> 85\%$ SM coupling efficiency with low efforts. The combination of elements results as well very stable in time and does not require user adjustments for months.

The coupled light is sent to a 50:50 fiber splitter (PMC1060-50B-APC, Thorlabs Inc., USA), where the two branches of the interferometer are created.

3.1.3 Acousto-optic modulators

Two in-fiber TeO_2 AOMs (Fiber-Q T-M150-0.4C2G-3-F2P, Gooch & Housego PLC, UK) are driven by the same RF synthesizer (ARF421, MOG Laboratories Pty Ltd, Australia) and fed, via shielded coaxial cables, with slightly frequency shifted signals near 150MHz , in order to obtain two laser beams with a fixed frequency offset $f_{\text{het}} = 10\text{kHz}$. f_{het} was chosen as a tradeoff between the electronics limited detection bandwidth and the maximum detectable displacement speed.

The selected offset frequency is both high enough for fast displacement monitoring and sufficiently low for easy, and cheap, detection with off-the-shelf electronics. With this in mind, one would choose the heterodyne frequency almost arbitrarily within the kHz range. Nevertheless there are some issues worthy of mention. Placing f_{het} at a frequency where the laser amplitude fluctuations are at the shot-noise limit may be helpful; unfortunately, this

was not possible because of the limited 50kHz bandwidth of the acquisition system in use for demodulation. There may exist, however, sources of technical noise at frequencies that can easily be avoided. We have found noise peaks due to both our detectors and laser (see subsection 3.3.1). Thus it is always wise to look at the amplitude noise spectra of the detector and laser to avoid accidentally choosing a noisy zone. The chosen $f_{\text{het}} = 10\text{kHz}$ falls in a fairly quiet frequency zone, as can be seen in Figure 3.17.

The signals sent to the modulators are phase locked to the same 1GHz internal clock to avoid additional uncorrelated phase noise on the channels. As already stated, independent AOMs driving on the two channels adds uncorrelated frequency noise that can be associated to an equivalent shortened coherence length. The RF driver used guarantees channels crosstalk $< -90\text{dBc}$, harmonic distortion at -80dBc and phase noise of -114dBc/Hz @ 10kHz . These excellent performances exclude the device from contributing in a notable manner to the total displacement noise at the interferometer output. AOMs non-ideal behaviour is more likely to limit the instrument sensitivity. Both AOMs come with integrated PM fiber coupling and 3m output fibers. This provides optimal mode cleaning and gives the possibility of keeping the sensible section of the setup away from the heat dissipated by the laser and the AOMs. To this end, the laser source, the AOMs and the coupling unit are all mounted on a portable breadboard (see Fig. 3.1). The choice of fiber coupled AOMs against free-space ones demonstrated to be successful. These AOMs does not need any alignment procedures nor adjustments while the driving frequency is changed. Their efficiency settles above 60% as far as the driving frequency is maintained in the $145 - 155\text{MHz}$. This means that f_{het} can be easily tuned between 0Hz and 10MHz with a tolerable power efficiency of the overall system.

3.2 MEASUREMENT INTERFEROMETER

After exiting from the modulator fibers, the light of both arms passes through refractive collimators to provide well collimated beams at the way in of the free-space section of the interferometer. These source beams have a $1/e^2$ diameter $D_{\text{beam}} = 8\text{mm}$ and recombine at a 50:50 non-polarizing beam-splitter to give a single-fringe interference pattern. Alignment procedures at a first stage are conducted by setting $f_{\text{het}} = 0$. As showed in Figure 3.6a, the interferometer in the beginning of the alignment procedure looks and works like a standard Mach-Zehnder interferometer. Cage-system compatibility has been also guaranteed, to ease optics positioning and to allow fast starting alignment of the layout.

As stated in subsection 2.4.2, realizing the cancelable circuit by polarization coding has some inherent limitations which may lead, possibly in a more advanced development status of the experiment, to unwanted non-linear errors which cannot be eliminated without a full gauge redesign. Wavefront division represents a trickier solution, but it overcomes such limitations and makes the optical crosstalk less complex to manage, thanks to the insertion of properly designed masks. The proper shapes and sizes of the wavefront splitting optics can be determined by studying how the laser beam propagates inside the interferometer. In particular, one must take care of the beams cross sections, from the wavefront division point until right before the merging point, as well as all along the beams common path to the detectors. Diffraction at

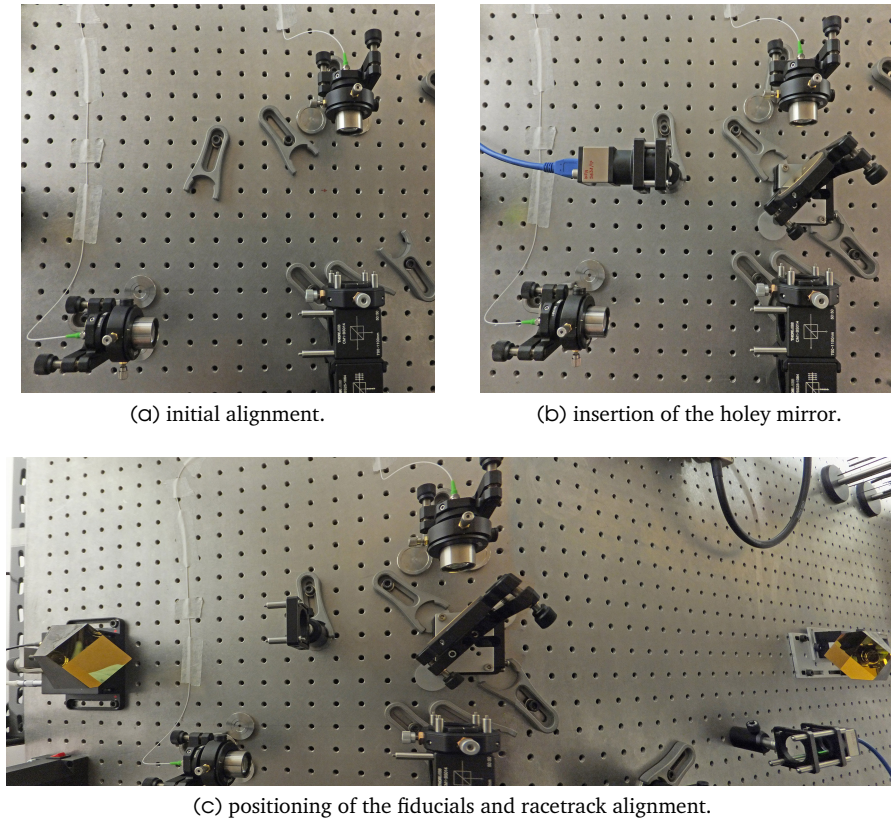


Figure 3.6: Pictures of some critical steps in the alignment of the displacement interferometer. One of the two alignment cameras (UI-3370CP-NIR-GL, IDS GmbH, Germany) can be seen in picture (b).

every aperture alters the propagation of light and can cause one beam to mix with its counterpart.

3.2.1 Holey mirror

The developed instrument implements the cancelable circuit design described in subsection 2.2.1. The separation of \mathcal{R} and \mathcal{M} is obtained by wavefront division. In addition, the gauge is designed for being placed in between the two fiducial points, as discussed in Sec. 1.5.2. This is made possible by the creation of a *racetrack* which the measurement beam \mathcal{M} must follow before recombining at the 50:50 BS. A double-coated gold mirror with a central hole of diameter $D_{hol} = 4\text{mm}$ (custom item in Fig. 3.8a, Tecnottica Consonni Srl, Italy) spatially splits one of the source beams in two parts: the inner part, \mathcal{R} , which propagates straight through the hole towards the recombination point, and the outer part, \mathcal{M} , with a ring shaped cross-section, which instead hits the mirror and travels towards the first fiducial (on the left of Fig. 3.19). This beam measures the distance between the fiducials by closing a loop: the beam goes to the first fiducial retro-reflector and hits it off-center; the reflected beam is then offset and goes past the gauge to hit the second fiducial on the right; then the beam is offset again to the opposite way and lines up with the center of the drilled mirror back surface; finally \mathcal{M} hits the back side of the mirror (*merging point*) and proceeds towards the recombination BS.

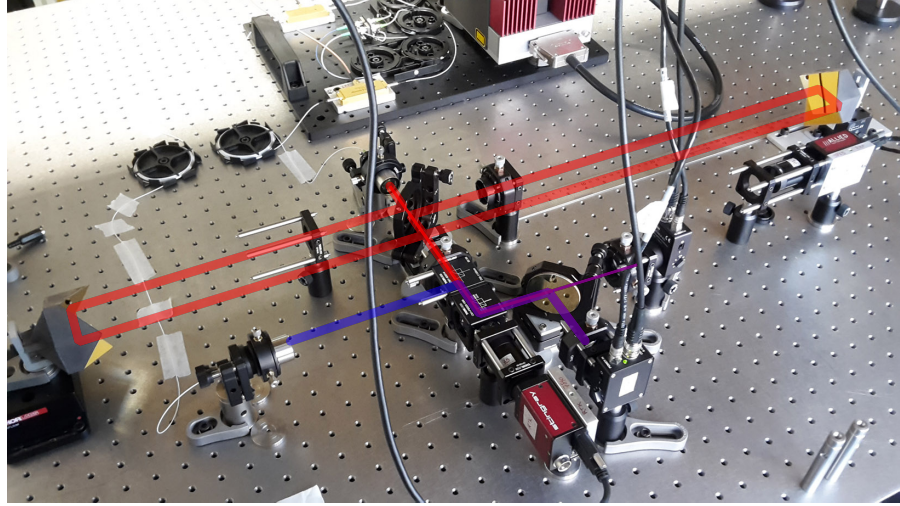


Figure 3.7: Displacement gauge under test. The beam paths of arm1 and arm2 are indicated in purple and red respectively.

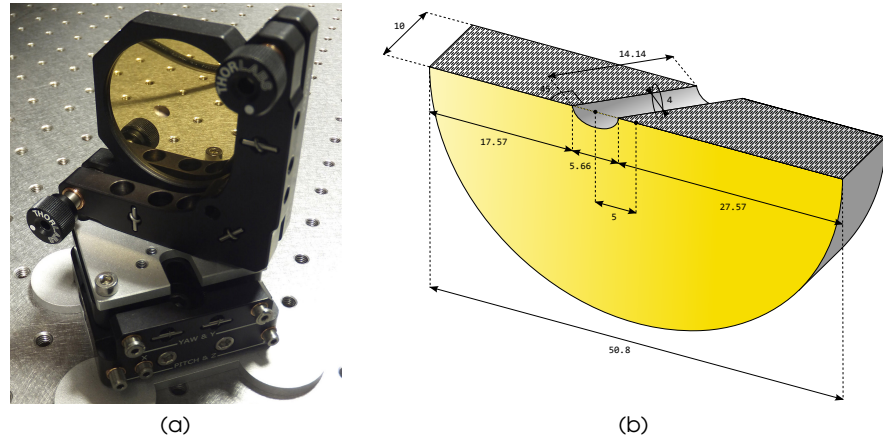


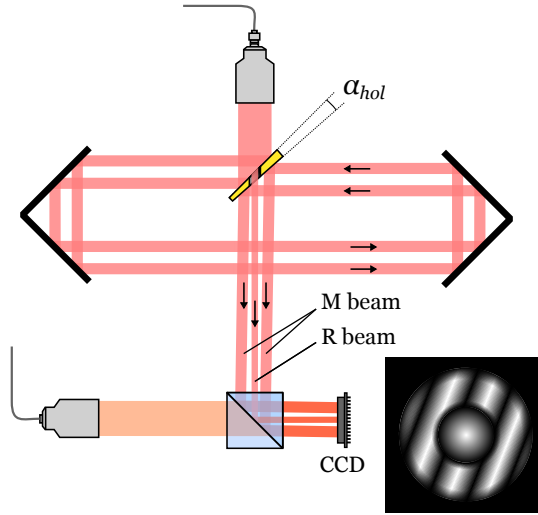
Figure 3.8: Wavefront division mirror with central tilted hole and front-back coating: (a) picture of the holey mirror mounted on a 6 dof kinematic manual stage and (b) custom design provided to the manufacturer (all critical dimensions are reported).

The custom design of the drilled mirror reported in [Figure 3.8b](#) highlighted non-trivial footprint issues, given that it had to work at a 45° angle of incidence while keeping a wide enough clear aperture on both of its sides. A 2 in diameter was chosen in order to avoid any beam blocking by standard mounts. The central hole must be wide enough to minimize diffraction effects; clearly, a larger hole binds to the necessity of magnifying the beams and thus to use additional larger optics. The actual hole diameter was selected in order to equally distribute the incoming optical power between the \mathcal{R} and the \mathcal{M} beams. Supposing a gaussian intensity distribution across the beam profile, we can write in (r, θ) polar coordinates

$$I(r, \theta) = \exp(-r^2) r \quad (3.9)$$

$$P|_{r_i}^{r_o} = \int_{A_{r_i r_o}} I = \int_0^{2\pi} \int_{r_i}^{r_o} I(r, \theta) dr d\theta, \quad (3.10)$$

Figure 3.9: Simplified layout illustrating the surface parallelism issue: \mathcal{M} beam tilting is caused by the addition of the racetrack. \mathcal{R} instead is in single fringe condition.



where $P|_{r_i}^{r_o}$ is the optical power enclosed in the ring-shaped beam cross-section of area $A_{r_i r_o}$. The optimal hole radius r_{opt} can be found by numerically solving the following equation:

$$P|_0^{r_{opt}} = P|_{r_{opt}}^{\sqrt{2}}, \quad (3.11)$$

where the left side defines the power enclosed in a circle of radius r_{opt} , while the right side accounts for the power associated to the complementary external ring. The $\sqrt{2}$ upper limit of the right integral defines the $1/e^2$ level of the normalized intensity $I(r, \theta)$. From Equation 3.11 we obtain $r_{opt}/\sqrt{2} = 0.532$, which gives an optimal hole diameter of

$$D_{opt} = D_{beam} \cdot \frac{r_{opt}}{\sqrt{2}} = 4.256 \text{ mm} . \quad (3.12)$$

The mirror coating to be applied on the front and back surfaces is bare gold. The material was selected as a tradeoff between cost and reflectivity. However, this type of coating is quite fragile and cannot be easily cleaned. Our wide aperture mirrors started showing some signs of delamination after the first months of use. Fortunately, both reflectivity and surface flatness were not much compromised by this process. A dielectric narrowband coating should be considered for future implementations, as it is more rugged and provides a higher reflectivity. The surface flatness is $\lambda/10$, as measured by the manufacturer after coating deposition. However, anything below $\lambda/5$ should not be of any concern, because the measurement is performed as an average over the full beam area. As long as the beam location is kept stable on the fiducials, no surface figure effects should arise.

One mirror property which was neglected at first is *surface parallelism*. The front and back surfaces of a mirror substrate are never perfectly flat. A real substrate is a wedge with its opposite flat surfaces defining a very low, but non-zero, angle α_{hol} . For our holey mirror the manufacturer could guarantee $\alpha_{hol} \leq 0.4 \text{ mrad}$. When inserted along arm 2 to create the racetrack path, the holey mirror is hit twice by the \mathcal{M} beam. The measurement beam hits as well two retro-reflective fiducials before merging again with its reference counterpart. If the back-reflection angle at the fiducials is not exact 180° , an additional α_{cc} error gets added to the beam pointing direction. This \mathcal{M} beam will then suffer from a total pointing error equivalent to $\alpha_{tot} = \alpha_{hol} + 2\alpha_{cc}$ with

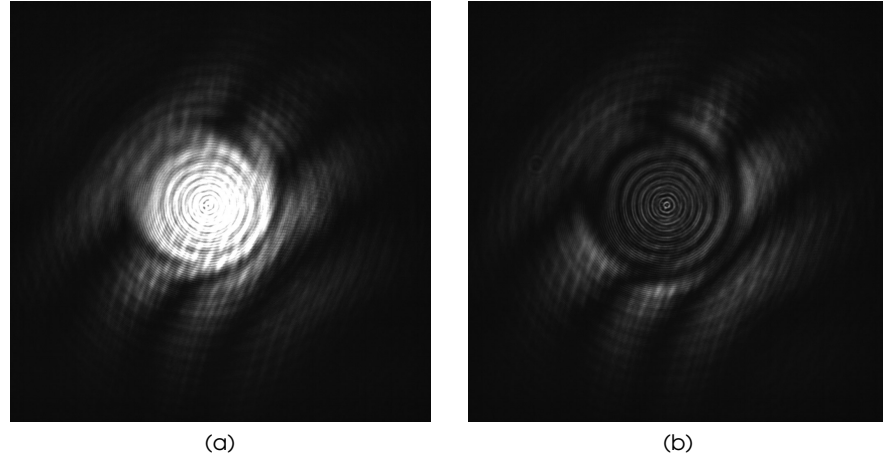


Figure 3.10: Picture of the beams cross-sections after recombination: (a) central fringe bright condition and (b) central fringe dark condition. The wedge interference pattern can be clearly distinguished across the outer ring zone (images side is 10 mm).

respect to the \mathcal{R} beam, which instead skips the racetrack optics. The issue is illustrated in Figure 3.9. What can be observed is that, at the recombination point, the single fringe condition cannot be reached any more by \mathcal{R} and \mathcal{M} at the same time. The typical wedge interference pattern can be observed in Figure 3.10 for the \mathcal{M} beam at recombination. Experimentally, we could count up to 4 fringes over an 8 mm cross-section, which gives a rough estimate of

$$\frac{4\lambda}{8\text{ mm}} \approx 0.5\text{ mrad}$$

for the total pointing error. The fiducials contribution to this sum was $2 \cdot 10\text{ arcsec} \approx 0.1\text{ mrad}$, as reported by the producer datasheet. A slight tilt of the beam in arm 1 can help in distributing the tilt fringes equally between the measurement and reference interference patterns. Nevertheless, a consistent contrast loss is observed. We addressed the problem in a pragmatic way and replaced one of the fiducials with a couple of tip-tilt mirror assemblies. This expedient added 4 dof to the racetrack path and allowed us to correct for the pointing error. The final measurement channel contrast C_M rose from 0.12 to almost 0.5.

It is clear that the above solution cannot be considered in more advanced versions of the gauge. The mirror parallelism issue must be eliminated during the manufacturing process by properly reducing tolerances. To ensure single fringe interference we impose

$$\alpha_{tot} < \frac{\lambda/2}{D_{beam}}, \quad (3.13)$$

which gives a maximum tolerable parallelism error of $62.5\ \mu\text{rad}$ for the current configuration.

3.2.2 Diffraction masks

As already mentioned in subsection 2.4.2, optical mixing of \mathcal{R} and \mathcal{M} beams is one main factor in the origin of the so called “cyclic error”, a systematic error

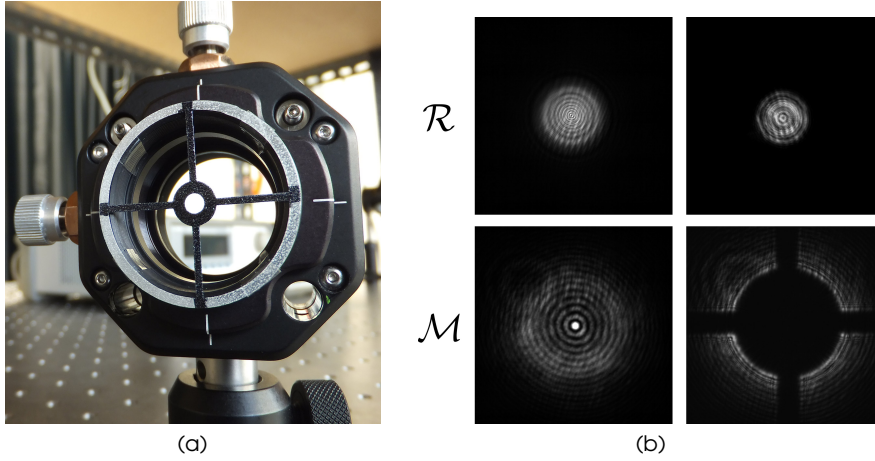


Figure 3.11: Pictures of (a) the custom ring mask mounted on a x-y kinematic manual stage and (b) the beam cross-sections before and after masks insertion, showing a good reduction of the unwanted diffraction patterns.

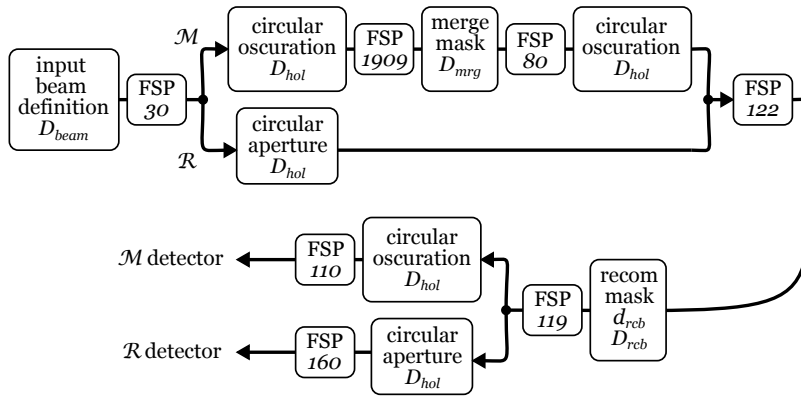


Figure 3.12: Displacement gauge POP model: free space propagation (FSP) distances are in mm .

which shows as a periodic offset between the detected displacement and the real one. Optical crosstalk mainly occurs between the merging point and the recombination point (see Figure 3.19) and is caused both by diffraction at the holey mirror aperture and by the long beam propagation over the racetrack path. In order to reduce this kind of contamination, the interferometer features a pair of removable blocking masks: a circular obscuration of diameter $D_{mrg} = 6\text{ mm}$ is located about 80 mm before the merging point; a ring obscuration of inner diameter $d_{rcb} = 3\text{ mm}$ and outer diameter $D_{rcb} = 7\text{ mm}$ is placed right before the recombination point. The masks were realized from a 0.2 mm thick steel foil, engraved with a laser cutting system formed by a femtosecond laser source and a pair of software controlled galvanometric mirrors. The masks are designed to be glued in front of a standard 1 in lens tube and feature 4 orthogonal brackets which firmly keep the obscuration at the aperture center Figure 3.11a.

The resulting optical layout was then simulated by means of the Zemax[®] Physical Optics Propagation (POP) tool [136], with the aim of predicting the amount of power leakages between the \mathcal{R} and the \mathcal{M} channels. POP uses diffraction calculations to propagate a wavefront through an optical system,

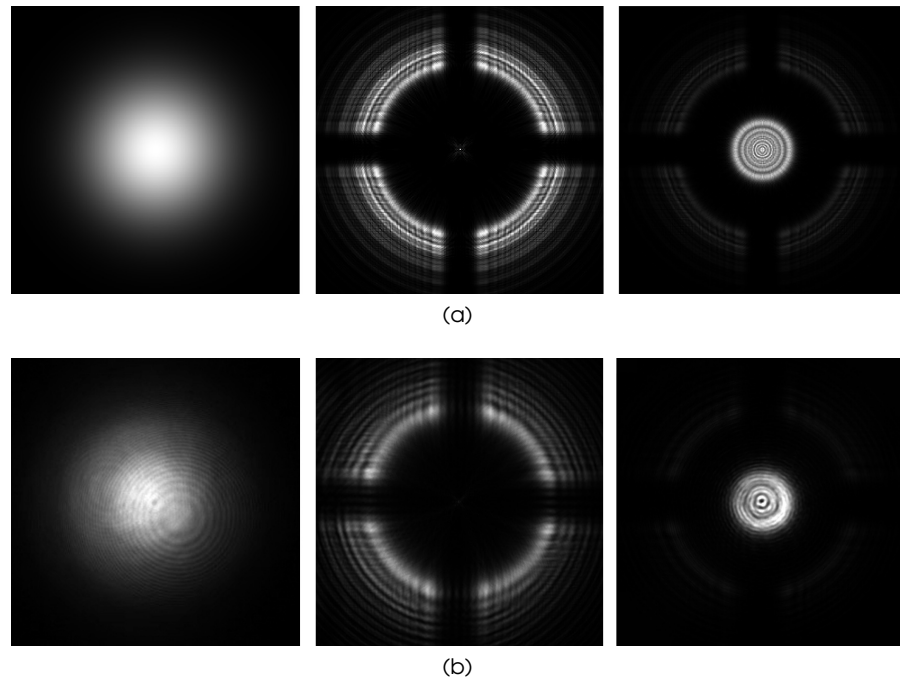


Figure 3.13: Comparison between (a) simulated beam cross-sections and (b) acquired beam cross-sections at different locations inside the interferometer. From left to right: collimated beam at exit from the fiber collimators, \mathcal{M} beam on detector (\mathcal{R} blocked), \mathcal{R} beam on detector (\mathcal{M} blocked).

surface by surface. The underlying model and algorithms work well under two main assumptions. The first is that all propagated beams are not too fast, which is easily verified in our experiment because the beams are almost collimated along the whole interferometer paths. The second assumption is that scalar diffraction applies, so the vector nature of the electric field is ignored. The POP model of our distance gauge is reported in Figure 3.12. As showed in Figure 3.13 and Figure 3.14, the simulations fit fairly well with how the real beams behave at various locations inside the interferometer. After the model was built and verified, we proceeded by calculating the power leakages of \mathcal{R} into \mathcal{M} (and viceversa) in various configurations: with and without the diffraction masks as well as for different sizes of both the holey mirror and the

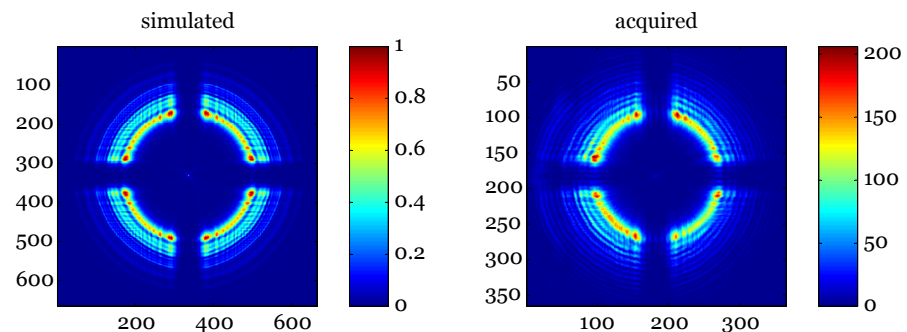


Figure 3.14: False color images of the measurement beam profile after masking and travelling to its detector. Simulated spot and acquired spot are pictured side by side, showing good consistency (intensity in arbitrary units).

Conf. (run #)	D_{hol} (mm)	D_{mrg} (mm)	d_{rcb}, D_{rcb} (mm)	ρ_{LR} ($\cdot 10^{-3}$)	ρ_{LM} ($\cdot 10^{-3}$)	$\epsilon_{\ell, cyc}$ (nm)
no mask	4	–	–, –	32.24	17.10	4.179
masks (1)	4	6	3, 7	8.694	2.037	0.9090
masks (3)	4	7	2.4, 6.2	7.451	0.361	0.6617
masks (8)	4	7.4	1.4, 7.8	1.055	0.0607	0.09451
no mask	2	–	–, –	12.38	60.58	6.180
masks (1)	2	3	1.6, 3.6	19.23	7.880	2.296
masks (3)	2	3	1.2, 3.4	18.25	2.851	1.787
masks (8)	2	2.4	1, 2.4	17.71	3.165	1.768
Modified detection layout, see subsection 3.2.4						
no mask	4	–	–, –	1.78	3.23	0.4244
masks (1)*	4	6	3, 7	0.0877	1.73	0.1540
masks (2)	4	6.78	2.50, 7.08	0.0633	0.497	0.04746
masks (3)	4	7.28	1.16, 7.58	0.0194	0.0149	0.002906

Table 3.1: Simulated optical power leakages and corresponding maximum displacement error. The (*) symbol indicates the current working configuration.

diffraction masks. A damped least-squares algorithm was used for minimizing the leakage powers by tuning the masks diameters. The optimized masks sizes were then rounded to the nearest tenth of mm to take into account possible manufacturing limits. Eventually, the maximum displacement error due to optical mixing was calculated for every configuration thanks to [Equation 2.33](#). As can be seen from [Table 3.1](#), the insertion and optimization of the diffraction masks can, in principle, improve the optical isolation between reference and measurement channels by at least one order of magnitude: for a holey mirror with a 4 mm hole diameter we obtained more than 97% reduction of the cyclic error; in the case of a 2 mm hole diameter the improvement is more limited, because of the greater diffraction effects, but still a 71% reduction is possible. The four bottom rows of the reported table refer to the simulations of a slightly changed optical model, where the apertures of the final detection stage were modified to optimize contrast. See [subsection 3.2.4](#) for further insight.

The developed optical model represents a reference point to start from for the optimization of the whole instrument. Changes in almost all the components parameters are possible, e.g. masks sizes and positions, mirror hole diameters and clear aperture, fiber collimator structure, output beam sizes, etc. Asymmetrical designs of the holey mirror and the masks are also possible in principle, although symmetry is more advisable because it naturally compensates for wavefront gradients caused by unwanted tilts in the optical elements.

We note that, although the designed masks were conceived for a rough crosstalk reduction, they turned out to be very useful as well for alignment purposes, because they made possible to align the racetrack components (the drilled mirror and the retro-reflectors) while keeping \mathcal{R} out of detectors sight.

3.2.3 Fiducials

The retro-reflectors, pictured in [Fig. 3.15](#), are of hollow corner-cube (CC) type, gold coated, and they offer a wide 63.5 mm clear aperture. Such a great diameter was selected in order to account for the 50 mm lateral offset to which

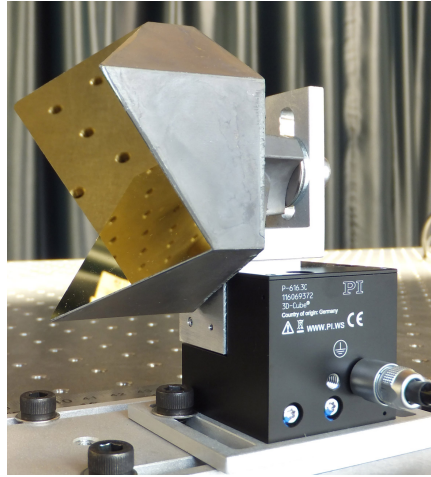


Figure 3.15: The wide aperture retro-reflector installed onto a tri-axial nanopositioner.

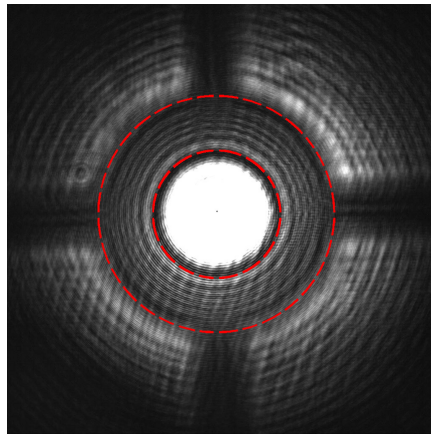


Figure 3.16: Beam cross-section of the light coming out from the final recombination BS. Non-beating light fills the ring shaped zone delimited by the mask image (dashed red lines).

\mathcal{M} is subjected while travelling along the racetrack. The issue can be better understood by looking at the traced red beams in Fig. 3.7. The fiducials are made out of a bulk aluminum substrate (50394-2510, Newport Corp., USA). Unlike those with a glass substrate, these aluminum retro-reflectors are lightweight enough to be mounted onto compact multi-directional nanopositioners (P-616.3C, Physik Instrumente (PI) GmbH & Co. KG., Germany), with negligible impairment of their dynamic performances. Each fiducial point can thus be moved programmatically along three orthogonal directions within a linear range of $100\ \mu\text{m}$ and $0.4\ \text{nm}$ resolution. We note that motion along directions other than that specified by L will not be examined here. Nevertheless, the motivation for tri-axial stages is given by the next step from the present work, which will be to reconstruct the L orientation in space from range only measurements; this is possible, in principle, by moving the fiducials along 3 orthogonal directions. This objective, as stated in section 1.4, is critical within the GINGER framework.

3.2.4 Beam combiner and detection splitter

After the recombination BS, light passes through a PBS to get rid of any non-interfering signal background. This unwanted light component may be present due to misalignments in the fiber collimator axes or because of slight changes in the polarization of \mathcal{M} after its interaction with the retro-reflective corner-

cubes. A second holey mirror causes the deflection of the measurement beam towards a detector different from the reference one.

If we observe the intensity distribution of the light coming out from the final PBS (Figure 3.16), we note the presence of a median annular region which does not recombine. This in fact is a spatial region in which the light from arm 2 is not present, thanks to the insertion of the blocking masks. Instead, the arm 1 light can freely propagate over its full initial area and is not prevented from filling this zone. When this non-beating light reaches the detectors, it causes the raising of their DC output level, thus lowering the final fringe visibility. In order to avoid this contrast loss, the detection holey mirror was chosen with a greater hole of diameter 7.5mm . In this way all the unwanted light is transmitted and gets blocked on a 2.8mm diameter iris placed in front of the reference detector.

3.3 DETECTION AND ACQUISITION

3.3.1 Amplified photodiodes

The detectors used to collect the heterodyne beats are InGaAs transimpedance amplified photodiodes (PD) with switchable gain (PDA10CS, Thorlabs Inc., USA). They provide between 17MHz and 12kHz bandwidth, depending on the set gain level, and a circular active area of diameter 1mm . InGaAs sensors are blind to visible light and make possible to operate the interferometer without worrying about any ambient or artificial light present inside the lab room. Moreover, this type of sensor offers a higher responsivity ($R > 0.5$) to NIR radiation with respect to silicon ($R < 0.1$). Incoming collimated beams are focused onto the PD active area by means of two 75mm singlets.

Before feeding them to the phasemeter, the PDs output signals were characterized with a fast oscilloscope. First, the light coming from arm 1 and from arm 2 have been analyzed separately. If we observe the spectrum reported in Fig. 3.17a, one notable peak is visible at about 104kHz . When the heterodyne lights are recombined a sharp peak at $f_{het} = 10\text{kHz}$ appears as expected, as well as a couple of intermodulation sidebands at $104\text{kHz} \pm f_{het}$ (see Figure 3.17b). This spurious peak, as anticipated in subsection 3.1.1, originates from the laser source: such an intensity modulation might be inherent to the laser natural emission or come from cavity instabilities due to ageing or unwanted back-reflections. If the latter case, the adoption of an optical isolator may be beneficial [70]. Another possible source of laser noise is the power supply, which should be checked and replaced if necessary. Further on the signals spectra, we observe that the spurious peaks get aliased at low frequencies when the voltage signals are sampled at low rate by the phasemeter. The aliasing issue can be seen in Figure 3.17c. The spurious peaks total power is -27.7dBc with respect to the beating carrier. Fortunately, the useful detection bandwidth is a small window of 2kHz around f_{het} , thus the voltage noise contribution falling into this window is much less than the total power of the unwanted peaks. By using the second equation in Table 2.1 and the measured ratios $\epsilon_{V_R}/V_{OR} = 7.365 \cdot 10^{-3}$ and $\epsilon_{V_M}/V_{OM} = 9.455 \cdot 10^{-3}$, we estimated an induced displacement error of 0.718nm . A narrow band-pass filtering around f_{het} before sampling would assure a better noise rejection for the system.

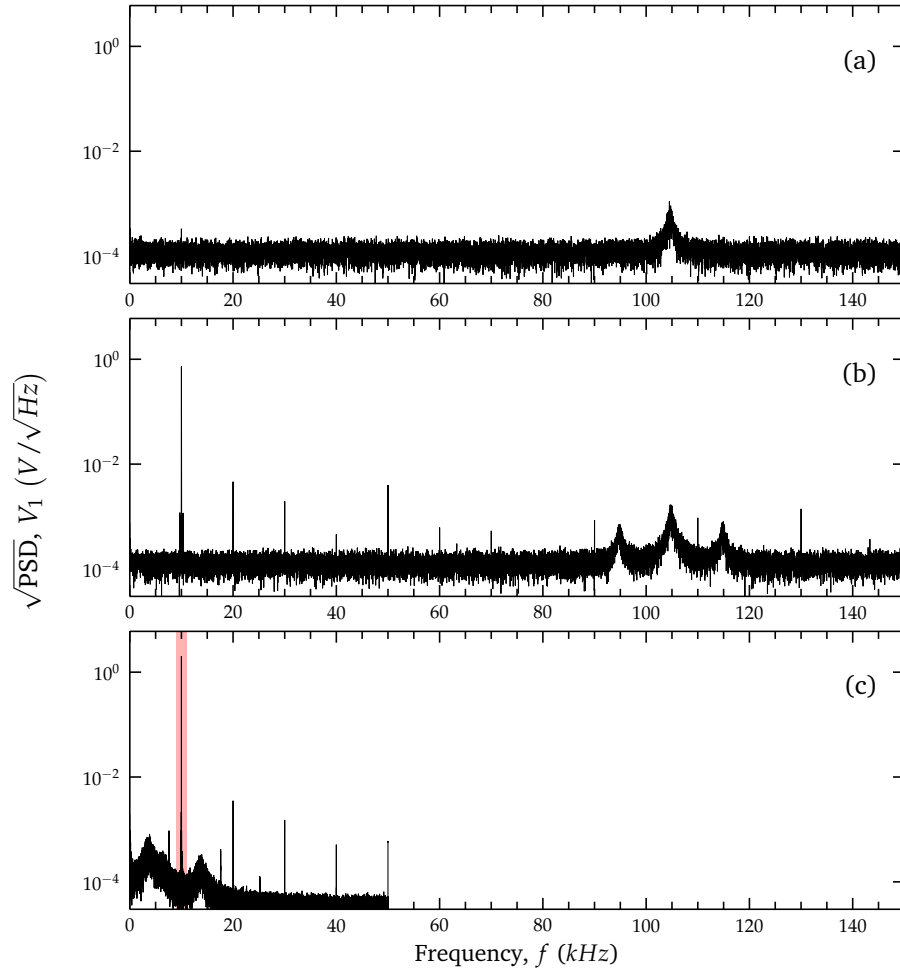


Figure 3.17: Spectral analysis of the raw voltage signals coming from the interferometer: (a) spectrum of the signal generated by arm 1 light through \mathcal{R} path; (b) spectrum of the signal generated by recombination light through \mathcal{R} path; (c) spectrum of the same signal as acquired by the phasemeter. The useful detection bandwidth is showed in red.

3.3.2 Digital phasemeter

The voltage outputs from the PDs are sent through coaxial cables to a 1.33 GHz real-time acquisition unit (cRIO-9035, National Instruments Corp., USA), featuring an integrated programmable FPGA (Kintex-7 7K70T, Xilinx Inc., USA) and a modular design. The system was selected as well for its inherent compatibility with the hardware and software already developed for the GINGERino experiment (see subsection 1.3.4). A compatible Hi-Z input module (NI-9223, National Instruments Corp., USA) provides four 16 bit synchronous ADCs operating at a data acquisition rate $f_s = 100 \text{ ksamples/s}$. The FPGA is directly interfaced to the ADCs and can perform the online high speed calculation of the lock-in algorithm described in subsection 2.3.2.

The internal reference signal $V_{LO} = c_{LO} + i s_{LO}$ is generated by means of the 2D planar rotation method [137]:

$$\phi_{LO} = 2\pi f_{het} \cdot \frac{1}{f_s} \quad (3.14)$$

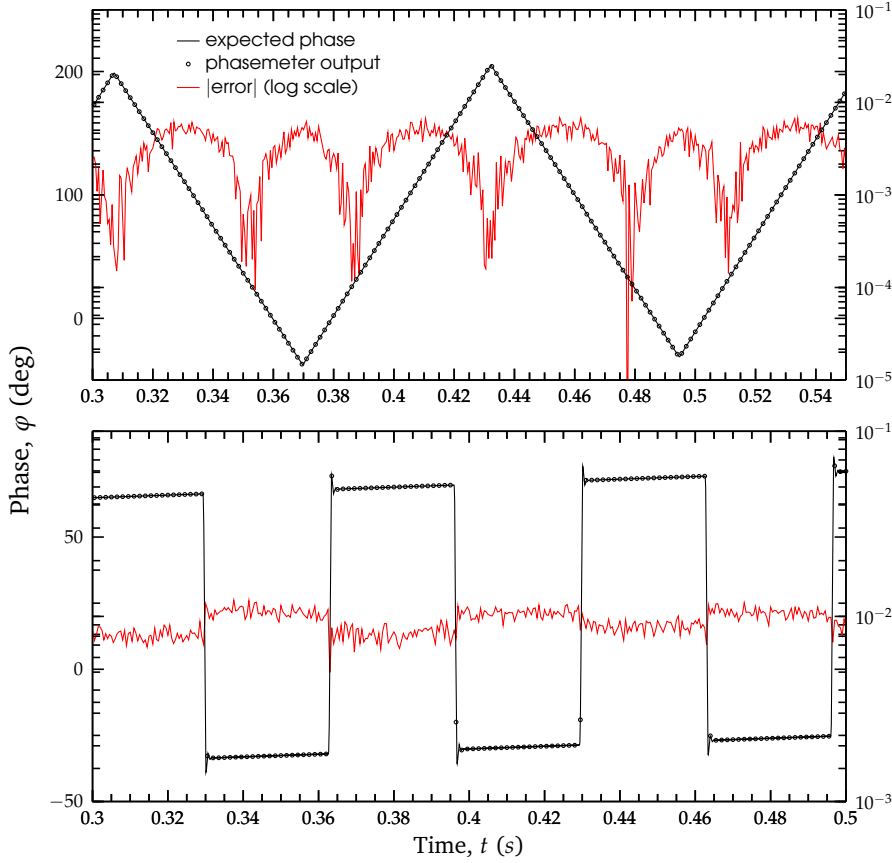


Figure 3.18: Response of the phasemeter to reference phase modulations imposed between two wave-generators: (a) 8 Hz sawtooth phase modulation with peak-to-peak (pk-pk) amplitude $A_{pk} = 240^\circ$ and (b) 15 Hz squarewave with $A_{pk} = 100^\circ$. The error magnitude (right log scale) is compatible with the numeric limitations produced by single precision floats.

$$c = \cos(\phi_{LO}) \quad (3.15)$$

$$s = \sin(\phi_{LO}) \quad (3.16)$$

$$c_{LO}(n+1) = c \cdot c_{LO}(n) - s \cdot s_{LO}(n) \quad (3.17)$$

$$s_{LO}(n+1) = s \cdot c_{LO}(n) + c \cdot s_{LO}(n) \quad (3.18)$$

where n/f_s is the time sample and $[c_{LO}(0) = 1, s_{LO}(0) = 0]$ are the starting values for the discrete vectors. This type of sinusoid generation algorithm is not affected by the typical diverging numerical error of the simpler $\sin(n/f_s)$ approach. Indeed, calculating the sines and cosines of growing time values leads to ever rising numeric approximation errors.

The 4th order LP digital filter has been set to a cut frequency of 1 kHz and the resulting phase values from \mathcal{R} and \mathcal{M} channels are unwrapped before subtraction and decimation. The measurement results are temporarily stored in a small buffer and then passed to the real-time system (1 GB DRAM, 4 GB storage memory). Here the data are decimated by a factor 50 and the phase measurement results are available with a rate of 2 ksamples/s. Instantaneous ADC values can be stored on demand as well, so that phase values can be calculated off-line at the host PC for debugging and testing purposes. To this end, the implemented phasemeter underwent an extensive series of data con-

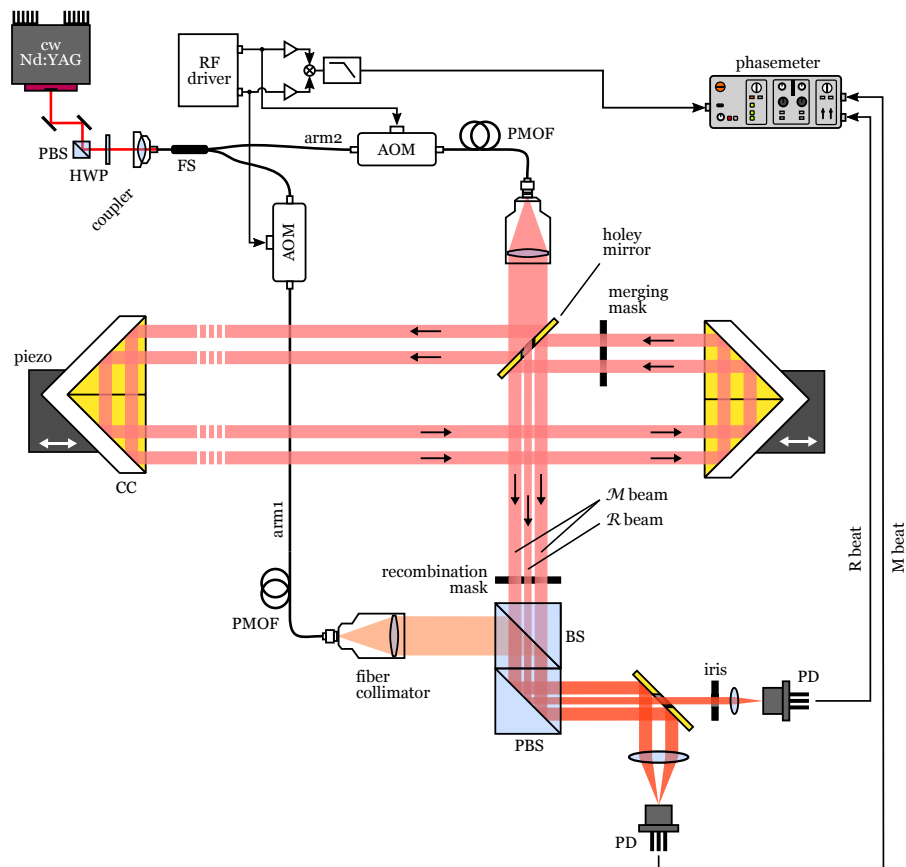


Figure 3.19: Simplified layout of the experimental setup.

sistency test, carried out by feeding it with two “perfect” beat signals provided by a couple of wave-generators (33521A and 33220A, Agilent Technologies, USA). The output from the phasemeter was compared with a reference phase, obtained by offline calculations on the raw signals from the wave-generators. The phasemeter algorithm was tested for abrupt phase changes, signals offset variations and unwrap artifacts, showing no major bugs and good agreement with the expected output (see Fig. 3.18).

The acquisition unit is also connected to each nano-positioner digital controller (E-727, Physik Instrumente (PI) GmbH & Co. KG., Germany) by an RS-232 interface. Suitable string commands are sent to the controller and used to generate corresponding voltage drive signals for the piezo stage. Moreover, the built-in capacitive sensors of the stage can output the instantaneous stage position under open and closed-loop operation. The readout of this sensor is available for the acquisition unit by proper query commands and can be used to track the fiducials position.

Finally, it worth to mention that the developed phasemeter also features a complete software backbone which guarantees continuous operation of the acquisition module, automatic phase data storage and the possibility of remotely monitoring the experiment.

4

RESULTS AND DISCUSSION

The present chapter offers a collection of experimental data, collected with the aim of characterize the performances of the previously described system. The measurements are divided into three main classes: *positioning tests*, carried out to check the gauge response consistency by programmatically moving one of the fiducials by known amounts; *performance tests*, aimed to the experimental characterization of the displacement uncertainty associated to the measurements; *environmental tests*, mainly conducted on longer time scales, they are performed to understand the influence of environmental parameters, such as vibration and temperature, on the gauge response. Before all, a brief evaluation of the random errors contribution is conducted.

4.1 RANDOM ERRORS ESTIMATION

Considering the random error contributions, we can now substitute the parameters in Tab. 2.1 with the typical value from our experimental setup. The laser crystal is operated at stable 25°C , which corresponds to a nominal optical frequency $\nu = 281.632\text{ THz}$; the laser manufacturer reports an $\epsilon_{\nu} = 20\text{ kHz}$ at 1 Hz , which increases up to 45 MHz over a 3 hours period; this corresponds to a long term relative frequency stability ϵ_{ν}/ν of about $1.6 \cdot 10^{-7}$. Each detection PD features an integrated switchable amplifier and the specified *NEP* embodies the combined contributions of detector noise and amplifier noise. The PDs, of responsivity $R = 0.729\text{ A/W}$ at λ_0 , are operated at different gain levels ($G_R = 4.75 \cdot 10^3\text{ V/A}$, $G_M = 4.75 \cdot 10^4\text{ V/A}$) and thus offer different *NEPs* ($NEP_R = 1 \cdot 10^{-11}\text{ W}/\sqrt{\text{Hz}}$, $NEP_M = 1.25 \cdot 10^{-12}\text{ W}/\sqrt{\text{Hz}}$) and bandwidths ($B_R = 8.5\text{ MHz}$, $B_M = 775\text{ kHz}$). The voltage sinusoids at the interferometer output have DC offsets $V_{OR} = 3.4\text{ V}$, $V_{OM} = 6.2\text{ V}$ and contrasts $C_R = 0.91$, $C_M = 0.49$. The ADCs input voltage range and bit depth are respectively $\Delta V = 20\text{ V}$ and $b = 16$, while the FPGA guarantees a $\tau_{jit} \leq 500\text{ ns}$ when reading from the I/O modules.

The displacement-independent random errors are reported in Fig. 4.1 as a function of the integration time. The instantaneous errors, affecting each phase measurement at the instant n/f_s , gets reduced by time averaging as described by Eq. 2.23. All random errors settle below 1 nm within 2 ms averaging, which is not far from the present 0.5 ms averaging period obtained by the implemented combination of LP filtering and decimation. Note that the contribution from time jitter dominates, probably due to the used τ_{jit} value, which is an upper bound specification rather than a “typical” one. Generally, the averaging time in GINGER observations will extend from days to years. The foreseen geometry control system will compensate for long-term deformations in a fairly quiet environment, therefore the required control bandwidth will not exceed 10 Hz . Limited to the random error contributions, this makes the

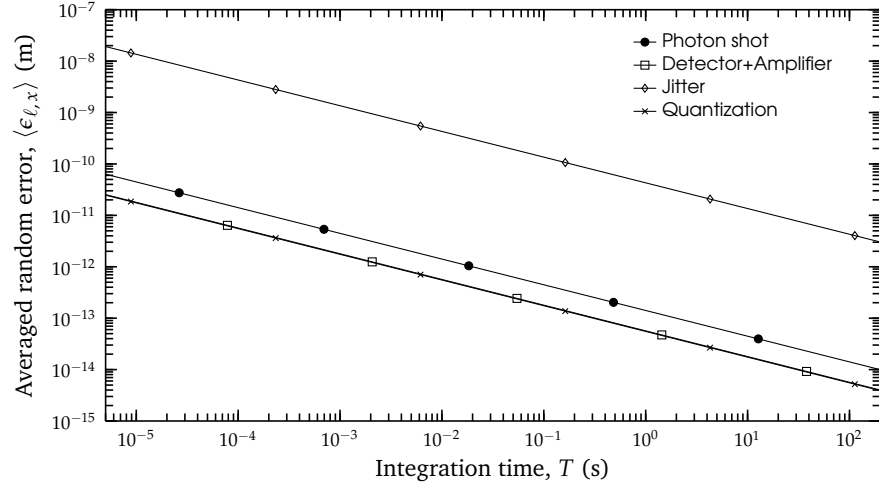


Figure 4.1: Random error contributions as a function of the integration time.

present interferometer nearly suitable for the final application, even though many additional factors should be considered in the determination of the real operational requirements. Among others, the fact that the same source unit will be conveniently used by multiple gauges, that implies a great reduction of the available optical power for the single one. The subsequent mandatory increase in PD gains may cause the photon noise and detector noise to overcome the quantization and jitter contributions.

As regards the other error types, i.e. displacement-dependent random, systematic and environmental, the developed gauge has been subjected to various dedicated tests, which are reported in the followings.

4.2 POSITIONING TESTS

To test the functionality of the gauge, a series of measurements were conducted with the aid of the nano-positioners installed below the retro-reflective fiducials. The aim of these measurements was to intentionally change one fiducial position and to use the interferometer to read out the corresponding phase offset. All collected data are compared to the piezo self-position output, provided by the embedded capacitive (CAP) sensor.

Response of the interferometer to a square wave fiducial displacement is reported in Fig. 4.2. The driving signal has 1 Hz frequency and pk-pk amplitude $A_{pk} = 10 \text{ nm}$. The good agreement between the CAP sensor data and the phasemeter data is highlighted by the residual error, which has a standard deviation of 1.27 nm . The error is calculated as a simple difference between the traces. The phasemeter data are detrended beforehand to get rid of any slow linear contribution. Similar tests have been conducted with different periodic patterns, some of them reported in Figure 4.3. For the widest amplitudes tested (Figures 4.3d and 4.3e), the error curves show a residual ripple which can be associated to mechanical vibrations of the retro-reflector assembly. These vibrations are detected by the external gauge and by the embedded capacitive sensor in different ways. Indeed, the CAP sensor monitors the position of the moving stage itself, while the displacement gauge detects movements in the fiducials mounted above. Conversely, sinusoidal driving with large amplitudes

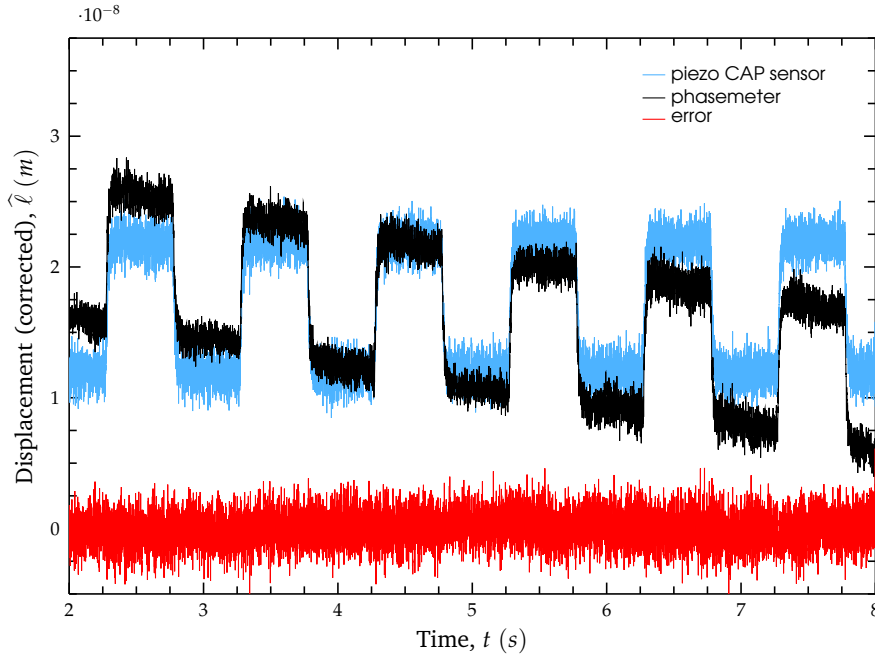


Figure 4.2: Gauge output during a positioning test: the fiducial was moved following a squarewave pattern of period 1s and pk-pk amplitude 10 nm.

does not introduces excess ripples (see item 4.3c, due to the absence of high frequency components which instead are present in the sawtooth and square waves.

Some linear sweeps were also executed, in order to identify possible sources of cyclic error. The results from physical optics simulations of the system, reported in subsection 3.2.2, provided us with the optical leakage values for the current configuration: $\rho_{LR} = 0.0877 \cdot 10^{-3}$ and $\rho_{LM} = 1.73 \cdot 10^{-3}$. These correspond, by applying Eq. 2.33, to an expected cyclic error with pk-pk amplitude of 0.154 nm, which is quite below the current instrument sensitivity. Actually, no sign of cyclic error could be identified from the data collected so far.

4.3 PERFORMANCE TESTS

The following measurements are intended to the characterization of the interferometer performances and to the identification of inherent measurement errors which can represent a limitation to future improvements of the gauge.

4.3.1 Best working conditions

In this test the displacement gauge was left to unattended data logging for extended time periods. The environmental noise was reduced to the lowest level allowed by the present laboratory conditions: air turbulence was minimized by switching off the air conditioning system and by isolating the interested lab area with heavy curtains; a rigid plastic enclosure was also placed to cover the fiducials axis in order to further limit acoustic noise and air circulation near the monitored distance. The underlying optical table is mounted on 4

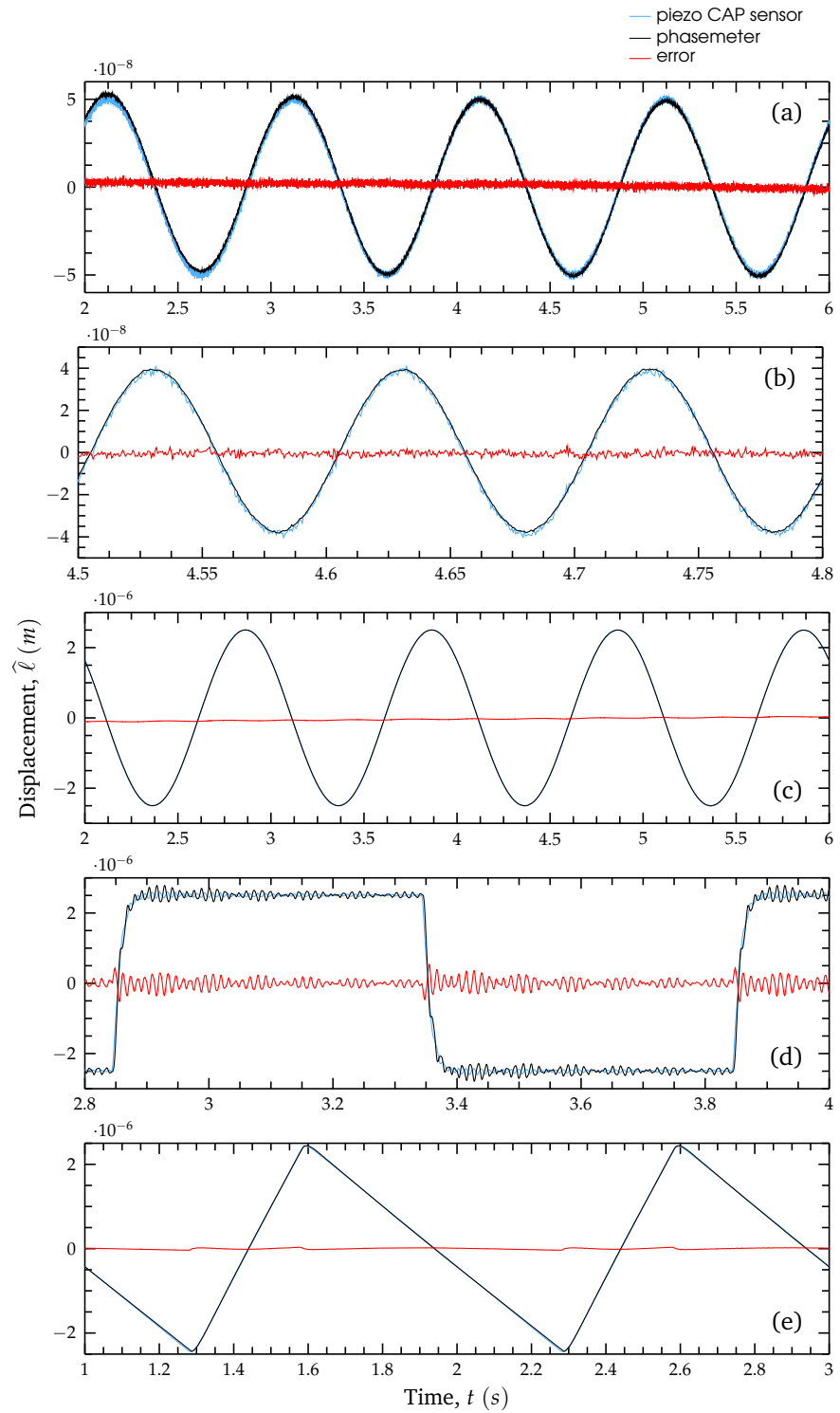


Figure 4.3: Gauge response to various displacement patterns:

- (a) sinewave $f=1\text{ Hz}$, $A_{pk}=100\text{ nm}$;
- (b) sinewave $f=10\text{ Hz}$, $A_{pk}=80\text{ nm}$;
- (c) sinewave $f=1\text{ Hz}$, $A_{pk}=5\text{ }\mu\text{m}$;
- (d) squarewave $f=1\text{ Hz}$, $A_{pk}=5\text{ }\mu\text{m}$;
- (e) sawtooth $f=1\text{ Hz}$, $A_{pk}=5\text{ }\mu\text{m}$.

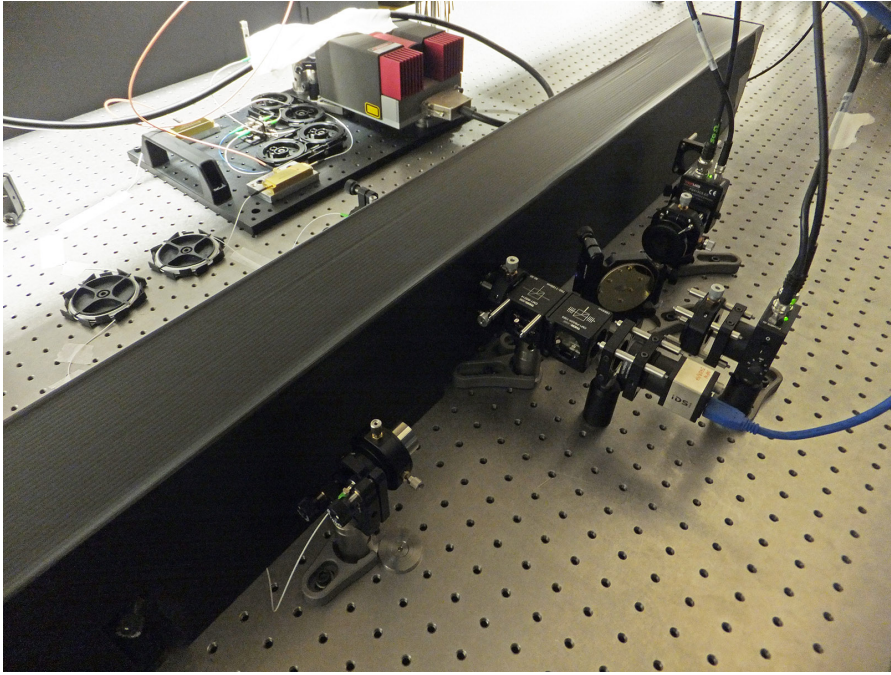


Figure 4.4: Picture of the displacement gauge with the racetrack protected by a plastic enclosure.

pneumatic vibration isolators, which kept operating during the whole logging runs. The piezo-capacitive actuator as well was switched off for this test.

Figure 4.5b shows the displacement power spectral density (PSD) of the interferometer in best working conditions. The PSD noise floor settles below $0.1 \text{ nm}/\sqrt{\text{Hz}}$ above 10 Hz , with some resonance peaks at higher frequencies, which will be discussed later on. The PSD then drifts up for lower frequencies, reaching $0.3 \text{ nm}/\sqrt{\text{Hz}}$ at 1 Hz and $3 \text{ nm}/\sqrt{\text{Hz}}$ at 100 mHz . The stability limitations of the present setup clearly show up for longer acquisition times, where slow mechanical relaxations and refractive index changes come into play. A constant linear drift can thus be seen in the original time data series of Fig. 4.5a. Below 1 Hz , long term effects including thermal, seismic and various other technical noise sources are expected to dominate, leading to a noise amplitude of $100 \text{ nm}/\sqrt{\text{Hz}}$ at 1 mHz .

4.3.2 Actuator noise

The noise contribution of the piezo actuator and other electronics was characterized by recording the phasemeter output data in two different situations: first the piezo was kept turned off, then it was switched on and used to move the fiducials by a known sinusoidal pattern of 10 Hz frequency and 100 nm pk-pk amplitude. The resulting spectra are shown in Fig. 4.6. The black (lower) curve represents the displacement PSD of the interferometer at rest: in the $10\text{-}500 \text{ Hz}$ range many resonance peaks can be seen, probably caused by residual mechanical vibrations. The most notable ones are located at 70 Hz , 82 Hz and 170 Hz . Beyond 500 Hz the electronics noise plateau dominates and its level remains below $10 \text{ pm}/\sqrt{\text{Hz}}$; this confirms an overestimate of the jitter error contribution previously calculated. The second spectrum reported (upper curve) is relative to the interferometer with an actuator turned on and moving.

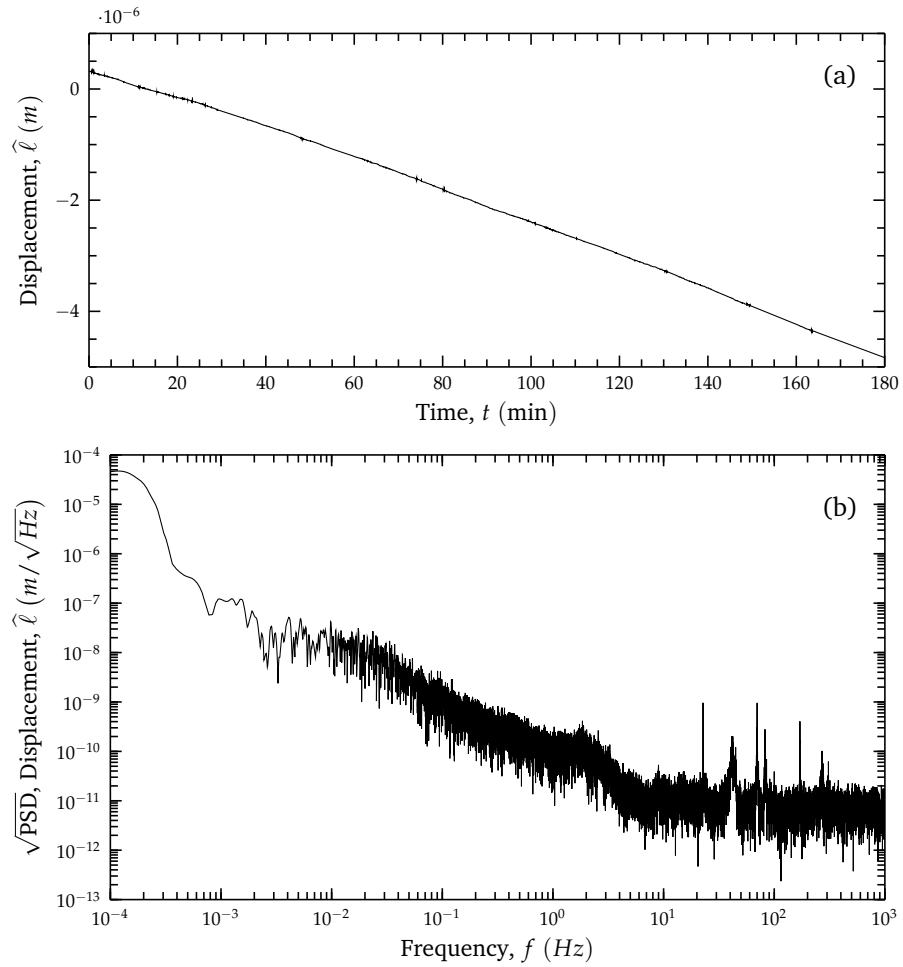


Figure 4.5: Monitored displacement in best working conditions over a 3h period: (a) time series and (b) power spectral density.

The spike at 10 Hz is due to the calibration signal and, as can be seen, there is a clear increase in the noise floor level due to the active position-control elements. This characterization gives a better insight on possible resolution limits arising from the use of these type of piezo actuators in the GINGER application. Given that the future switch to vacuum operation will require a substitution of the currently used stages, we suggest here a careful investigation on the noise PSDs provided by the manufacturers before purchase.

4.4 ENVIRONMENTAL TESTS

The following set of measurements were conducted with the aim of quantifying the contribution of the surrounding environment to the gauge performances.

4.4.1 Cancelable circuit operation

In order to test the positive effects of the cancelable circuit design, we computed the displacement values from the same dataset in two different ways.

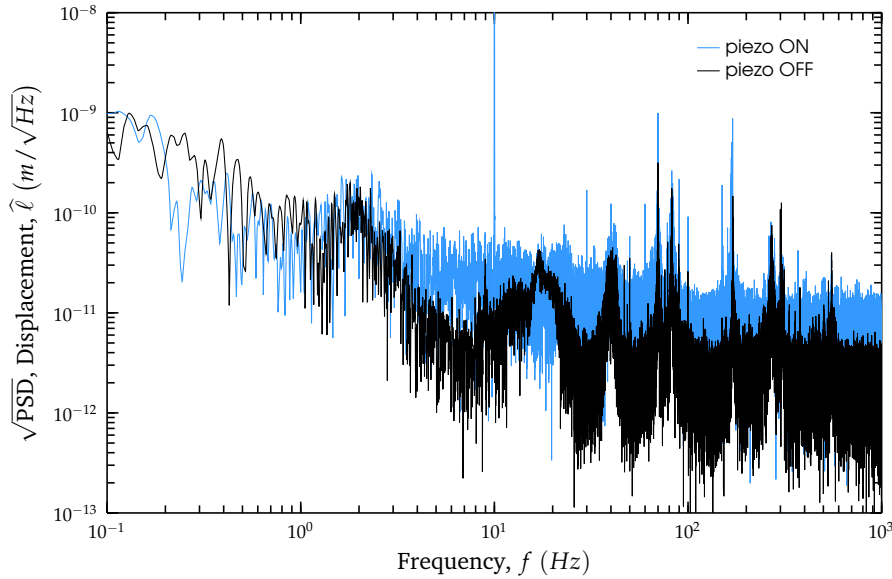


Figure 4.6: Noise spectral density of the interferometer with the piezo actuator turned off (bottom curve) and on (top curve). When the actuator is switched on, raising of the mechanical noise floor is clearly visible.

First, the standard procedure is used, consisting in the application of the lock-in algorithm to V_M and V_R , which are both generated by optical interference on the PDs. Then the same algorithm is applied to V_M and V_E , where V_M is the same as before, while V_E is a purely electrical reference, analogous to that showed in Figure 2.2a. This electrical reference is generated from a pair of buffered copies of the RF signals being fed to the AOMs. The signals at 150 MHz and 150.01 MHz are sent to an analog mixer (ZP-3MH-S+, Mini-circuits, USA) and the resulting output is then LP filtered by a discrete first-order RC circuit, with a cut frequency at about 100 kHz. Finally, after the elimination of the 300 MHz component, V_E is sampled by the real-time acquisition unit. As reported in Figure 4.7, the noise attenuation obtained by the cancelable circuit is remarkable. Most of the observed fluctuations in the noisy curve are caused by variations of the optical path difference between arm 1 and arm 2. The same fluctuations are common to V_R and V_M and do not appear in the black curve. The noise reduction mainly happens in the 10-1000 mHz range, where the PSD curve lowers by about one order of magnitude. We can state that this design has a great effect in removing the error from slow variations in optical path differences upstream of the holey mirror.

4.4.2 Vibration isolators operation

The effect of the pneumatic isolators (I-2000 Stabilizer, Newport Corp., USA) can also be measured with the present setup. Figure 4.8 shows two displacement PSDs relative to 100s data series collected respectively with isolators inactive and then activated. The rms noise over the 3-50 Hz bandwidth decreased from 0.71 nm to 0.03 nm, confirming the <0.1 transmissibility value reported by the manufacturer.

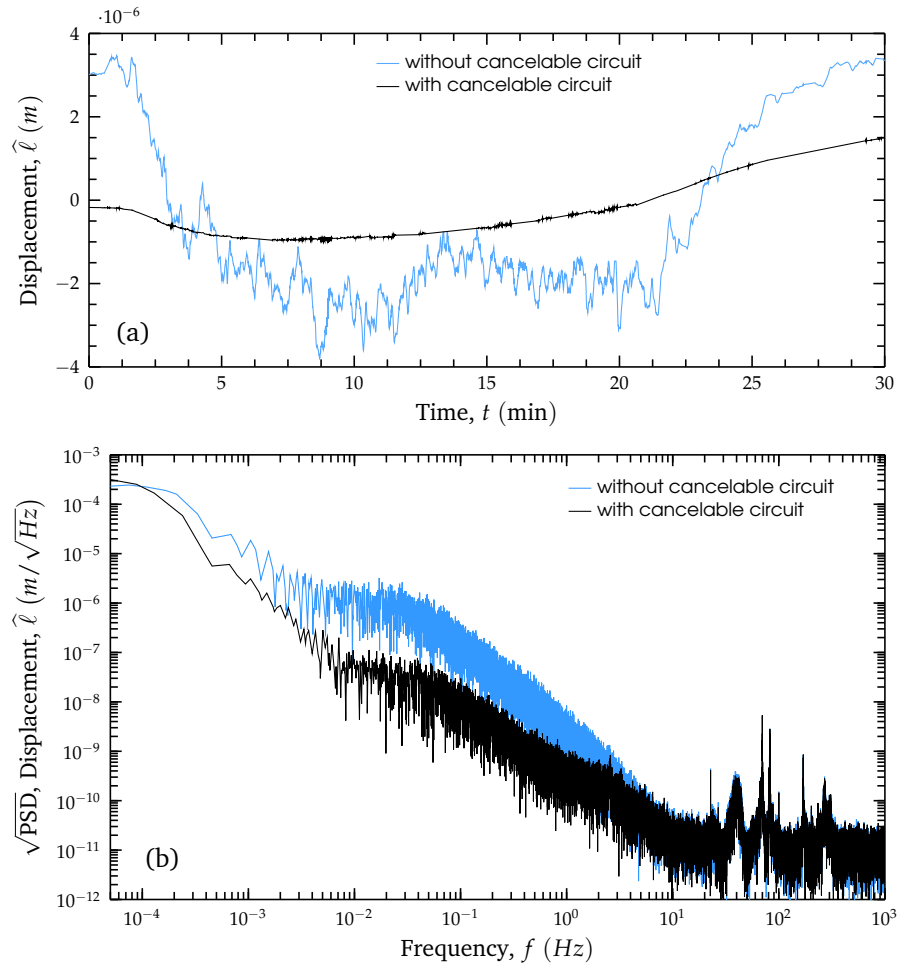


Figure 4.7: Comparison between two datasets relative to the same acquisition period. In (a) an extract from the two time series: the smoother one is obtained by applying the lock-in algorithm to V_R and V_M , both optically generated; the other curve results from applying the same algorithm to V_R and V_E , an electrical reference obtained from the RF driver. In (b) the corresponding PSDs are reported.

4.4.3 Ambient parameters changes

In our current test setup, thermal control and vacuum environment are not implemented. Moreover, all components are rigidly mounted on the optical bench, hence also its thermal expansion is likely to contribute to changes in L . A rough estimate of the worst case coupling factor for this type of effect is $12 \mu\text{m}/\text{K}$. Environmental variations can affect the reliability of the system in three ways: the first is thermally driven changes in the optical length of the transmissive optics downstream of the fiber splitter (PM fibers, AOMs and fiber collimators); the second is thermally driven changes in the holey mirror thickness; the third is variations of the effective optical path length caused by changes in air refractive index, as mentioned in section 2.4. For the first effect to be a problem there must be a differential change between the two paths of the interferometer, which cannot be the case, thanks to the cancelable circuit design. The second effect is much more critical because it acts directly and exclusively on the \mathcal{M} path. From the CTE value of the material used for

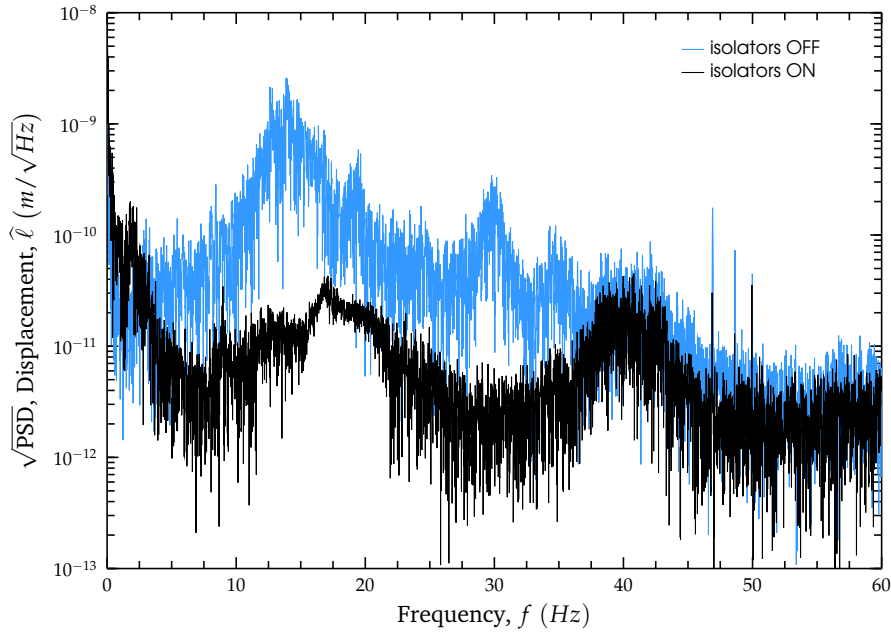


Figure 4.8: Responses of the interferometer at rest, with the pneumatic isolators turned off (upper curve) and on (lower curve).

the mirror substrate we can calculate a coupling factor of -3.68 nm/K . This may become a limitation for the gauge performances only in absence of a good temperature stability, which instead will be certainly guaranteed at the experimental site chosen for GINGER [20]. The third effect is right now the most relevant of all three and constitutes the main limitation to the long term stability of the present experiment, together with the components mechanical relaxations and the thermal expansion of the bench. A future upgrade of the gauge foresees placing the racetrack section of the interferometer in a vacuum chamber, thus eliminating the error to the roots. Nevertheless, it can still be interesting to investigate on the amount of displacement error induced by air refractive index changes in this type of heterodyne interferometers. To this end, temperature, pressure and relative humidity in proximity of the distance L have been monitored continuously by means of a data-logger (176 P1, Testo SE & Co. KGaA). The environmental datasets were then synchronized offline to the corresponding displacement time series by proper timestamping. Figure 4.9 reports the evolution of these ambient parameters over a period of $5h$. During the considered time window the temperature was deliberately made change by switching the air conditioning system on and off three times. We recall that the room in which this experiment is settled does not have any temperature control system installed, thus ambient changes are just passively induced. Indeed, temperature and humidity curves show typical exponential decays. We estimated the refractive index variations by applying the revised Edlén's equation reported in 2.42 through 2.46, assuming a $x_{\text{CO}_2} = 450 \text{ ppm}$. Propagation of errors gives us an uncertainty of $\epsilon_{\ell,n} \approx 8.361 \cdot 10^{-7}$. Once the refractive index is available, it is possible to reconstruct the induced deadpath error. From Eq. 2.39 we have:

$$\delta_{dp,n} = \frac{\Delta\lambda}{\lambda} L_0 = L_0 \left(1 - \frac{n}{n_0} \right), \quad (4.1)$$

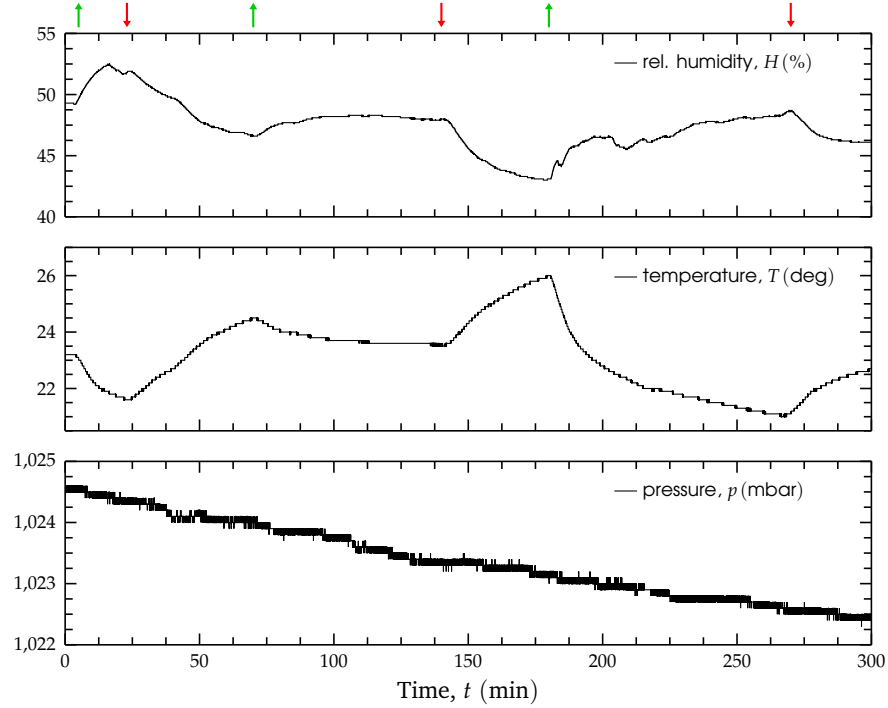


Figure 4.9: Monitored ambient parameters over a period of 5h. The arrows at top indicate the instants of activation (up, green) and deactivation (down, red) of the air conditioning system. Data quantization is visible due to the limited resolution of the sensors.

where n_0 is the refractive index at the beginning of measurement and $L_0 = 994\text{mm}$. Figure 4.10 shows the gauge output during a 5h period (black curve) and the corresponding index induced deadpath error $\delta_{dp,n}$. The uncertainty on the obtained deadpath values can be calculated by adapting Equation 2.40 to Equation 4.1:

$$\epsilon_{\ell,dp} = \sqrt{\left(L_0 \frac{\epsilon_n}{n_0}\right)^2 + \left(\left(1 - \frac{n}{n_0}\right) \epsilon_{L_0}\right)^2}, \quad (4.2)$$

with $\epsilon_{L_0} = 1\text{mm}$. The above expression gives an uncertainty $\epsilon_{\ell,dp} \approx 830.9\text{nm}$. This quite high value can be attributed to the high starting uncertainties of the ambient parameters. Nevertheless, a clear correlation between the detected displacement and the ambient parameters can be noticed by comparing Figures 4.10 and 4.9. The displacement curve after error subtraction is also displayed in blue. Unexpectedly, a piecewise linear trend remains after correction. This observed residual cannot be attributed to parasitic tilts of the holey mirror, which instead cause non-linear displacement errors (see “cosine error” in section 2.4), nor to laser frequency variations. A length variation of $50\mu\text{m}$ would imply an unrealistic 14GHz laser frequency shift for the considered deadpath length. Such a linear variation of the optical path may be caused by a combination of the bench thermal expansion and of the slow mechanical relaxation of some optical mounts.

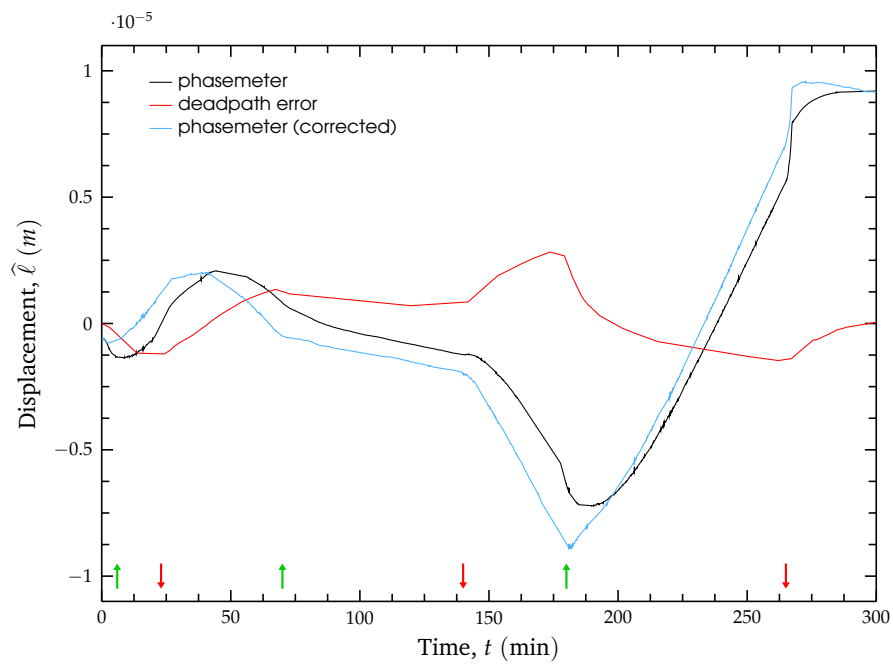


Figure 4.10: Monitored displacement over a period of 5 h (black), with related deadpath error (red) and resulting corrected trace (blue).

5

CONCLUSIONS AND FUTURE WORK

The motivation for the present study is the investigation of a new approach to the open issue of stabilizing an array of interdependent large ring-lasers. The structural stability of large ring-lasers is a main limitation of the present best performing devices and represents a big challenge for the feasibility of the next-generation multi-axial arrays. The target is to minimize the systematics associated with the geometrical deformations of the single optical cavity, as well as to prevent changes in the inter-distances and angles between different rings of the same array. Cavity deformations strongly compromise the sensitivity of a RL because of the direct dependence of the Sagnac frequency on the scale factor. Differently, uncertainties in the reciprocal orientations of different ring-lasers prevents the complete reconstruction of the rotation vector in the tridimensional space.

Detecting the Earth induced Lense-Thirring effect with 1% uncertainty imposes a target sensitivity below $\sim 10^{-16} \text{ rad/s}$ for the dedicated GINGER experiment. This translates into the challenge of stabilizing with sub-nanometer accuracy the variations of multiple mirror inter-distances. Being the mirrors a fundamental part of the RL cavities, the stabilization system must function without altering, or being altered by, the normal RLs operation. The approaches used in the past were based on two technique susceptible to influence from the active medium dynamics: the first was the locking of the RL emission frequency to an optical reference, in order to control the ring cavity perimeter; the second addresses more specifically the mirror inter-distances by controlling the absolute lengths of the diagonals in square shaped RLs.

Inspired by a space-borne application, we studied and started the development of an external metrology truss which will guarantee the monitoring and control of the GINGER geometry within its binding dimensional specifications. Being external to the ring cavities, it is inherently independent of any RL dynamics. The truss has a modular design and is composed by many identical displacement gauges, all sharing a common highly coherent source. Each gauge is placed along the axis connecting a pair of array fiducials and provides measurements of the changes in the mirror inter-distances. The information gathered from multiple gauges is then used to reconstruct the array geometry and to stabilize it by means of tri-axial nano-positioners. The experimental work here reported has focused on the implementation of a proof-of-concept design for the single displacement gauge.

Results

We have demonstrated a technique for high sensitivity displacement measurements, which is based on a heterodyne Mach-Zehnder interferometer and an effective implementation of the cancelable circuit scheme. The developed configuration is meant to be directly inserted along the distance of interest,

hence it is suitable for being matched to a large opto-mechanical structure such as that of GINGER. The measurement principle has been studied extensively and then implemented with a bench-top experiment which is giving promising results. The present interferometer shows a noise floor lower than $0.1 \text{ nm}/\sqrt{\text{Hz}}$ for frequencies above 10 Hz and an uncertainty of $3 \text{ nm}/\sqrt{\text{Hz}}$ at 0.1 Hz in best working conditions. Being operated in atmospheric conditions, the system performances are currently limited at low frequencies by mechanical drifts, thermal drifts and subsequent alterations of the air refractive index. Actually, the instrument shows a displacement noise of $100 \text{ nm}/\sqrt{\text{Hz}}$ at 1 mHz .

Here follows a brief summary of the main results obtained.

The heterodyne displacement interferometer has been studied in all its aspects, from the optical working principle to the possible phase retrieval schemes. A formalization of the cancelable circuit design is also presented, as well as the derivation of the analytical expressions for the many errors which can affect the displacement measurement.

The guidelines for the selection of a suitable laser source are given in terms of power and spectral purity. To this end, a set of numerical simulations was conducted for a qualitative evaluation of the effects of amplitude and frequency noise of the source on the optical beatings phenomenon. Beats visibility was confirmed to be directly related to the source degree of coherence. The ideal source required for the proper functioning of GEMS has an output power higher than 0.5 W and linewidth below the MHz .

A robust heterodyne source unit has been realized and tested: two heterodyne IR beams can be easily obtained and injected via fibers into the interferometric unit. Their frequency offset is widely tunable in the $0 \text{ Hz} - 10 \text{ MHz}$ frequency range. The laser amplitude noise was also characterized at low frequencies, showing possible induced displacement errors due to a spurious peak near f_{het} .

The realization of the cancelable circuit by wavefront splitting was possible thanks to the design of a custom mirror with a central tilted hole and reflective coating on both its front and back faces. Some technical issues arised from the first design of this component, namely mounts clearance and surfaces parallelism. These problems have been properly analyzed and will constitute useful lessons learned for the future development of the gauge.

We gave a simple analytical derivation of the systematic displacement error caused by the optical crosstalk occurring across the system. Diffraction at apertures and power leakages between complementary beam paths have been simulated by means of the Physical Optics Propagation tool offered by the Zemax[®] ray-tracing software. It was demonstrated that the introduction of properly designed masks can effectively minimize the optical mixing between wavefront splitted beams, leading to a factor 10 improvement with limited computing effort. The blocking masks have been realized and installed, though experimental evidence of their benefits will become possible only after a sensitivity upgrade of the system. Nevertheless, the developed optical model represents a reference point to start from for the optimization of the whole instrument.

A working FPGA-based phasemeter has been developed and successfully tested for response consistency. Online and offline phase retrieval algorithms have been implemented, as well as a complete software backbone which guarantees continuous operation of the acquisition module, automatic data storage and the possibility of remotely monitoring the experiment. The programmed

code is fully compatible with the hardware used in GINGERino, as requested by the GINGER project's common guidelines.

The realized experimental setup have been fully characterized with a series of specific displacement measurement, conducted on a test distance on 1 m. Controlled periodic translations of one fiducial let us validate the instrument response with comparisons to known displacement amounts. This showed a residual error with a standard deviation of 1.27 nm over 10 s. The system was then tested for extended time periods in the best possible environmental conditions. We demonstrated a noise floor below $0.1 \text{ nm}/\sqrt{\text{Hz}}$ above 10 Hz and we identified the amount of displacement noise induced by the activation of the nano-positioner. The effects of pneumatic isolators and of the cancelable circuit have been clearly characterized as well. Finally, a notable correlation of the detected displacement with the ambient parameters has been showed. The issue has been investigated by estimating the instantaneous changes in the air refractive index; then the related deadpath error was calculated and subtracted.

Future work

Many error sources have been identified and their contribution to the phase measurement was estimated. Nevertheless, a substantial upgrade of the current setup is mandatory for two main reasons: first, some unexplained long-term responses of the system need to be investigated; second, some of the foreseen error contributions (e.g. the cyclic error) could not be identified because they are presently overshadowed by other much stronger noise sources. The first issue can be addressed with a better characterization of the environment (direct tracking of the air index, multi-point monitoring of ambient parameters) and of the racetrack (thermal and mechanical model of its components). The second issue requires the elimination of the atmospheric influence and possibly a reduction of mechanical instabilities. These can be accomplished with the design of a more compact optical layout, rescaling its footprint from the current $360 \times 390 \text{ mm}^2$ to less than a half. All non-reflective optics should be eliminated, and use of low CTE substrates is suggested. All the components will then be mounted on a Zerodur breadboard and placed in a dedicated vacuum chamber, which will contain the retro-reflective fiducials as well. The optical upgrade will likely allow to reach the required sub-nanometer sensitivity and to insure it in the long-term.

The system is also ready to implement a control algorithm, now under development, for the identification and stabilization of the interested distance.

In the more general framework of GEMS, several key issues related to the external truss are to be investigated as well. The matching of GEMS with the GINGER opto-mechanical structure offers a big challenge in terms of design, manufacturing and characterization of the multi-directional fiducials: the unavoidable abbe and cosine errors must be modeled and compensated for. Once the measurements of the inter-fiducial distances will be available, an algorithm for the identification and estimation of the GINGER geometry will be mandatory. A control scheme design must then provide the stabilization of the overall system.

We are thus faced with many challenges, which will require hard work and complex technological solutions in order to bring large ring-lasers in the realm of General Relativity.

BIBLIOGRAPHY

- [1] Lorenzo Pantieri and Tommaso Gordini. *L'arte di scrivere con L^AT_EX*. 2011.
- [2] Georges Sagnac. “L'éther lumineux démontré par l'effet du vent relatif d'éther dans un interféromètre en rotation uniforme”. In: *CR Acad. Sci.* 157 (1913), pp. 708–710.
- [3] Guido Rizzi and Matteo Luca Ruggiero. “The relativistic Sagnac effect: two derivations”. In: *Relativity in Rotating Frames*. Springer, 2004, pp. 179–220.
- [4] K. U. Schreiber, A. Gebauer, and J.-P. R. Wells. “Closed-loop locking of an optical frequency comb to a large ring laser”. In: *Optics Letters* 38 (Sept. 2013), p. 3574. DOI: [10.1364/OL.38.003574](https://doi.org/10.1364/OL.38.003574).
- [5] K. U. Schreiber et al. “How to Detect the Chandler and the Annual Wobble of the Earth with a Large Ring Laser Gyroscope”. In: *Physical Review Letters* 107 (17 Oct. 2011), p. 173904. DOI: [10.1103/PhysRevLett.107.173904](https://doi.org/10.1103/PhysRevLett.107.173904).
- [6] F. Bosi et al. “Measuring gravitomagnetic effects by a multi-ring laser gyroscope”. In: *Physical Review D* 84 (2011), 122002(23). DOI: [10.1103/PhysRevD.84.122002](https://doi.org/10.1103/PhysRevD.84.122002).
- [7] A. Di Virgilio et al. “A ring lasers array for fundamental physics”. In: *Comptes Rendus Physique* 15.10 (2014), pp. 866–874. DOI: [10.1016/j.crhy.2014.10.005](https://doi.org/10.1016/j.crhy.2014.10.005).
- [8] B. Mashhoon, F. W. Hehl, and D. S. Theiss. “On the gravitational effects of rotating masses: The Thirring-Lense papers”. In: *General Relativity and Gravitation* 16.8 (1984), pp. 711–750. DOI: [10.1007/BF00762913](https://doi.org/10.1007/BF00762913).
- [9] Chien-ming Wu, J. Lawall, and R. D. Deslattes. “Heterodyne interferometer with subatomic periodic nonlinearity”. In: *Appl. Opt.* 38.19 (July 1999), pp. 4089–4094. DOI: [10.1364/AO.38.004089](https://doi.org/10.1364/AO.38.004089).
- [10] Ki-Nam Joo et al. “Simple heterodyne laser interferometer with subnanometer periodic errors”. In: *Optics letters* 34.3 (2009), pp. 386–388.
- [11] L. B. Ames et al. “SIM external metrology beam launcher (QP) development”. In: *Proceedings of SPIE: Interferometry in Space*. Vol. 4852. NASA JPL, 2003, pp. 347–354. DOI: [10.1117/12.460946](https://doi.org/10.1117/12.460946).
- [12] Alberto Donazzan et al. “Characterization of nanometer displacement gauge for dimensional control of large opto-mechanical structures”. In: *Opt. Express* (2017, submitted).
- [13] Alberto Donazzan, Giampiero Naletto, and Maria G. Pelizzo. “Study of the optical crosstalk in a heterodyne displacement gauge with cancelable circuit”. In: *Modeling Aspects in Optical Metrology VI*. Vol. 10330. International Society for Optics and Photonics. 2017, 103300F. DOI: [10.1117/12.2270193](https://doi.org/10.1117/12.2270193).

- [14] Antonello Ortolan et al. “GINGER: an array of ring lasers for testing fundamental physics”. In: *Proceedings of the MG14 Meeting on General Relativity*. Ed. by Massimo Bianchi, Robert T. Jantzen, and Ruffini Remo. 2017.
- [15] Alberto Donazzan et al. “A network of heterodyne laser interferometers for monitoring and control of large ring-lasers”. In: *SPIE Optical Engineering + Applications*. 2016, pp. 1–8. DOI: [10.1117/12.2237638](https://doi.org/10.1117/12.2237638).
- [16] Alberto Donazzan et al. “External metrology system for the stabilization of large ring-lasers”. In: *Metrology for Aerospace (MetroAeroSpace), 2016 IEEE*. IEEE. 2016, pp. 266–270.
- [17] J. Belfi et al. “Very high sensitivity laser gyroscopes for general relativity tests in a ground laboratory”. In: *2016 European Frequency and Time Forum (EFTF)*. Apr. 2016, pp. 1–4. DOI: [10.1109/EFTF.2016.7477839](https://doi.org/10.1109/EFTF.2016.7477839).
- [18] A. Ortolan et al. “The GINGER project and status of the GINGERino prototype at LNGS”. In: *Proceedings, 14th International Conference on Topics in Astroparticle and Underground Physics (TAUP 2015)*. Vol. 718. 7. 2016, p. 072003. DOI: [10.1088/1742-6596/718/7/072003](https://doi.org/10.1088/1742-6596/718/7/072003).
- [19] A. Di Virgilio et al. “The GINGER Project”. In: *Nuclear Physics B-Proceedings Supplements (2016)*, pp. 1–8.
- [20] A. Di Virgilio et al. “The GINGER Project and status of the ring-laser of LNGS”. In: *Proceedings of the XVI International Workshop on Neutrino Telescopes (NEUTEL2015)*. Palazzo Franchetti, Venice, Italy, Mar. 2015, pp. 2–6.
- [21] I. Ciufolini and J. A. Wheeler. *Gravitation and Inertia*. Princeton series in physics. Princeton University Press, 1995.
- [22] C. W. F. Everitt et al. “Gravity Probe B: Final Results of a Space Experiment to Test General Relativity”. In: *Physical Review Letters* 106 (22 May 2011), p. 221101. DOI: [10.1103/PhysRevLett.106.221101](https://doi.org/10.1103/PhysRevLett.106.221101).
- [23] I. Ciufolini and E. C. Pavlis. “A confirmation of the general relativistic prediction of the Lense-Thirring effect”. In: *Nature* 431 (Oct. 2004), pp. 958–960. DOI: [10.1038/nature03007](https://doi.org/10.1038/nature03007).
- [24] Ignazio Ciufolini et al. “Testing gravitational physics with satellite laser ranging”. In: *The European Physical Journal Plus* 126.8 (2011), pp. 1–19.
- [25] I. Ciufolini et al. “A test of general relativity using the LARES and LAGEOS satellites and a GRACE Earth gravity model. Measurement of Earth’s dragging of inertial frames”. In: *European Physical Journal C* 76, 120 (Mar. 2016), p. 120. DOI: [10.1140/epjc/s10052-016-3961-8](https://doi.org/10.1140/epjc/s10052-016-3961-8).
- [26] Ignazio Ciufolini et al. “A new laser-ranged satellite for General Relativity and space geodesy: I. An introduction to the LARES2 space experiment”. In: *The European Physical Journal Plus* 132.8 (2017), p. 336.
- [27] F. Flechtner et al. “Current Status Of The GRACE Follow-On Mission”. In: *EGU General Assembly Conference Abstracts*. Vol. 19. EGU General Assembly Conference Abstracts. Apr. 2017, p. 4566.
- [28] Olivier Darrigol. “Georges Sagnac: A life for optics”. In: *Comptes Rendus Physique* 15.10 (2014), pp. 789–840.

- [29] G. E. Stedman, R. B. Hurst, and K. U. Schreiber. “On the potential of large ring lasers”. In: *Optics Communications* 279 (2007), pp. 124–129. DOI: [10.1016/j.optcom.2007.07.011](https://doi.org/10.1016/j.optcom.2007.07.011).
- [30] T. L. Gustavson, P. Bouyer, and M. A. Kasevich. “Precision rotation measurements with an atom interferometer gyroscope”. In: *Physical Review Letters* 78.11 (1997), p. 2046.
- [31] K. U. Schreiber and J. P. R. Wells. “Invited Review Article: Large ring lasers for rotation sensing”. In: *Review of Scientific Instruments* 84 (4 2013), pp. 041101–. DOI: [10.1063/1.4798216](https://doi.org/10.1063/1.4798216).
- [32] M. O. Scully, M. S. Zubairy, and M. P. Haugan. “Proposed optical test of metric gravitation theories”. In: *Phys. Rev. A* 24 (4 Oct. 1981), pp. 2009–2016. DOI: [10.1103/PhysRevA.24.2009](https://doi.org/10.1103/PhysRevA.24.2009). URL: <https://link.aps.org/doi/10.1103/PhysRevA.24.2009>.
- [33] G. E. Stedman. “Ring-laser tests of fundamental physics and geophysics”. In: *Reports on progress in physics* 60.6 (1997), p. 615.
- [34] Victor Vali and R. W. Shorthill. “Fiber ring interferometer”. In: *Applied optics* 15.5 (1976), pp. 1099–1100.
- [35] Warren M. Macek and D. T. M. Davis Jr. “Rotation rate sensing with traveling-wave ring lasers”. In: *Applied Physics Letters* 2.3 (1963), pp. 67–68.
- [36] W. W. Chow et al. “The ring laser gyro”. In: *Reviews of Modern Physics* 57.1 (1985), p. 61.
- [37] F. Aronowitz. “Fundamentals of the Ring Laser Gyro”. In: *Optical Gyros and their Application* 339 (1999).
- [38] Alessandro Beghi et al. “Compensation of the laser parameter fluctuations in large ring-laser gyros: a Kalman filter approach”. In: *Appl. Opt.* 51.31 (Nov. 2012), pp. 7518–7528. DOI: [10.1364/AO.51.007518](https://doi.org/10.1364/AO.51.007518).
- [39] G. E. Stedman et al. “Harmonic analysis in a large ring laser with backscatter-induced pulling”. In: *Physical Review A* 51.6 (1995), p. 4944.
- [40] Davide Cuccato. “Modeling, estimation and control of ring laser gyroscopes for the accurate estimation of the earth rotation”. In: (Jan. 2015).
- [41] K. Ulrich Schreiber et al. “Sensing earth’s rotation with a helium–neon ring laser operating at 1.15 μm ”. In: *Optics Letters* 40.8 (2015), pp. 1705–1708.
- [42] Robert B. Hurst et al. “Correction of backscatter-induced systematic errors in ring laser gyroscopes”. In: *Appl. Opt.* 53.31 (Nov. 2014), pp. 7610–7618. DOI: [10.1364/AO.53.007610](https://doi.org/10.1364/AO.53.007610).
- [43] Richard Douglas Graham. “New concepts for operating ring laser gyroscopes”. PhD thesis. University of Canterbury, 2010.
- [44] Karl Ulrich Schreiber et al. “The Large Ring Laser G for Continuous Earth Rotation Monitoring”. In: *Pure and applied geophysics* 166.8-9 (2009), pp. 1485–1498.
- [45] K. U. Schreiber, A. Gebauer, and J-P R. Wells. “Long-term frequency stabilization of a 16 m 2 ring laser gyroscope”. In: *Optics letters* 37.11 (2012), pp. 1925–1927.

- [46] K. U. Schreiber, A. Gebauer, and J-P. R. Wells. “Closed-loop locking of an optical frequency comb to a large ring laser”. In: *Optics letters* 38.18 (2013), pp. 3574–3577.
- [47] Ulrich Schreiber et al. “The GEOsensor project: rotations—a new observable for seismology”. In: *Observation of the Earth System from Space*. Springer, 2006, pp. 427–443.
- [48] Angela Di Virgilio et al. “Performances of ‘G-Pisa’: a middle size gyro-laser”. In: *Classical and Quantum Gravity* 27.8 (2010), p. 084033.
- [49] J. Belfi et al. “A 1.82 m² ring laser gyroscope for nano-rotational motion sensing”. In: *Applied Physics B* 106.2 (2012), pp. 271–281. DOI: [10.1007/s00340-011-4721-y](https://doi.org/10.1007/s00340-011-4721-y).
- [50] Jacopo Belfi et al. “Performance of “G-Pisa” ring laser gyro at the Virgo site”. In: *Journal of seismology* 16.4 (2012), pp. 757–766.
- [51] Jacopo Belfi et al. “Horizontal rotation signals detected by “G-Pisa” ring laser for the Mw= 9.0, March 2011, Japan earthquake”. In: *Journal of Seismology* 16.4 (2012), pp. 767–776.
- [52] Davide Cuccato et al. “Controlling the non-linear intracavity dynamics of large He–Ne laser gyroscopes”. In: *Metrologia* 51.1 (2014), p. 97.
- [53] Rosa Santagata et al. “Optimization of the geometrical stability in square ring laser gyroscopes”. In: *Classical and Quantum Gravity* 32.5 (2015), p. 055013.
- [54] J Belfi et al. “Interferometric length metrology for the dimensional control of ultra-stable ring laser gyroscopes”. In: *Classical and Quantum Gravity* 31.22 (2014), p. 225003.
- [55] J. Belfi et al. “Absolute Control of the Scale Factor in GP2 Laser Gyroscope: Toward a Ground Based Detector of the Lense-Thirring Effect”. In: *European Frequency and Time Forum & IEEE International Frequency Control Symposium (EFTF/IFC), 2013 Joint*. 2013, pp. 795–798. DOI: [10.1109/EFTF-IFC.2013.6702268](https://doi.org/10.1109/EFTF-IFC.2013.6702268).
- [56] Rosa Santagata. “Sub-nanometer length metrology for ultra-stable ring laser gyroscopes”. In: (2015). URL: http://www.infn.it/thesis/thesis_dettaglio.php?tid=10057.
- [57] J. Belfi et al. “First Results of GINGERino, a deep underground ring-laser”. In: *arXiv preprint arXiv:1601.02874* (2016).
- [58] Jacopo Belfi et al. “Deep underground rotation measurements: GINGERino ring laser gyroscope in Gran Sasso”. In: *Review of Scientific Instruments* 88.3 (2017), p. 034502.
- [59] ROMY website. URL: <https://www.geophysik.uni-muenchen.de/ROMY/>.
- [60] H. Igel et al. “ROMY: A 4-component large ring laser for geophysics”. In: *AGU Fall Meeting Abstracts*. Dec. 2016.
- [61] André Gebauer et al. “Design and construction of a large 4C ring laser: ROMY”. In: *EGU General Assembly Conference Abstracts*. Vol. 19. 2017, p. 10170.
- [62] Karl Ulrich Schreiber et al. “Integration and initial operation of the multi-component large ring laser structure ROMY”. In: *EGU General Assembly Conference Abstracts*. Vol. 19. 2017, p. 5628.

- [63] *IERS Annual Report 2014*. Tech. rep. Frankfurt am Main: Verlag des Bundesamts für Kartographie und Geodäsie: International Earth Rotation and Reference Systems Service, Central Bureau, 2015.
- [64] Angelo Tartaglia et al. “Testing general relativity by means of ring lasers”. In: *The European Physical Journal Plus* 132.2 (2017), p. 73.
- [65] Angela D. V. Di Virgilio et al. “GINGER: A feasibility study”. In: *The European Physical Journal Plus* 132.4 (2017), p. 157.
- [66] P. G. Halverson et al. “Progress towards picometer accuracy laser metrology for the space interferometry mission”. In: *Proceedings of ICSO 2000, 4th International Conference on Space Optics*. NASA JPL, 2000, pp. 417–428.
- [67] P. G. Halverson et al. “Progress towards picometer accuracy laser metrology for the Space Interferometry Mission - Update for ICSO 2004”. In: *Proceedings of ICSO 2004, 5th International Conference on Space Optics*. NASA JPL, 2004, pp. 515–522.
- [68] B. Nemati. “SIM PlanetQuest: Status and Recent Progress”. In: *Proceedings of SPIE: Advances in Stellar Interferometry*. Vol. 6268. NASA JPL, 2006. DOI: [10.1117/12.665678](https://doi.org/10.1117/12.665678).
- [69] J. E. Logan et al. “Automatic alignment of a displacement-measuring heterodyne interferometer”. In: *Applied Optics* 41 (2002), pp. 4314–4317. DOI: [10.1364/AO.41.004314](https://doi.org/10.1364/AO.41.004314).
- [70] John Lawall and Ernest Kessler. “Michelson interferometry with 10 pm accuracy”. In: *Review of Scientific Instruments* 71.7 (2000), pp. 2669–2676. DOI: [10.1063/1.1150715](https://doi.org/10.1063/1.1150715).
- [71] Gary M. Kuan. “Metrology optical power budgeting in SIM using statistical analysis techniques”. In: *Optical and Infrared Interferometry*. Vol. 7013. Proc. SPIE. July 2008, p. 70134V. DOI: [10.1117/12.790459](https://doi.org/10.1117/12.790459).
- [72] John N. Dukes and Gary B. Gordon. “A two-hundred-foot yardstick with graduations every micronch”. In: *Hewlett-Packard Journal* 21.2 (1970), pp. 2–8.
- [73] C. R. Steinmetz. “Sub-micron position measurement and control on precision machine tools with laser interferometry”. In: *Precision Engineering* 12.1 (1990), pp. 12–24.
- [74] B Shirinzadeh et al. “Laser interferometry-based guidance methodology for high precision positioning of mechanisms and robots”. In: *Robotics and Computer-Integrated Manufacturing* 26.1 (2010), pp. 74–82.
- [75] Richard K Leach et al. “The European nanometrology landscape”. In: *Nanotechnology* 22.6 (2011), p. 062001.
- [76] Harald Bosse and Günter Wilkening. “Developments at PTB in nanometrology for support of the semiconductor industry”. In: *Measurement Science and Technology* 16.11 (2005), p. 2155.
- [77] Marco Pisani et al. “Comparison of the performance of the next generation of optical interferometers”. In: *Metrologia* 49.4 (2012), p. 455.
- [78] F. Zhao. “Development of high precision laser heterodyne metrology gauges”. In: *Proceedings of SPIE: Advanced Sensor Systems and Applications II*. Vol. 5634. NASA JPL, 2005. DOI: [10.1117/12.569844](https://doi.org/10.1117/12.569844).

- [79] Samuel A Leveque et al. “Toward nanometer accuracy laser metrology for phase-referenced interferometry with the VLTI”. In: *Proceedings of SPIE*. Vol. 4838. 2003, pp. 983–994.
- [80] Matthew J Dudik et al. “Development of a precision cryogenic dilatometer for James Webb Space Telescope materials testing”. In: *Proc. SPIE* 5179 (2003), pp. 5179–10. DOI: [10.1117/12.506482](https://doi.org/10.1117/12.506482).
- [81] Vinzenz Wand. “Interferometry at low frequencies: Optical phase measurement for LISA and LISA Pathfinder”. PhD thesis. Gottfried Wilhelm Leibniz Universität Hannover, 2007.
- [82] BS Sheard et al. “Intersatellite laser ranging instrument for the GRACE follow-on mission”. In: *Journal of Geodesy* (2012), pp. 1–13.
- [83] Norman Bobroff. “Recent advances in displacement measuring interferometry”. In: *Measurement Science and Technology* 4.9 (1993), p. 907.
- [84] Andrew J. Fleming. “A review of nanometer resolution position sensors: Operation and performance”. In: *Sensors and Actuators A: Physical* 190 (2013), pp. 106–126.
- [85] M. Hirano. “Optical Heterodyne Measurement Method”. In: *Handbook of Optical Metrology*. Ed. by Toru Yoshizawa. CRC Press, 2009. DOI: [10.1201/9781420019513.ch10](https://doi.org/10.1201/9781420019513.ch10).
- [86] Jonathan D. Ellis and Society of Photo-optical Instrumentation Engineers. *Field Guide to Displacement Measuring Interferometry*. Vol. FG30. SPIE Press, 2014.
- [87] Bryan K. A. Ngoi and Krishnan Venkatakrishnan. “Techniques to eliminate error induced due to acousto-optic modulator vibration in heterodyne interferometry”. In: *Optical Engineering* 38.12 (1999), pp. 2050–2054.
- [88] James A. Smith and Christian P. Burger. “Digital phase demodulation in heterodyne sensors”. In: *Optical Engineering* 34.9 (1995), pp. 2793–2801. DOI: [10.1117/12.212980](https://doi.org/10.1117/12.212980).
- [89] P. Köchert et al. “Phase measurement of various commercial heterodyne He–Ne-laser interferometers with stability in the picometer regime”. In: *Measurement Science and Technology* 23.7 (2012), p. 074005.
- [90] *Simple Phase Meter Operates to 10MHz (HA5024, HFA3102)*. AN9637.1. Intersil Corporation. Oct. 2004.
- [91] Peter G. Halverson and Frank M. Loya. “Signal processing for order 10 pm accuracy displacement metrology in real-world scientific applications”. In: *5th International Conference on Space Optics*. Vol. 554. 2004, pp. 571–577.
- [92] Andrew J. Stevenson et al. “Quantum-noise-limited interferometric phase measurements”. In: *Applied optics* 32.19 (1993), pp. 3481–3493.
- [93] P. L. Richards. “Bolometers for infrared and millimeter waves”. In: *Journal of Applied Physics* 76.1 (Aug. 1994), pp. 1–24. DOI: [10.1063/1.357128](https://doi.org/10.1063/1.357128).
- [94] D. G. Manolakis and J. G. Proakis. *Digital Signal Processing: Principles, Algorithms, and Applications*. 3rd. Prentice Hall, 1996.

- [95] Paul Smith. *Little Known Characteristics of Phase Noise*. AN-741 Application Note. Analog Devices. 2004.
- [96] T. L. Schmitz, D. Chu, and L. III Houck. “First-order periodic error correction: validation for constant and non-constant velocities with variable error magnitudes”. In: *Measurement Science and Technology* 17.12 (2006), p. 3195. DOI: [10.1088/0957-0233/17/12/001](https://doi.org/10.1088/0957-0233/17/12/001).
- [97] Haijin Fu et al. “Simple method for reducing the first-order optical nonlinearity in a heterodyne laser interferometer”. In: *Applied optics* 54.20 (2015), pp. 6321–6326.
- [98] Oliver P. Lay and Serge Dubovitsky. “Polarization compensation: a passive approach to a reducing heterodyne interferometer nonlinearity”. In: *Opt. Lett.* 27.10 (May 2002), pp. 797–799. DOI: [10.1364/OL.27.000797](https://doi.org/10.1364/OL.27.000797).
- [99] S. J. A. G. Cosijns, Han Haitjema, and P. H. J. Schellekens. “Modeling and verifying non-linearities in heterodyne displacement interferometry”. In: *Precision Engineering* 26.4 (2002), pp. 448–455. DOI: [10.1016/S0141-6359\(02\)00150-2](https://doi.org/10.1016/S0141-6359(02)00150-2).
- [100] Liping Yan et al. “Analysis and verification of the nonlinear error resulting from the misalignment of a polarizing beam splitter in a heterodyne interferometer”. In: *Measurement Science and Technology* 26.8 (2015), p. 085006.
- [101] Yekta Gursel. “Laser metrology gauges for OSI”. In: *Proc. SPIE*. Vol. 1947. 1993, pp. 188–197. DOI: [10.1117/12.155740](https://doi.org/10.1117/12.155740).
- [102] Peter G. Halverson et al. “Techniques for the reduction of cyclic errors in laser metrology gauges for the space interferometry mission”. In: *ASPE 2001 Conference*. 2001.
- [103] Mitsuru Tanaka, Tohru Yamagami, and Kan Nakayama. “Linear interpolation of periodic error in a heterodyne laser interferometer at subnanometer levels (dimension measurement)”. In: *IEEE Transactions on Instrumentation and Measurement* 38.2 (1989), pp. 552–554.
- [104] Tony Schmitz and John Beckwith. “Acousto-optic displacement measuring interferometer: a new heterodyne interferometer with Ångstrom-level periodic error”. In: *Journal of modern optics* 49.13 (2002), pp. 2105–2114.
- [105] Daniel A. Shaddock. “Digitally enhanced heterodyne interferometry”. In: *Opt. Lett.* 32.22 (Nov. 2007), pp. 3355–3357. DOI: [10.1364/OL.32.003355](https://doi.org/10.1364/OL.32.003355).
- [106] Jeremias Seppä et al. “A method for linearization of a laser interferometer down to the picometre level with a capacitive sensor”. In: *Measurement Science and Technology* 22.9 (2011), p. 094027.
- [107] Marco Pisani, Giovanni Mana, and Anna M. Nobili. “Design of an interferometric displacement sensor with picometer resolution for the Galileo-Galilei mission”. In: *Metrology for Aerospace (MetroAeroSpace), 2015 IEEE*. IEEE. 2015, pp. 591–595.
- [108] L. L. Ames, R. M. Bell, and K. Dutta. *Beam masking to reduce cyclic error in beam launcher of interferometer*. US Patent 6,922,249. July 2005.

- [109] Kalyan Dutta, Robert S. Benson, and M. Shao. “Performance modeling of optical metrology systems”. In: *Proceedings of SPIE*. Vol. 4852. 2003, pp. 839–848.
- [110] Xu Wang. “The mask designs for Space Interferometer Mission (SIM)”. In: vol. 7013. 2008, pp. 701352–11. DOI: [10.1117/12.787256](https://doi.org/10.1117/12.787256).
- [111] Hong Tang and Feng Zhao. “Estimation of cyclic error due to scattering in the internal OPD metrology of the Space Interferometry Mission”. In: vol. 5776. 2005, pp. 94–101. DOI: [10.1117/12.611645](https://doi.org/10.1117/12.611645).
- [112] C.-m. Wu. “Periodic nonlinearity resulting from ghost reflections in heterodyne interferometry”. In: *Optics Communications* 215 (Jan. 2003), pp. 17–23. DOI: [10.1016/S0030-4018\(02\)02203-4](https://doi.org/10.1016/S0030-4018(02)02203-4).
- [113] Giovanni Cavagnero, Giovanni Mana, and Enrico Massa. “Effect of recycled light in two-beam interferometry”. In: *Review of scientific instruments* 76.5 (2005), p. 053106.
- [114] Gerhard Heinzl et al. “Interferometry for the LISA technology package LTP: an update”. In: *Journal of Physics: Conference Series*. Vol. 32. 1. IOP Publishing. 2006, p. 132.
- [115] Peter G. Halverson and Robert E. Spero. “Signal processing and testing of displacement metrology gauges with picometre-scale cyclic nonlinearity”. In: *Journal of Optics A: Pure and Applied Optics* 4.6 (2002), S304.
- [116] Shahram Mohammad Nejad and Saeed Olyaei. “Accuracy improvement by nonlinearity reduction in two-frequency laser heterodyne interferometer”. In: *Electronics, Circuits and Systems, 2006. ICECS'06. 13th IEEE International Conference on*. IEEE. 2006, pp. 914–917.
- [117] Nile M. Oldham et al. “Electronic limitations in phase meters for heterodyne interferometry”. In: *Precision engineering* 15.3 (1993), pp. 173–179.
- [118] K. Oka, M. Tsukada, and Y. Ohtsuka. “Real-time phase demodulator for optical heterodyne detection processes”. In: *Measurement Science and Technology* 2.2 (1991), p. 106.
- [119] David B. Schaechter et al. “Diffraction hardware testbed and model validation”. In: *Proceedings of SPIE*. Vol. 4852. 2003, pp. 302–313.
- [120] René Schödel. “Limiting aspects in length measurements by interferometry”. In: *Fringe 2009*. Springer, 2009, pp. 1–7.
- [121] A. Hirai, M. Kajima, and S. Telada. “Displacement”. In: *Handbook of Optical Metrology*. Ed. by Toru Yoshizawa. CRC Press, 2008. DOI: [10.1201/9781420019513.pt3](https://doi.org/10.1201/9781420019513.pt3).
- [122] Feng Zhao et al. “Common-path multichannel heterodyne laser interferometer for subnanometer surface metrology”. In: vol. 3740. 1999, pp. 642–645. DOI: [10.1117/12.347766](https://doi.org/10.1117/12.347766).
- [123] Philip E. Ciddor. “Refractive index of air: new equations for the visible and near infrared”. In: *Appl. Opt.* 35.9 (Mar. 1996), pp. 1566–1573. DOI: [10.1364/AO.35.001566](https://doi.org/10.1364/AO.35.001566).
- [124] B. Edlén. “The Refractive Index of Air”. In: *Metrologia* 2 (Apr. 1966), pp. 71–80. DOI: [10.1088/0026-1394/2/2/002](https://doi.org/10.1088/0026-1394/2/2/002).
- [125] Edson R. Peck and Kaye Reeder. “Dispersion of Air*”. In: *J. Opt. Soc. Am.* 62.8 (Aug. 1972), pp. 958–962. DOI: [10.1364/JOSA.62.000958](https://doi.org/10.1364/JOSA.62.000958).

- [126] G. Bönsch and E. Potulski. “Measurement of the refractive index of air and comparison with modified Edlén’s formulae”. In: *Metrologia* 35.2 (1998), p. 133.
- [127] W. Wagner and A. Pruß. “The IAPWS Formulation 1995 for the Thermodynamic Properties of Ordinary Water Substance for General and Scientific Use”. In: *Journal of Physical and Chemical Reference Data* 31.2 (2002), pp. 387–535. DOI: [10.1063/1.1461829](https://doi.org/10.1063/1.1461829).
- [128] N. Bobroff. “Residual errors in laser interferometry from air turbulence and nonlinearity”. In: *Applied Optics* 26.13 (July 1987), pp. 2676–2682. DOI: [10.1364/AO.26.002676](https://doi.org/10.1364/AO.26.002676).
- [129] O. Svelto. *Principles of Lasers*. 5th ed. Springer US, 2010. DOI: [10.1007/978-1-4419-1302-9](https://doi.org/10.1007/978-1-4419-1302-9).
- [130] Gianni Di Domenico, Stéphane Schilt, and Pierre Thomann. “Simple approach to the relation between laser frequency noise and laser line shape”. In: *Appl. Opt.* 49.25 (Sept. 2010), pp. 4801–4807. DOI: [10.1364/AO.49.004801](https://doi.org/10.1364/AO.49.004801).
- [131] R. Paschotta, H. R. Telle, and U. Keller. “Noise of Solid-State Lasers”. In: *Solid-State Lasers and Applications*. Ed. by Alphan Sennaroglu. CRC Press, 2006. DOI: [10.1201/9781420005295.ch12](https://doi.org/10.1201/9781420005295.ch12).
- [132] Rüdiger Paschotta. “Field guide to optical fiber technology”. In: SPIE. 2010.
- [133] Y. Salvadé and R. Dändliker. “Limitations of interferometry due to the flicker noise of laser diodes”. In: *Journal of the Optical Society of America A* 17.5 (May 2000), pp. 927–932. DOI: [10.1364/JOSAA.17.000927](https://doi.org/10.1364/JOSAA.17.000927).
- [134] K. Petermann. *Laser Diode Modulation and Noise*. Advances in Opto-Electronics. Springer Netherlands, 1988. DOI: [10.1007/978-94-009-2907-4](https://doi.org/10.1007/978-94-009-2907-4).
- [135] S. R. Bowman. “High-power diode-pumped solid-state lasers”. In: *Optical Engineering* 52.2 (2012), p. 021012.
- [136] ZEMAX Development Corporation. *ZEMAX Optical Design Program User’s Guide*. June 2009.
- [137] John W. Gordon and Julius O. Smith. “A Sine Generation Algorithm for VLSI Applications”. In: *Proc. 1985 Int. Computer Music Conf., Vancouver*. Computer Music Association. Computer Music Association, 1985.

